

8-2003

Synthesis of Porous Monoclinic Tungsten Oxides and Their Application in Sensors

Anil Bhalchandra Waghe

Follow this and additional works at: <http://digitalcommons.library.umaine.edu/etd>

 Part of the [Chemistry Commons](#)

Recommended Citation

Waghe, Anil Bhalchandra, "Synthesis of Porous Monoclinic Tungsten Oxides and Their Application in Sensors" (2003). *Electronic Theses and Dissertations*. 203.

<http://digitalcommons.library.umaine.edu/etd/203>

This Open-Access Thesis is brought to you for free and open access by DigitalCommons@UMaine. It has been accepted for inclusion in Electronic Theses and Dissertations by an authorized administrator of DigitalCommons@UMaine.

**SYNTHESIS OF POROUS MONOCLINIC TUNGSTEN OXIDES AND THEIR
APPLICATION IN SENSORS**

By

Anil Bhalchandra Waghe

B.Sc. University of Bombay, 1986

M.Sc. Indian Institute of Technology, 1988

A THESIS

Submitted in Partial Fulfillment of the

Requirements for the Degree of

Doctor of Philosophy

(in Chemistry)

The Graduate School

The University of Maine

August, 2003

Advisory Committee:

Carl P. Tripp, Professor of Chemistry, Co-Advisor

Bruce L. Jensen, Associate Professor of Chemistry, Co-Advisor

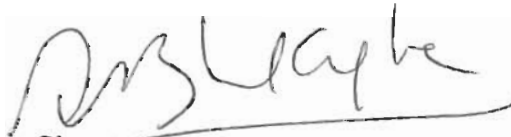
Raymond Fort, Professor of Chemistry

Alla Gamarnik, Assistant Professor of Chemistry

Brian Frederick, Associate Professor of Chemistry

LIBRARY RIGHTS STATEMENT

In presenting this thesis in partial fulfillment of the requirements for an advanced degree at The University of Maine, I agree that the Library shall make it freely available for inspection. I further agree that permission for "fair use" copying of this thesis for scholarly purposes may be granted by the Librarian. It is understood that any copying or publication of this thesis for financial gain shall not be allowed without my written permission.


Signature:

Date: 6-26, 2003

SYNTHESIS OF POROUS MONOCLINIC TUNGSTEN OXIDES AND THEIR APPLICATION IN SENSORS

By Anil Bhalchandra Waghe

Thesis Co-Advisors: Dr. Carl P. Tripp and Dr. Bruce L. Jensen

An Abstract of the Thesis Presented
in Partial Fulfillment of the Requirements for the
Degree of Doctor of Philosophy
(in Chemistry)
August, 2003

Semiconducting metal oxide sensors are limited in their usage because of their poor detection selectivity. The current approach to achieve better selectivity in SMO detection uses prefiltering/ preconcentration schemes to reduce the number of gases in contact with the sensor in combination with array-based detection. In this thesis we have investigated different materials and approaches for use as elements in an array based detection system.

One approach we have investigated involves the use of porous monoclinic WO_3 to obtain size selectivity in detection within the sensing element itself. In chapter 3 we describe the synthetic protocol used to generate high surface area porous monoclinic tungsten oxide. Mesoporous oxides are produced by a sol-gel polymerization in the presence of a self-assembled surfactant structure. This approach has not been applied to the synthesis of WO_3 based oxides because the presence of salts leads to mixtures of

WO₃ and tungstates. By minimizing the presence of Na⁺ ions, it is shown that ordered porous monoclinic WO₃ can be prepared. The sodium tungstate is first passed through an ion exchange resin to remove the sodium and tungstic acid thus formed is then added to solution containing a cationic surfactant, n-cetyltrimethylammonium bromide (CTAB) to template the structure. While a salt is formed with the CTAB cation, it does not lead to stable tungstates because these salts are easily decomposed during the calcination step. It is also shown that the need for ion-exchange can be avoided by using ammonium tungstate as a precursor in place of sodium tungstate. As with CTAB cations, the NH₄⁺ ions are easily decomposed during the calcination step. While the surfactant template collapses during the calcination step, the morphology and properties of the product is controlled by the initial template structure. Using these cationic surfactant based recipes unique high surface area and porous monoclinic WO₃ powders are prepared.

In Chapter 4, we examine the sensor properties of the various porous WO₃ powders. The sensors were tested to a series of alcohols of various size as well as dimethyl methyl phosphonate (DMMP, a nerve agent stimulant) and it was found that there was a size dependent response signal on the porous WO₃ relative to sensors fabricated with nonporous WO₃ powders. IR spectroscopic measurements shows that the difference in sensor responses on porous material was due to a size dependent control over the amount of alcohol absorbed on the surface. A key aspect of this approach is to operate the sensors in a difference mode in which a gas pulse is simultaneously exposed to several sensors composed of both porous and nonporous powders. By comparing the response on a porous sensor to that of a nonporous sensor it is possible to separately distinguish the signal of DMMP from methanol. The ability to distinguish the response of

DMMP from methanol has been a longstanding goal to demonstrate selectivity in nerve agent detection.

In chapter 5 we examined a different approach to achieve selectivity in an array based SMO sensor. Specifically, the approach involves the use of UV illumination to selectively decompose adsorbed molecules from the surface of WO_3 . In infrared studies, it is found that adsorbed DMMP decomposes under UV illumination at room temperature to form a stable methyl phosphate species on the surface. However, the decomposition under UV does not occur with the lattice oxygen but rather with the ozone or surface O^- sites oxygen radicals produced in the gas phase and this is and this is unlikely to lead to a change in sensor response. In addition, it is found that the sensor base conductivity is also very sensitive to UV illumination at room temperature. The UV generates electron-hole pairs that decompose surface water and these results in the intercalation of H^+ into the material to produce tungsten bronzes and a resulting change in base conductivity.

ACKNOWLEDGMENTS

I wish to express my appreciation to all the people who made my studying in the University of Maine pleasurable. First of all, I thank my advisors Dr. Carl Tripp and Dr. Bruce L. Jensen. I also want to thank It was a great pleasure working with both of my advisors. The access to the wider spectrum of knowledge which I gained by having joint advisors was unique.

Dr. Carl Tripp, my joint research advisor. I gained deeper knowledge of Sensor, FTIR, Raman spectroscopy and more. His wisdom, enthusiasm, encouragement and his deep concern for quality of work was exemplary. Without his constant support and follow up on this work, it would not have been a reality. I also want to thank his family for being very nice to me and for serving extremely delicious food during various get together at their home.

Dr. Bruce Jensen, my joint research advisor and lab coordinator, for his help and guidance. I am very thankful to him for the knowledge I gained after taking his classes and teaching Organic labs and lecture. I especially treasure the wonderful chat we had together about teaching, research and black bear games. I sincerely believe that he is well organized best teacher and researcher. I learnt excellent teaching skills and various research techniques from him.

I express my gratitude to Dr. Ray Fort who has been a member of my advisory committee for giving me helpful advice for my research and teaching. I benefited a lot from taking his classes.

I thank another member of my advisory committee, Dr. Alla Gamarnik. I am glad that I had opportunity to learn from her. She was always helpful and supportive. Her interest and participation in my committee's work is greatly appreciated.

I am also grateful to have Dr. Brian Federick for his various suggestions for this thesis and for serving as a committee member. The reference material he provided for this thesis was very useful.

My sincere gratitude goes to late Dr. Brian Green. I admire him as a brilliant Professor and wonderful person. His untimely death was a huge loss to the Department of Chemistry and the University. I also thank him for guiding me in my early stage of research.

I want to express my appreciation to the department of chemistry chair, Dr. Barbara Cole and laboratory of surface science chair Dr. Robert Lab for giving me an opportunity to work with two great departments, and also being kind and helpful in every way.

I would also thank to Prof. Jay Rasaiah for his support and advise to me and my wife.

I would also like to acknowledge George Bernhardt, David LaBrecque and David Frankel for taking good care of the instrumentation and teaching me various instrumentation techniques. I couldn't have conducted any experiment without the instruments working properly. I will take opportunity to thank Prof. Martin Yeats from Geology department for allowing me to use the XRD instrument. I also want to thank

Kelly Edwards from the Electron Microscopy Laboratory, Department of Biological Sciences for running TEM and SEM samples with short notice.

My sincere gratitude goes to Cynthia Comeau, Margi Forbes, Sue Ashley, Patty Paul for their efficient paper work.

Some of the greatest help came from my former group members Sergei Slobodzian, Ahmed Malkawi, Sofian Kanan, Devnesan Loganathan, Zhixiang Lu, Shivshankar Bitla, Chung Kim, and current members Haiyan Li, Cuihong, Wei Gu, Laura Swartz and William Tze.

I will also thank Meg Hausman, Ahmed AlOmary, Jinasena & Ruwini and all current and former undergraduate and graduate students for their help and support.

I also wants thank my parents Mr. Bhalchandra Waghe and Mrs. Ashalata Waghe and my brothers Ashok and Ajit and all my family members for their encouragement support, understanding and love.

Finally, I want thank my son Omkar and my wife Aparna who helped my acclimatization to the life and making.

The list of people who helped me during my work is long and due to space I can not include name of everyone but I will always remember and appreciate their help.

TABLE OF CONTENTS

ACKNOWLEDGMENTS.....	ii
LIST OF TABLES.....	viii
LIST OF FIGURES.....	ix
CHAPTER	
I. INTRODUCTION.....	I
1.1. Background.....	1
1.2. Chemistry of Sensor Response.....	3
1.3. Selectivity.....	4
1.4. FTIR Studies on WO ₃	7
1.5. Sol-Gel Synthesis of nano-Sized WO ₃ particles.....	9
1.5.1. Chelating Agents Approach.....	12
1.5.2. Emulsion Based Synthesis.....	13
1.6. Porous Materials.....	18
1.6.1. General Synthesis of Mesoporous Oxides.....	18
1.6.2. Mechanism of Pore Formation.....	19
1.6.3. Pore Size Control Parameters for Mesoporous Oxides.....	21
1.7. Summary.....	24
2. EXPERIMENTAL.....	25
2.1. Materials.....	25
2.2. Synthesis of Tungsten Trioxide.....	27

2.2.1. Preparation of Tungstic Acid Solution	27
2.2.2. Calcination	28
2.3. Characterization of Tungsten Oxide Powders	29
2.3.1. Raman Spectroscopy	29
2.3.2. Infrared Spectroscopy	31
2.3.3. BET (Brunauer Emmett and Teller) Surface Area Measurement.....	34
2.3.4. Porosity and Pore Size Distribution.....	36
2.3.5. X-ray Diffraction (XRD)	44
2.3.6. Scanning Electron Microscopy (SEM).....	44
2.3.7. Transmission Electron Microscopes (TEM).....	45
3. SYNTHESIS OF POROUS MONOCLINIC WO ₃ USING CATIONIC SURFACTANT TEMPLATING METHODS	46
3.1. Introduction	46
3.2. Experimental.....	49
3.2.1 Synthesis of Porous WO ₃ using MCM-41 type Templating Architecture.....	49
3.2.2. Synthesis of Porous WO ₃ using MCM-48 Templating Architectures	50
3.2.3 Synthesis of Porous WO ₃ using (NH ₄) ₂ WO ₄ ·2H ₂ O	50
3.3. Results and Discussion	51
3.3.1. Raman Spectroscopy	51
3.3.2. X-ray Diffraction (XRD)	53

3.3.3. TEM Micrographs	64
3.3.4. SEM Micrographs.....	68
3.3.5. N ₂ Adsorption Isotherms	68
3.3.6. Porous WO ₃ Generated using (NH ₄) ₂ WO ₄ as the Precursor.....	74
3.4. Summary.....	76
4. SIZE SELECTIVE DETECTION IN POROUS WO ₃ BASED SENSORS	77
4.1. Introduction	77
4.2. Experimental.....	80
4.3. Results and Discussions.....	84
4.3.1. Adsorption of Methanol and DMMP.....	85
4.3.2. Adsorption of Series of Alcohols	91
4.4. Summary.....	95
5. UV ILLUMINATION OF WO ₃ POWDER SENSORS.....	97
5.1. Background.....	97
5.2. Experimental.....	99
5.3. Results and Discussion	99
5.3.1. IR Studies.	99
5.3.2. Sensor Testing Under UV Illumination.....	104
5.4. Summary.....	114
6. FUTURE WORK	115
REFERENCES	116
BIOGRAPHY OF THE AUTHOR	125

LIST OF TABLES

Table 3.1	Molar Ratios of Reagents	52
Table 3.2	XRD Low Angles Peaks.....	56
Table 3.3	d-spacing and Surface Areas of Samples.....	70
Table 5.1	A Summary of Band Assignments for DMMP Adsorbed on TiO ₂ and WO ₃ surface at 27 °C	102

LIST OF FIGURES

Figure 1.1.	Chemiresistive semiconducting metal oxide Gas sensor platform	2
Figure 1.2.	Sensor response to a methanol gas pulse	5
Figure 1.3.	Schematic of prototype hybrid chemical sensor suite	6
Figure 1.4.	IR studies on thin film sensor element	8
Figure 1.5.	Transmission infrared spectra of adsorbed DMMP on commercial powder (top) and nano-sized powder (bottom)	15
Figure 1.6.	Inverse micelles and droplets in the emulsion showing tungstic acid and water trapped inside droplets.....	17
Figure 1.7.	Templated Fabrication of Porous Adsorbents.....	20
Figure 1.8.	Steps in synthesis of mesoporous materials.....	21
Figure 1.9.	Spherical micelle showing surfactant tail influence on the size of pores.	22
Figure 2.1.	Experimental setup for preparation of sol (H_2WO_4 solution) using ion exchange resin.....	26
Figure 2.2.	Raman Spectra of (a) porous WO_3 sample A1 (b) nonporous WO_3 sample C (c) hydrated WO_3 and (d) WO_3 produced using Na_2WO_4 without ion exchange.....	30
Figure 2.3.	Transmission cell used for IR experiments.....	32
Figure 2.4.	DRIFT apparatus for IR measurements	33

Figure 2.5.	Desorption (top part of hysteresis loop) and Adsorption (bottom part of hysteresis loop) curves Plot A starts with filled pores and Plot B starts with empty pores showing hysteresis in type IV isotherm.	37
Figure 2.6.	Adsorption isotherms shown as coverage θ or volume versus partial pressure of the gas.	39
Figure 2.7.	Different stages in adsorption of gas molecules on a surface	40
Figure 2.8.	Cylindrical geometry where r_p : radius of pore, d_o : mean diameter, d_A : adsorbate diameter, d_E : adsorbent diameter $(d_o = 0.5 (d_A + d_E))$	42
Figure 3.1.	Raman Spectra of (a) sample A1, (b) nonporous WO_3 sample C, (c) hydrated WO_3 and (d) WO_3 produced using Na_2WO_4 without ion exchange (sample A4).	54
Figure 3.2.	XRD Spectra of uncalcinated and calcinated WO_3 (a) uncalcinated A1 sample, (b) A1 sample after calcination at 500 °C, (c) non-porous C sample before calcination and (d) non-porous sample after calcination at 500 °C.	55
Figure 3.3.	XRD spectra of WO_3 samples A1, A2 and A3 before calcination and Na_2WO_4	57
Figure 3.4.	XRD patterns of various porous WO_3 samples after calcination at 500 °C. The XRD pattern for non-porous WO_3 sample C is provided for comparison.....	58

Figure 3.5.	Raman Spectra of sample A2, (a) before calcination and after calcination step (c) is the Raman spectra of solid CTAB.	60
Figure 3.6.	Raman spectra of uncalcinated WO_3 and Na_2WO_4	62
Figure 3.7.	XRD spectra of WO_3 top curve showing B1 sample before calcination and bottom curve showing B1 sample after calcination at $500^\circ C$	63
Figure 3.8.	TEM micrograph of sample A1. Small part in circle in a is magnified in picture b. (a) A1 ,(b) A1 sample magnified, (c) A2 sample, (d) A3 sample	65
Figure 3.9.	TEM micrographs of porous WO_3 samples (a) B1 sample, (b) picture shows B1 under magnification, (c) B2 sample	66
Figure 3.10.	TEM micrograph of non-porous WO_3 sample	67
Figure 3.11.	SEM picture of sample porous WO_3 (a and b) sample B1 (c) B2, (d) A1, (e) A2 and (f) A3.....	69
Figure 3.12.	N_2 Adsorption Isotherms for porous samples B1, B2, A1 and a nonporous C, sample C is shown as curve d for comparison.	73
Figure 3.13	XRD of MCM-48 samples B1 and B2.	75
Figure 4.1.	The Structures of Nerve Agents, Tabun, Sarin and Simulant DMMP showing their relative size and shapes	78
Figure 4.2.	Reaction equations of DMMP at elevated temperature on various metal oxides.	79
Figure 4.3.	Sensor testing device.	82
Figure 4.4.	Methanol and DMMP space filling models and their sizes	84

Figure 4.5.	Space filling models of various alcohols showing relative size and shapes.....	87
Figure 4.6.	Typical 3 pulse sequence of methanol, t-butanol and DMMP	88
Figure 4.7.	$\Delta C_{\text{porous}} / \Delta C_{\text{nonporous}}$ value as a function of size of the molecule	90
Figure 4.8.	FTIR of Methanol on porous and nonporous tungsten oxide	91
Figure 4.9.	Typical FTIR spectrum of various alcohols adsorbed on WO_3	92
Figure 4.10.	Relative adsorbed amount of various alcohols on WO_3 Samples A2 and A3 as determined by IR spectroscopy.	93
Figure 4.11.	Ratio of response of A2 sensor to A3 sensor for each alcohol.	95
Figure 5.1.	IR spectra of DMMP adsorbed on nonporous WO_3 at a) 27 °C and then evacuated at the specified temperature for 30 minutes. All spectra were recorded at room temperature.	101
Figure 5.2.	IR spectra of a) DMMP adsorbed on WO_3 at room temperature followed by UV illumination in air for the indicated time.....	103
Figure 5.3.	Sensor response curve to methanol pulses at 400 °C using nonporous WO_3 powder sensor.	105

Figure 5.4.	Resistance change to UV illumination in a nonporous WO ₃ powder sensor at room temperature.....	108
Figure 5.5.	Resistance change under continuous UV illumination at room temperature.	109
Figure 5.6.	Characteristic plot of base resistance vs temperature for a WO ₃ sensors.....	111
Figure 5.7	Water Desorption curve on WO ₃ powder.....	113

Chapter 1

INTRODUCTION

1.1. Background

Developing semiconducting metal oxide (SMO) based sensors has been a cornerstone of research activity at the Laboratory for Surface Science and Technology (LASST) at the University of Maine for the last 20 years. While films such as SnO_2 ^{1,2}, ZnO ^{3,4} and WO_3 ⁵ have been used as the sensing element in gas detectors, the work at LASST has focused on WO_3 based materials. The advantage of SMO based detection is that it provides an inexpensive, compact, and rapid method for the detection of low concentrations (ppb) of gases. However, the SMO detectors are plagued by poor detection selectivity and it is this aspect that provided the impetus for the research described in this thesis.

Figure 1.1 shows a typical sensor platform used for the SMO gas sensor fabricated at LASST⁶. A sapphire substrate is prepared with interdigitated platinum electrodes on the top and a serpentine heater and resistance temperature device (RTD) at the bottom. SMO based sensors are typically fabricated by depositing an oxide layer, either as a thin film oxide layer or a powder dispersed in with a suitable binder on the top of underlying platform containing the electrical contacts.⁷⁻⁹ The work at LASST has focused on thin film based technologies in which WO_3 films of about 500 Å thickness are deposited by reactive Rf magnetron sputtering. The RTD is needed because the sensors are typically operated at temperatures of 250 °C to 400 °C in order to increasing detection sensitivity by increase the rate of reaction.

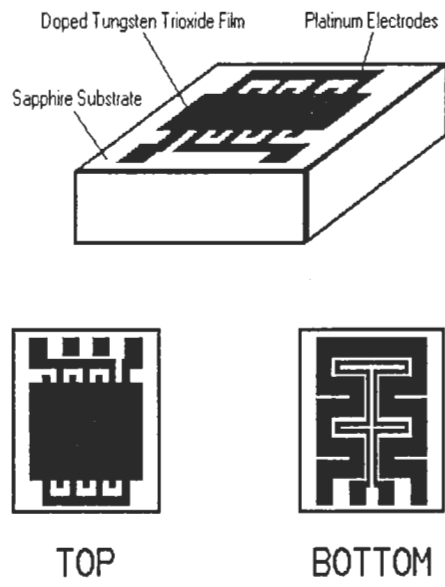
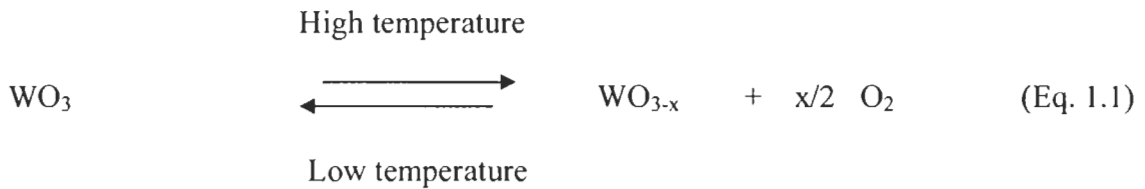


Figure 1.1. Chemiresistive Semiconducting metal oxide Gas sensor platform.

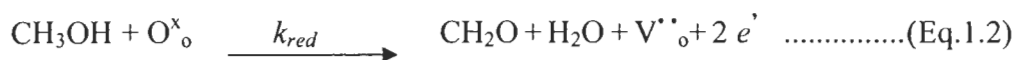
Another reason for operating at high temperature is at room temperature the WO₃ film is an insulator. At elevated temperatures, the WO₃ becomes sub-stoichiometric in composition due to loss of lattice oxygen and semiconducting in nature.



The conductivity increases because the carrier concentration increases as “x” increases in WO_{3-x} and because of thermal excitation of electrons in to the conduction bands. The lattice oxygen concentration also occurs when an oxidizing or reducing gas comes in contact with the WO₃ surface, which leads to a change in carrier concentration and signal detection in the sensor.

1.2. Chemistry of Sensor Response

The reaction sequence leading to a change in conductivity is illustrated using methanol as the target gas as described in the work of Dr. Frederick’s group at LASST^{8,9,10} In Figure 1.2, the upper curve shows the time interval of the methanol gas pulse. The lower curve in Figure 1.2 shows that a decrease in resistance occurs with the initial introduction of the methanol. The methanol in contact with the WO₃ surface is oxidized to CH₂O by reacting with the lattice oxygen according to:¹¹



where O_o^x is lattice oxygen and V_o^{**} is positively charged vacancies generated in WO_3 at elevated temperature.

This process occurs rapidly owing to the high mobility of the lattice oxygen leading to a fast initial decrease in resistance which plateaus when the lattice oxygen attains a new equilibrium concentration level. The removal of the lattice oxygen leads to vacancies and generation of a pair of electrons, leading to a decrease in the resistance of the oxide film. When the methanol gas pulse is turned off, the equilibrium concentration of lattice oxygen is reestablished to the original level (and hence the resistance of the film) through oxidation with the oxygen gas in the air.



1.3. Selectivity

The above reaction mechanism with methanol also illustrates the problem in detection selectivity. There is very little information content in the sensor response other than an increase in conductivity occurs when a reducing gas molecule is oxidized and a decrease occurs when a gas molecule is reduced. Given that any organic molecule will undergo an oxidation reaction with the lattice oxygen, a problem clearly exists in distinguishing the response from a target gas amongst the myriad of other compounds that could be present in a gas stream. This leads to false alarms and is the biggest technical hurdle preventing the widespread use of this technology.

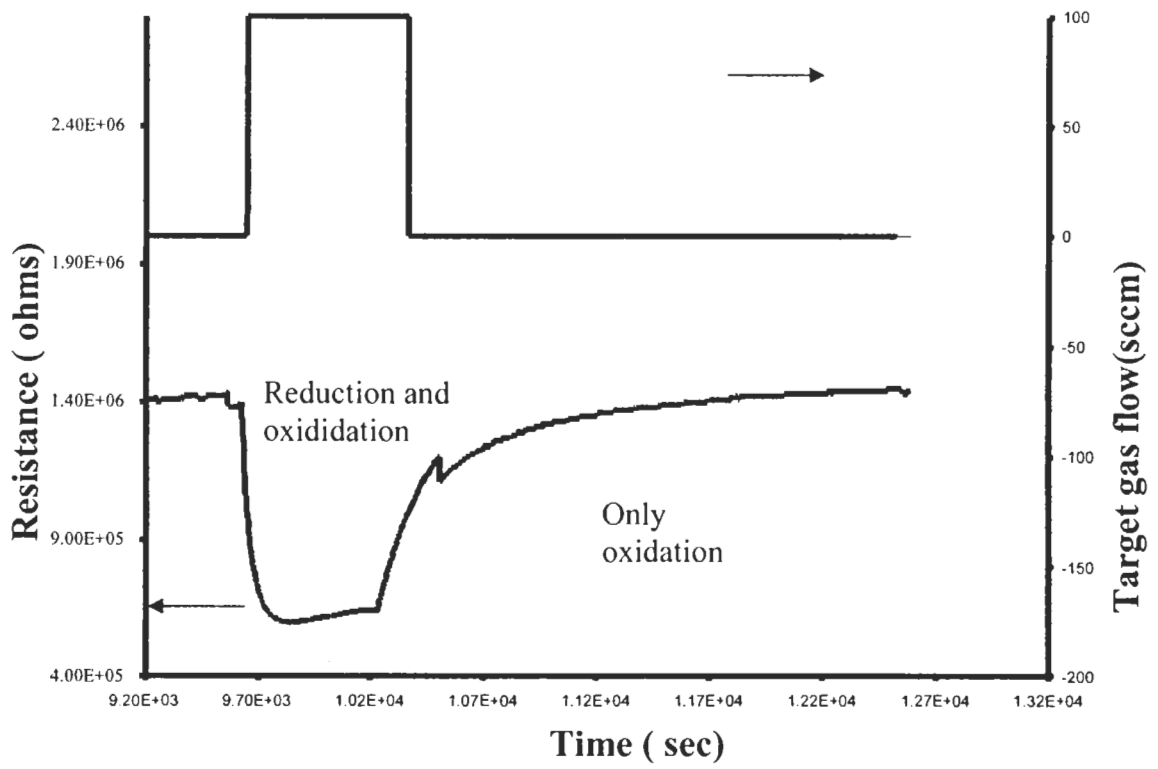


Figure 1.2. Sensor response to a methanol gas pulse

The current approaches to improve selectivity in SMO sensing involve a combination of filtration¹² / concentration¹³ and array based detection.^{14, 15} This approach is actively pursued by researchers at LASST and a schematic of this approach is shown in Figure 1.3

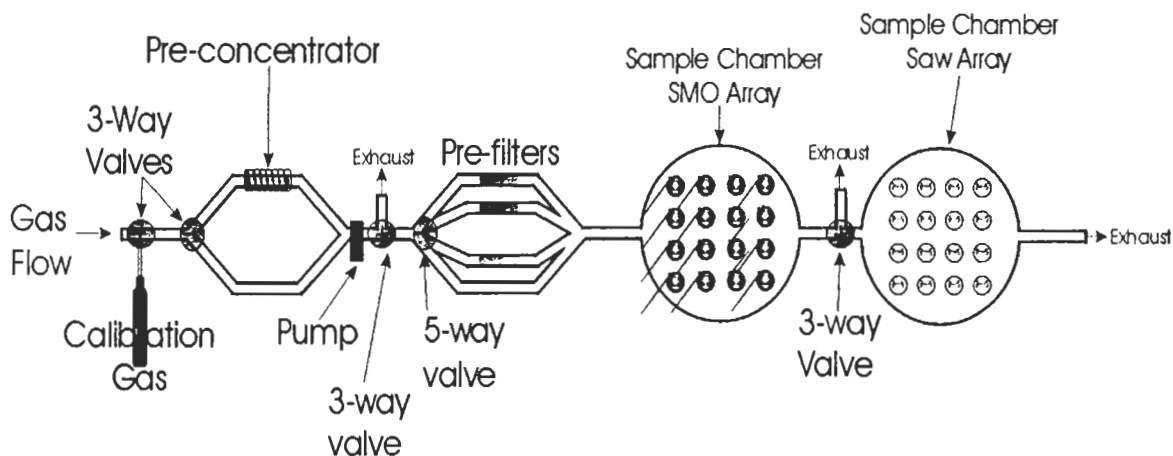


Figure 1.3. Schematic of Prototype Hybrid Chemical Sensor Suite

Use of prefilters/concentrators tackles the problem by reducing the number of components in the gas stream impinging on the SMO detector element. Materials such as inorganic membranes, zeolites, and other adsorbents are used to selectively preconcentrate and prefilter interferent molecules from the gas stream. For example, work in our group has recently shown that silica based material can be used to selectively adsorb organophosphonates from a gas stream^{16, 17} and other work by colleagues at LASST¹⁸ has shown that silicalite (a zeolite) can be used for size and polarity based separation of isoprene and NO₂ from NO.

An array-based approach tackles the problem of minimal information content of the response signal in that each element of the array produces different response characteristics to the gas matrix. In this case, a bank of sensors is used in which each sensor element produces a different response to the various components of the gas stream. Variables such as metal oxide composition and morphology, impregnation with metal catalysts and operational temperature are a few approaches that are under investigation to achieve distinguishable sensor array elements.¹⁹⁻²⁴ Neural network methodologies are then used to process the complex response signal.

The role of our research effort in the array based approach was to use infrared spectroscopy to provide a molecular understanding of the chemical reactions of various gaseous molecules on the different sensor materials. The aim was to use the molecular information derived from the spectroscopic studies to provide insight into the selection of material and operational conditions for the sensor elements used in an array-based detection system. Ideally, the infrared studies would be conducted *in situ* directly on the sensor devices themselves as this would lead to a direct correlation between surface reactions and sensor response. In practice, this proved to be very difficult to perform and the reason for this can be traced to two fundamental aspects of infrared spectroscopy.

1.4. FTIR Studies of WO₃

The first limitation arises from the fact that infrared spectroscopy is not a surface sensitive technique. The infrared beam passes through the bulk as well as the surface of the WO₃. In the case of the WO₃ sensor platform shown in Figure 1.4, transmission studies were not possible owing to the opacity of the sapphire substrate.

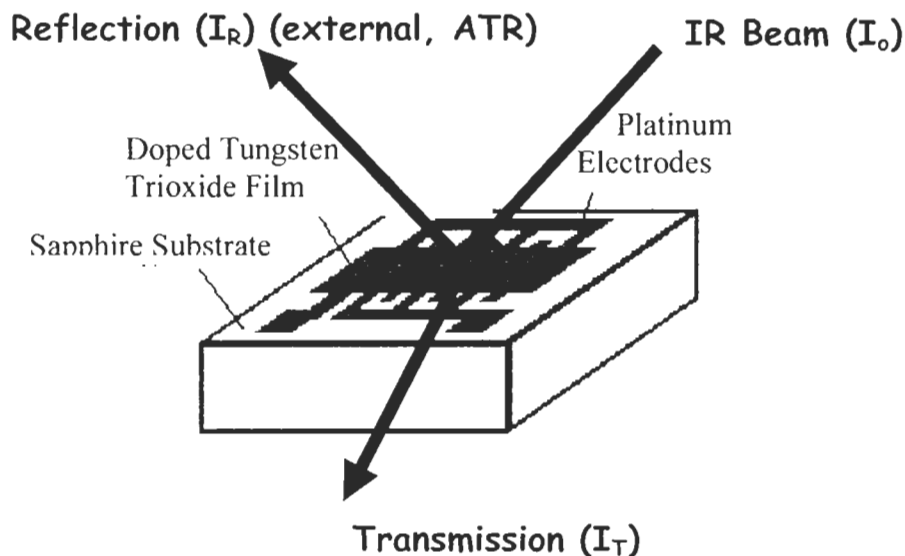


Figure 1.4. IR studies on thin film sensor element

External reflection measurements were attempted but these measurements on semiconducting material are difficult to interpret because of the complex refractive index (and hence the external reflectivity) changes that occur within an adsorption peak superimposed on a semiconducting metal oxide surface. The most promising method involved the use of Attenuated Total Reflection (ATR) in which a WO_3 film is coated on an internal reflection element.^{25, 26} While it was possible to collect spectra with this approach, our attempts to study surface reactions on WO_3 coated ATR crystals were not successful because of the difficulty in detecting the weak bands due to adsorbed species.

The second limitation arises from the fact that the light absorbed by the sample is not measured directly. In IR, a reference spectrum is first measured and then a separate spectrum is recorded with the sample in place. In recording the sample spectrum, it is the

light transmitted (I_T) or reflected (I_R) that is measured by the detector and this is then ratioed to the reference spectrum (I_o). In the case of the thin film WO_3 sample, the percent of the total light absorbed by surface species leads to a very small attenuation of the IR beam²⁷ (i.e., the difference between I_T and I_o is about 1 photon in 10^6). As a result, this places a high demand on the dynamic range (i.e., measuring a difference of 1:10⁶ between two signals) and also translates to band intensities of about 10^{-4} absorbance units which are at the edge of the practical detection limit of infrared spectrometers.

The most common method to circumvent the detection and dynamic range limitations in surface IR studies is to increase the surface area probed by the IR beam by using metal oxide powders. While the surface area probed on a thin film oxide is about 1 cm², metal oxide powders can have surface areas in excess of 500 m²/g and thus probing even milligram quantities of powder with an IR beam translate into 3-4 orders in magnitude increase in intensity of the bands due to adsorbed species. While there exists an enormous volume of literature of surface infrared studies on metal oxide powders,²⁸⁻³⁰ until our recent work^{16, 31-33} we are unaware of similar IR surface studies on WO_3 powders. The development of synthetic methods leading to the generation of high surface area WO_3 particles was the key enabler for our infrared work. Commercial particles are micron sized and were not suitable for infrared studies because they scatter the IR beam and have low surface area (< 1m²/g).

1.5. Sol-Gel Synthesis of nano-sized WO_3 particles

An exhaustive search for a commercial source of high surface area monoclinic WO_3 particles met with little success. The best commercial particles had measured

surface areas of 1.7 m²/g and it is estimated that a particle size reduction of at least a factor of 10 (i.e. about 20 m²/g) was needed for our infrared studies. A description of the synthetic methods used to produce the nano-sized particles is provided below because the recipes used in this thesis for generating mesoporous WO₃ are extensions of prior work.

Tungsten oxide powders are typically generated by the sol-gel process.³⁴ Sol-gel processing is a wet chemical route to synthesis of a colloidal suspension of solid particles or clusters in a liquid (sol), and subsequently to formation of a dual phase material of a solid skeleton filled with a solvent (gel). When the solvent is removed, the wet gel converts to a xerogel through ambient pressure drying or an aerogel through supercritical drying. In the sol preparation, the precursors (either organic or inorganic) undergo two chemical reactions: hydrolysis and condensation or polymerization, typically with acid or base as catalysts, to form small solid particles or clusters in a liquid (either organic or aqueous solvent). In this process an inorganic or organic molecular precursor M(OR)_n, is typically used as the starting material, where M is a metal and (OR) a hydrolysable alkoxy group, respectively. The reaction can be utilized to provide oxides in the form of powders or a macromolecular network for use as thin films on other substrates.

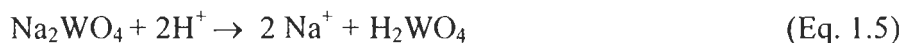
In principle the sol-gel reaction can be written as:³⁵



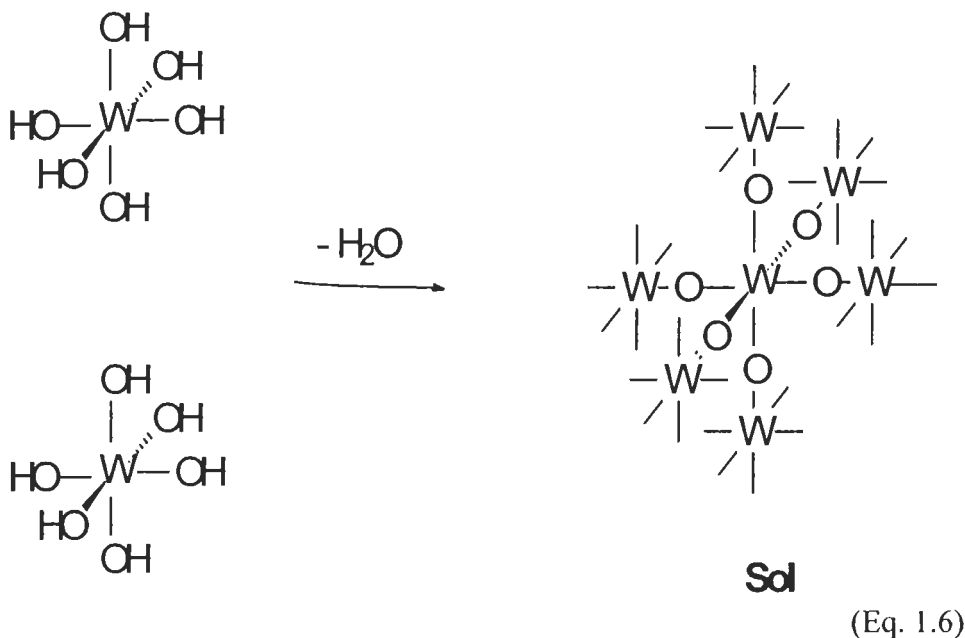
Organic additives are commonly used in sol-gel chemistry.³⁶ These additives can operate as stabilizers or reactive metal alkoxides^{37,38} towards hydrolysis or as drying

agents (such as dimethylformamide). These organic compounds and the by-products of sol-gel reactions can drastically modify the physical properties of the materials.

The literature on sol-gel tungsten oxides is almost entirely devoted to the formation of films on surfaces. The synthesis of the films can be divided into methods based on the hydrolysis of tungsten alkoxides^{39,40} and methods based on the acidification of alkali tungstates. In the latter, the most widely used sol-gel method begins with the ion exchange of sodium tungstate at ambient temperature. Chemseddine *et. al.*⁴¹ have prepared stable WO₃ films using this ion-exchange resin process. A solution of Na₂WO₄·2H₂O in water was passed through a protonated ion exchange resin, leading to a colloid solution of sodium and chloride free tungstic acid.⁴²



The sodium cation is removed and trapped by the resin. In the next step, the condensation (polymerization) of the H₂WO₄ results in a network of tungsten oxide.



The polymerization in acidic conditions involves several stages⁴², starting with formation of metal hydroxy complexes, formation of hydroxy polymers (olation), formation of oxobridges (oxolation) and finally a visible yellow tungsten trioxide hydrate $(\text{WO}_3 \cdot \text{H}_2\text{O})_n$ solid product. Depending on the concentration and polymerization conditions, the sol may precipitate from the solution as individual particulates or form a stable gel.

In the formation of WO_3 particles, the growth of the hydrated tungsten oxide sol continues until the particle precipitates from solution. This occurs when the particles are approximately micron-sized. To produce particles with high surface area (i.e., smaller size) it is necessary to inhibit the growth of the sol particulates and to limit the aggregation of particles during the calcination step.

Calcination at elevated temperature is required to convert the hydrated tungsten oxide to a crystalline form. To make stable crystalline tungsten trioxide powders, calcination temperatures of at least 500 °C are required. At temperatures below 500 °C, the crystalline WO_3 slowly reverts back to its amorphous hydrated form.^{16, 33}

1.5.1 Chelating Agents Approach

Lu *et al.* showed that it was possible to obtain small WO_3 particles with high surface area by controlling the reaction conditions through the use of organic chelating agents and water and oil emulsions.³² Chelating agents such as oxalic acid^{43, 44}, acetylacetone⁴⁵ and 2,4-pentanedione⁴⁶ have been used to generate stable WO_3 sol-gel films. The rate of condensation occurring between two W-OH groups is reduced as the number of non-condensable chelating agents attached to the central W atom increases.

The slower condensation or cure produces less stress between a sol-gel film and the substrate and this minimizes the cracking that occurs when the film is annealed at elevated temperatures.

Lu *et. al.* showed that oxalate and acetate chelating agents that lead to stable sol-gel films also inhibit the condensation, growth and aggregation of individual particles.³² Furthermore, it has been shown⁴⁴ that bound oxalate remains on the hydrated tungsten oxide particle at temperatures up to 200 °C. This was also important in powder synthesis, as the presence of coordinated oxalate at these elevated temperatures also inhibits the reduction in surface area or aggregation of particles during the calcination step. By using oxalic acid or a mixture of oxalic acid and acetic acid during the sol-gel synthesis, WO₃ particles with surface area of about 20 m²/g were produced.³³

There was a dramatic improvement in our ability to perform IR surface studies with the availability of WO₃ powders with surface areas in the 20 m²/g range. An example of this improvement is demonstrated with the spectra shown in Figure 1.5.

The top curve in Figure 1.5 shows the transmission infrared spectra of adsorbed dimethyl methyl phosphonate (DMMP, a nerve agent simulant) recorded using a commercial WO₃ powder and the bottom curve is the spectrum for the same experiment on a 20 m²/g WO₃ powder. The distinction between these curves is clearly evident as the intense bands due to the adsorbed DMMP are only observed on the high surface area powders.

1.5.2. Emulsion Based Synthesis

Although the WO₃ particles fabricated using chelating agents produced material that enabled our infrared surface studies, the question remained as to whether this is the

limit or whether it is possible to prepare material with even higher surface area. Any further increase in surface area beyond the 20 m²/g range would directly translate in improved ability to detect weak features and/or increase the lower detection limit.

However, efforts by other researches in our group to increase the surface area of the particles beyond 18-22 m²/g by altering reaction conditions with chelating agents met with little success. Clearly, a completely different synthetic approach would be needed to achieve significantly higher surface area powders.

An alternative route involved the use of emulsion-based synthesis. In this case, the condensation reaction occurs in the aqueous phase inside a water-in-oil (W/O) emulsion. A W/O emulsion is composed of a continuous phase containing solvent, micro-water-droplets, inverse micelles and free surfactant. (see Figure 1.6)

In essence, the surfactant stabilized water droplet behaves as a micro-reactor in which the condensation and hence, growth in particle is limited by its size. The conditions leading to droplet-stabilized emulsions for polymerization reactions depends on parameters such as the type and concentration of surfactant, the surfactant/water/organic solvent ratio, the rate of stirring and temperature.^{47, 48} For WO₃, the system is limited to nonionic surfactant systems as traditional cationic or anionic surfactants are salts. These salts have counter ions such as Na⁺ or Cl⁻ and their presence would lead to products containing mixed tungstates.^{49, 50}

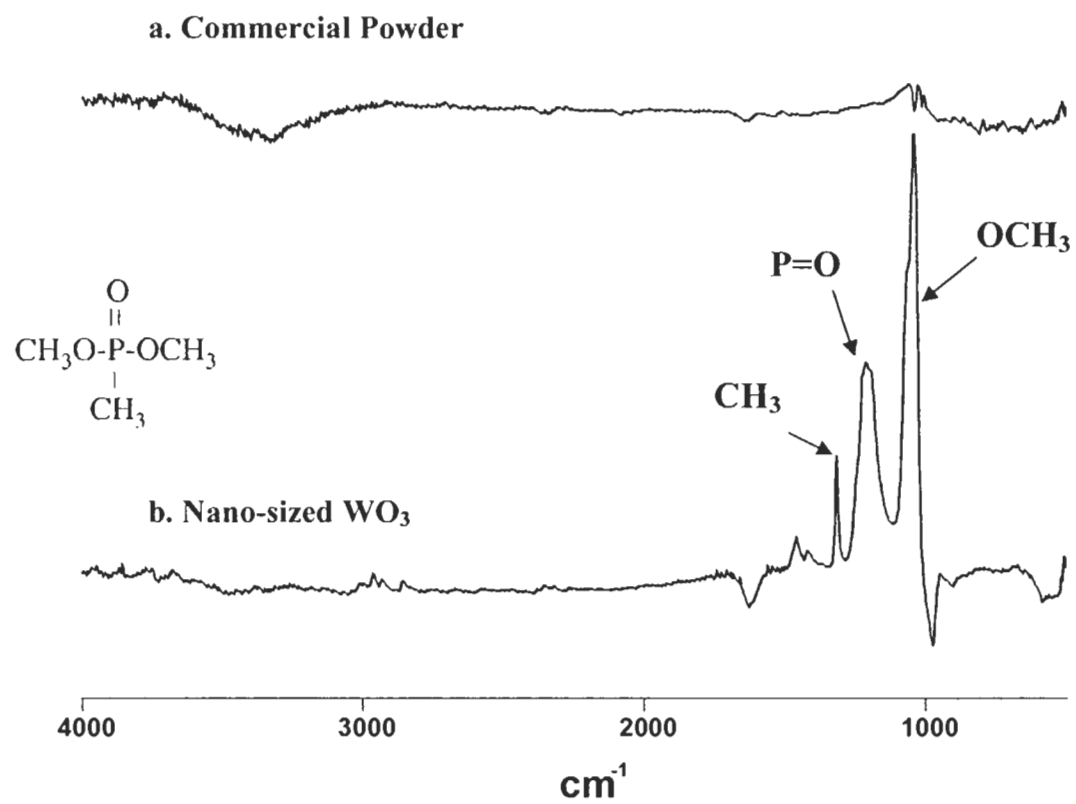


Figure 1.5. Transmission infrared spectra of adsorbed DMMP on commercial powder (top) and nano-sized powder (bottom)

In principle, the size of the droplet is in the submicron to micron range and this size provides a potential means for substantially increasing the surface area of WO_3 particles. Furthermore, the individual particles are encapsulated by surfactant and this should sterically restrict the amount of sintering occurring in the calcination step. These advantages were realized as the emulsion based powders typically had surface areas that were twice the values obtained using oxalate/acetate chelating agents. (i.e. around $40 \text{ m}^2/\text{g}$)³² This resulted in a direct improvement in sensitivity in the IR studies as the bands due to adsorbed species were also doubled in intensity on the emulsion-based powders. These powders have been the backbone of our IR studies and have been used to identify surface sites³³ as well as to elucidate the surface intermediates during decomposition of organophosphonates on WO_3 surfaces.^{13, 17, 31} Several other infrared studies on the adsorption of alcohols, sulfur based compounds (H_2S , SO_2 , CH_3SH), and nitric oxides (NO , NO_2) are in progress.

We recall that one of the aims in performing infrared measurements was to obtain a molecular insight into the behavior of the thin film sensor. This has been demonstrated on a regular basis. For example, WO_3 thin film sensors operating at $400 \text{ }^\circ\text{C}$ are poisoned by repeated doses to DMMP gas whereas no such poisoning occurs with repeated doses to methanol.³¹ IR adsorption studies have shown that adsorbed methanol is completely desorbed from WO_3 powders at $400 \text{ }^\circ\text{C}$ whereas adsorbed DMMP decomposes leaving a stable methyl phosphate species on the surface.³¹ It is the presence of the methyl phosphate that leads to poisoning of the detector.

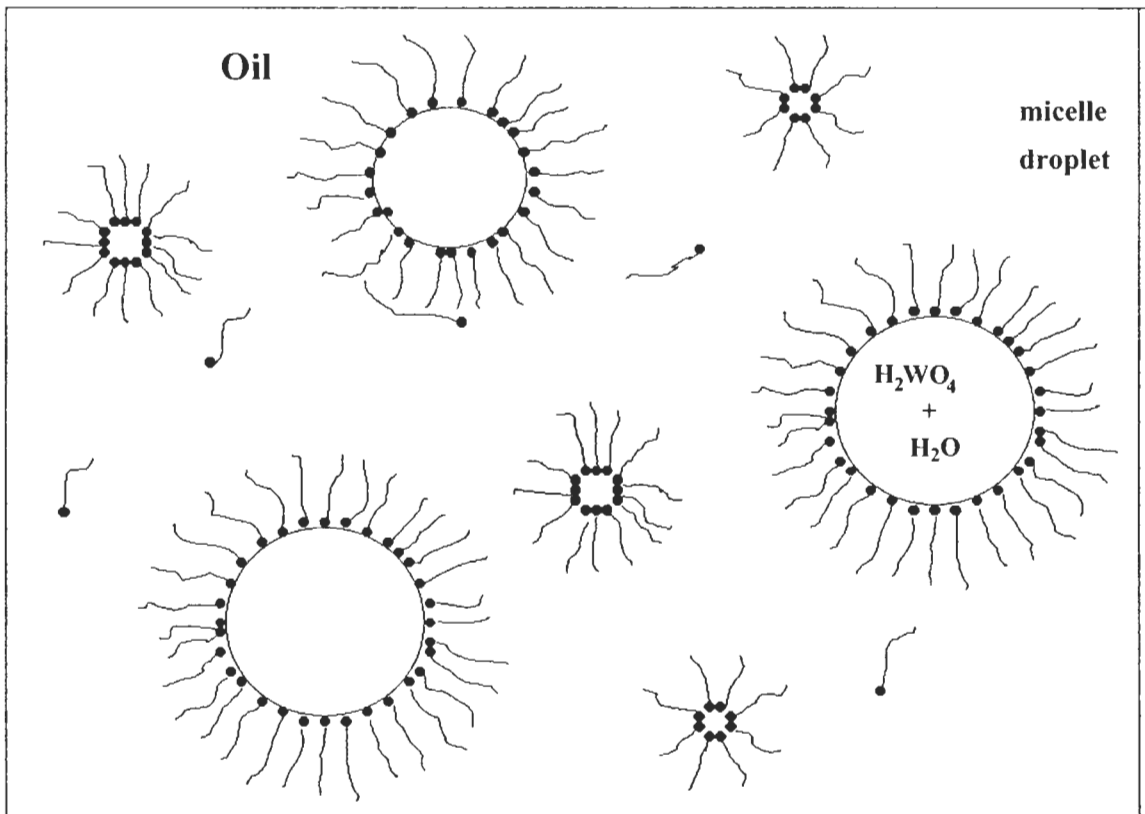


Figure 1.6. Inverse micelles and droplets in the emulsion showing tungstic acid and water trapped inside droplets

1.6. Porous Materials

While the current powders have satisfied our spectroscopic requirements, it was the use of these powders in sensing that has prompted the additional synthetic effort described in this thesis. In particular, we have found that sensors prepared using the same powders developed for the infrared studies show slightly higher sensitivity and faster response compared to their thin film counterpart. While the powder based sensors enable a direct comparison of the surface chemistry by IR and the sensor response, it was also recognized that a sol-gel preparative methodology could provide new materials for use in our array-based sensor strategy.

Specifically, it is our intent to leverage the experience gained from work with surfactant driven synthesis of nano-particles to develop “designer” nanocomposite material with structural control extending to micron dimensions.^{47,48,51-54} Known as mesoporous, materials composed of oxides, sulfides and phosphates have been made in this manner using liquid crystal surfactants and phase separated block copolymers to template the assembly of the inorganic framework.^{55,56} Mesoporous materials have significantly higher surface areas than their nonporous equivalents and thus generating porous WO₃ based on mesoporous material synthetic strategy would be attractive from this standpoint alone. However, there is an additional attraction to fabricating a sensor based on WO₃ prepared via a mesoporous synthetic route in that the periodic porous structure could provide size selectivity in detection within the sensor element itself.

1.6.1. General Synthesis of Mesoporous Oxides

The general principles leading to mesoporous oxides are illustrated in the water-oil-surfactant phase diagram shown in Figure 1.7. The emulsion polymerization

described earlier for the production of WO_3 was conducted in the lower right hand side of the phase diagram. Inverse micelles were prepared using water droplets in oil and the sol-gel polymerization occurred in the aqueous phase contained inside the micelles.

Mesoporous oxides are not formed in an oil solvent but rather, fabricated in water (*i.e.*, along the water-surfactant edge of the phase diagram) with little or no oil present. By increasing the surfactant concentration, various aggregated surfactant structures are formed in the aqueous phase. For example, the micelles convert to cylindrical micelles and at higher surfactant concentration pack into a contiguous hexagonal network. At even higher surfactant concentrations, cubic and lamellar structures are formed.

1.6.2. Mechanism of Pore Formation

Addition of the sol-gel precursor leads to polymerization in the aqueous phase surrounding the surfactant architecture and not inside the hydrophobic regions containing the surfactant tails. The procedure is shown in Figure 1.8. When operating at surfactant concentration above the second critical micellar concentration (CMC-2), rod like micelles form. The outer surfaces of these rod-like micelles are hydrophilic and the internal regions containing the surfactant tails are hydrophobic. The sol-gel polymerization occurs in the hydrophilic region around the structure and therefore, the structure of the oxide is templated by the surfactant architecture. The oxide is dried and calcined at elevated temperature to remove the surfactant leaving a highly porous and structured material with adjustable pore sizes.

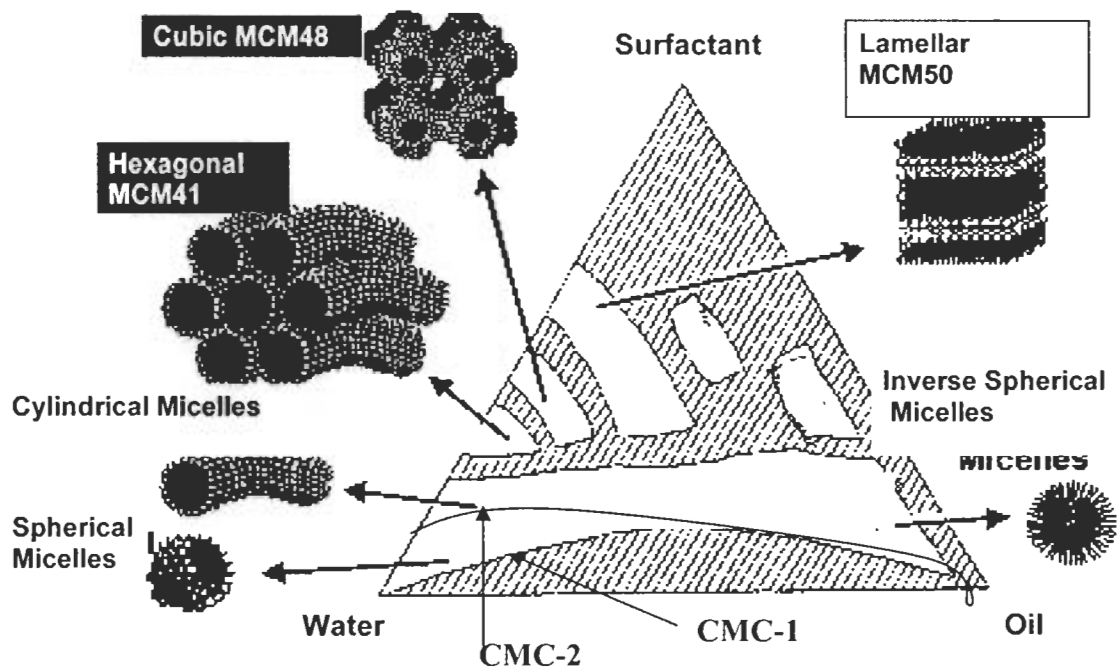


Figure 1.7. Templated Fabrication of Porous Adsorbents.⁵⁷

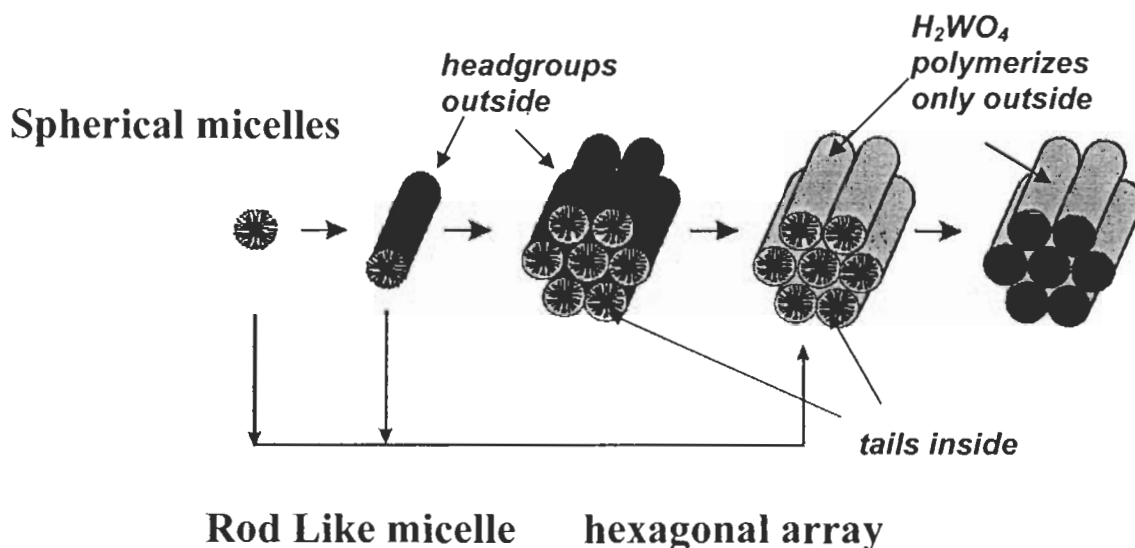


Figure 1.8. Steps in synthesis of mesoporous materials⁵⁸

1.6.3. Pore Size Control Parameters for Mesoporous Oxides

A major advantage of using mesoporous materials is that pore size can be adjusted and this may lead to a size selective approach in SMO detection. There are several experimental parameters that can be used to control the pore size and these are listed below.

Temperature: At high temperatures, surfactant molecules acquire considerable energy; self-assembly takes longer periods of time and/or forms disorganized structures. At very low temperatures, solubility problems are observed.⁴⁹ Critical micellar temperature (CMT) refers to a “pseudophase” transition from spherical to rod like micelles which

occur at low temperature or high surfactant concentrations. Regions are also observed where hydrated solid (gel or coagel) phases and liquid crystals (lamellar or hexagonal) appear (Figure 1.7).⁵⁷

Surfactant Nature: As shown in Figure 1.9, micelle size depends on the relative length of surfactant hydrophobic tail and headgroup size and charge. Longer chain lengths result in larger pore size. However, if the tail length is reduced below C-8, micelles will not self assemble. Furthermore, the surfactant length is limited to C-20 chains since natural surfactants longer than C-20 are rare and very expensive.⁵⁹⁻⁶¹

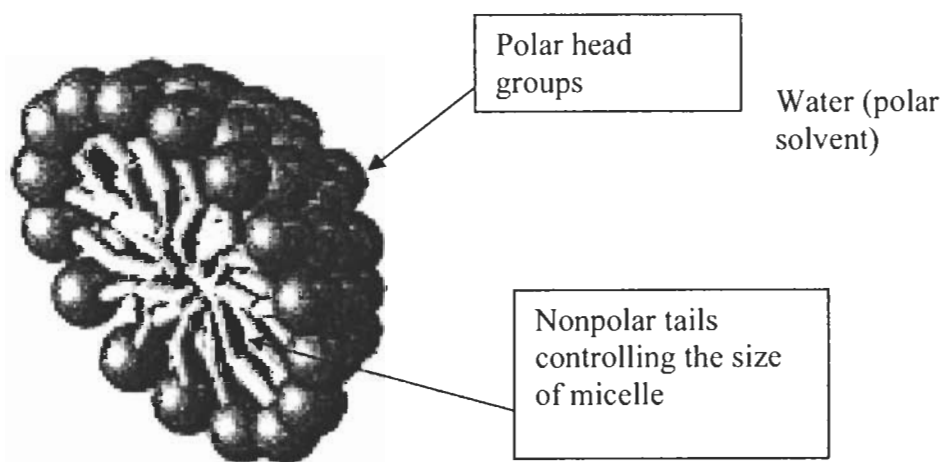


Figure 1.9. Spherical micelle showing surfactant tail influence on the size of pores⁶²

Surfactant and Water Concentration: The major factor influencing micelle size is the molar ratio of water/surfactant. At a concentration less than the first critical micellar concentration (CMC-1), micelles are not formed, whereas above the CMC-1, spherical

micelles are formed. When the concentration of surfactant is further increased, a second critical micellar concentration is reached (CMC-2). Above this concentration, rod like micelles are formed and mesoporous materials templated by these surfactant structures are known as MCM-41 (Space group: P6m name given by Mobil Catalytic Materials) type material, cubic MCM-48 (materials with space group Ia3d) and lamellar templated structures are known as MCM-50 type material respectively.^{60, 63} The topology of the mesosilicate formed is generally very similar to the known liquid crystal phases. However, sometimes unknown liquid-crystal phases, such as P6₃/mmc, are also obtained.⁶⁴

pH and Ionic Strength: Variations in pH are used to stabilize or destabilize the surfactant assembly. Addition of ionic salts reduces the micelle size by screening the electrostatic repulsion between the surfactant headgroups.

Calcination Conditions: Gel preparation is followed by calcination at 500 °C to 550 °C to remove the surfactant. Slow heating and cooling rates (1 °C/ min) are important to avoid collapse of the mesoporous structure.

Rate of stirring: It was found that high stirring rates tend to deform the structures and prevent surfactant self-assembly. Moderate stirring, on the other hand, promotes aggregation of surfactant water oil molecules and aids structure formation.

Organic Additives: Organic hydrophobic additives, such as mesitylene, acts as a “seed” for structure growth. The surfactant hydrophobic tails assemble around this “seed” resulting in larger micelles and leading to bigger pore sizes within the mesoporous

product. However, when hydrophilic additives are used, pore size does not decrease. Instead, the spherical micelles revert to cylindrical micelles.⁵⁰

Given the above synthetic latitude, a variety of mesoporous WO_3 materials should be possible. However, to the best of our knowledge, mesoporous WO_3 based materials have not been reported in the literature.

1.7. Summary

In this chapter we provided a discussion on the problem of detection selectivity in SMO based sensing. It was shown that, recent work generating WO_3 provide new opportunities in generating novel materials for SMO based sensors. One possible strategy to improve selectivity would be to incorporate porosity into the design of the powder. In, Chapter 3, a description of the protocols used to generate porous materials along with the characterization of material produced is provided. In Chapter 4, the sensor response of the porous material was tested to a series of alcohols of various sizes. Detection selectivity is shown and has been attributed to size selectivity in the alcohol adsorption in the pore structure of the WO_3 . In Chapter 5, an alternative approach to acquire detection selectivity is investigated. A combination of IR measurements and sensor test data was collected for DMMP and methanol adsorption under UV illumination.

Chapter 2

EXPERIMENTAL

In this chapter we describe the materials and general procedures used to synthesize and characterize the porous WO_3 . Each subsequent chapter also contains a brief experimental section describing the specific details related to that work. For example, in this chapter we describe the materials and details of the preparation of the ion exchange column and surfactant solutions, whereas a detailed description of specific reaction conditions for the synthesis of the various porous oxides are provided in Chapter 3.

2.1. Materials

Starting materials were obtained from the Aldrich Chemical Company. For the synthesis of porous WO_3 , the chemicals used were the ion exchange resin (DOWEX 50 WX2-200), sodium tungstate dihydrate (99%), ammonium tungstate, ammonium hydroxide (28%), commercial monoclinic tungsten (VI) oxide powder (1-5 microns 99.9%) as well as the cationic surfactants cetyltrimethyl ammonium bromide (CTAB, $(\text{CH}_3)_3\text{N}^+(\text{CH}_2)_{15}(\text{CH}_3) \text{Br}^-$) and cetyltrimethyl ammonium chloride (CTAC, $(\text{CH}_3)_3\text{N}^+(\text{CH}_2)_{15}(\text{CH}_3) \text{Cl}^-$) 25% solution.

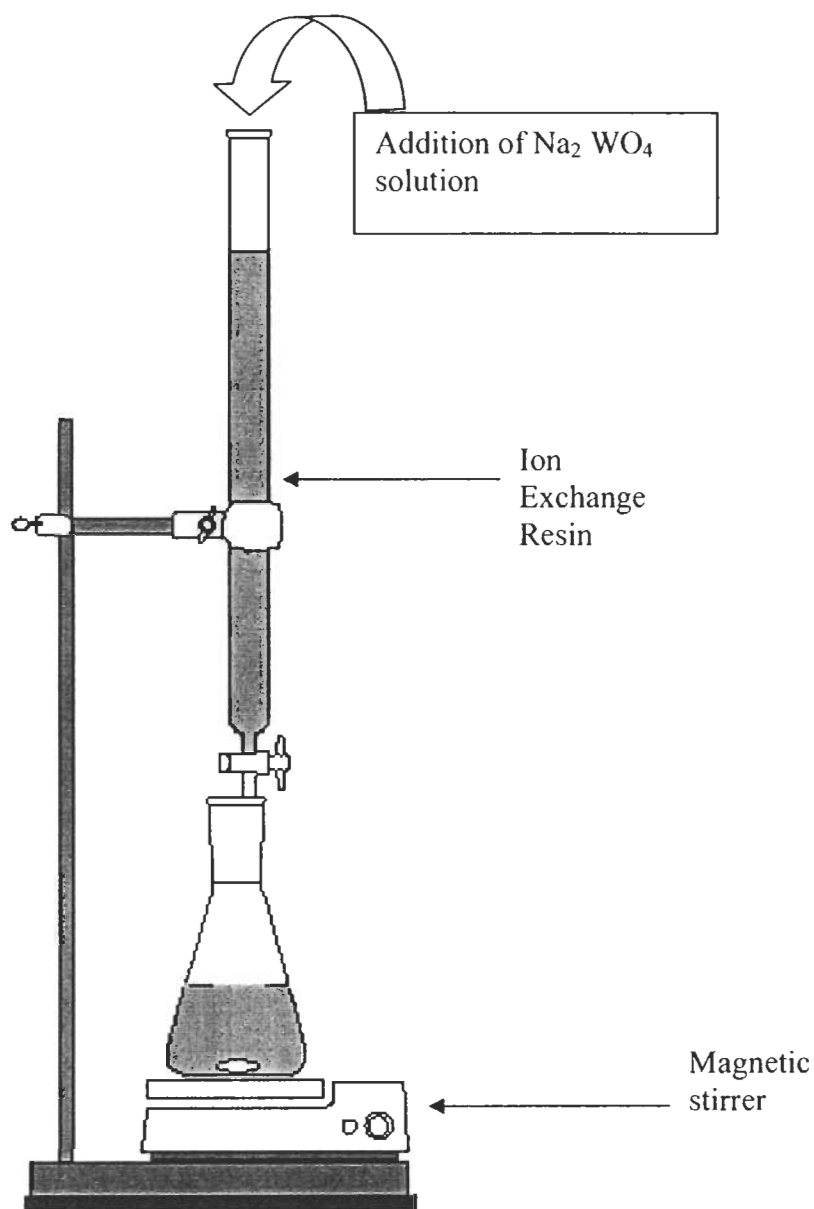


Figure 2.1. Experimental setup for preparation of sol (H_2WO_4 solution) using ion exchange resin.

2.2. Synthesis of Tungsten Trioxide

Both Na_2WO_4 and $(\text{NH}_4)_2\text{WO}_4$ were used as precursors in the sol-gel preparation of WO_3 . The Na_2WO_4 and $(\text{NH}_4)_2\text{WO}_4$ were converted to H_2WO_4 by acidification with HCl . Particular care was needed when using Na_2WO_4 because the presence of Na^+ ions in H_2WO_4 during the synthesis of WO_3 leads to mixed products of WO_3 and sodium tungstates.^{41,65} Therefore, Na_2WO_4 was first passed through an ion exchange resin to remove Na^+ ions prior to addition to the surfactant solution.

The experimental setup for performing the ion exchange is shown in Figure 2.1. All glassware was ultrasonically cleaned with soap and water and rinsed thoroughly with deionized water three times before use. 35 g of Dowex 50WX2-200 resin was first washed with 400 mL of DI water 3 times to remove excess sulfuric acid. Then resin was transferred into a standard 50 mL buret. A small wad of cotton covered by a Teflon film was inserted at the bottom of the buret. The 35 g of the ion exchange resin was loosely packed in a standard 50 mL buret. Deionized water was passed through the column until the pH of the water effluent was 5-6 (measured with pH paper) (pH of double distilled water was 5.8). Alternatively a solution of silver nitrate could be used to test for residual Cl^- ions.

2.2.1. Preparation of Tungstic Acid Solution

A predefined amount of sodium tungstate dihydrate (or ammonium tungstate) was dissolved in a 100 mL volumetric flask of double distilled water. The amount of solute depends on the concentration used in the experiments and this typically was 0.12 M. The solution of sodium tungstate dihydrate was added to a hydrogen ion exchange column

and eluted at a rate of 0.5 mL / min. With too high a rate of elution, sodium ions appear in the tungstic acid solution. Our experience in working with the ion exchange column showed that there is a narrow operational range between solution concentration, amount of resin used, and elution rate. Using higher concentrations of Na_2WO_4 or less resin in the column leads to mixtures of WO_3 and sodium tungstate whereas using more resin and slow elution rates clogged the column with polymerized WO_3 sol. Collection of effluent began when the solution pH was 1.5 or lower.

The receiving flask contained the assembled surfactant architectures and upon addition of the H_2WO_4 exiting the ion exchange the templating process commenced. The experimental conditions used in this stage are detailed in Chapter 3. After completion of the sol-gel process, the final step is calcination at elevated temperature to remove the surfactant and convert the hydrated WO_3 into monoclinic form.

2.2.2. Calcination

To obtain the stable monoclinic form of WO_3 , the tungsten trioxide dihydrate was calcinated at 500 °C. Several heating protocols were tested and it was found that the higher the calcination temperature, the lower the surface area of the particle. Although monoclinic WO_3 was obtained at a minimum 400°C, the samples needed to be heated to at least 500°C. At temperature below 500 °C, the samples reverted to their amorphous hydrated form. The calcination step was also needed to burn off the surfactant leaving behind open channels inside the hardened WO_3 lattice.

The heating rate was found to be an important parameter in dictating the final structure. A fast heating rate led to collapse of the mesoporous structure, agglomeration

of the water-laden particles, and reduction in the surface area. To minimize the structural collapse, the samples were first heated at 150 °C to remove water, then the material was dried at a temperature ramp rate set between 1 and 10 °C/ min to the temperature of 500 °C and held at this temperature for 6 hours, followed by cooling to room temperature at a rate of 20 °C / min.

2.3. Characterization of Tungsten Oxide Powders

Porous materials are principally identified by adsorption isotherms, XRD patterns and transmission electron microscopy. However, in our case, the powders were first analyzed by infrared and Raman spectroscopy because this instrumentation was readily available in our laboratory and provided a quick screening method of the samples before proceeding to adsorption isotherm, XRD and TEM measurements.

2.3.1. Raman Spectroscopy

Raman spectroscopy was used because of the ease in identifying characteristic bands for sodium tungstates, hydrated tungsten oxide and WO_3 .^{42,66-70} For all samples except those that used Na_2WO_4 directly (no ion exchange), characteristic sodium tungstate bands in the 940-960 cm^{-1} range were not detected⁷⁰. A spectrum of the hydrated tungsten oxide and tungsten oxide with sodium is shown in fig 2.2. For comparison, a Raman spectrum of a typical porous sample and a commercial powder is shown.

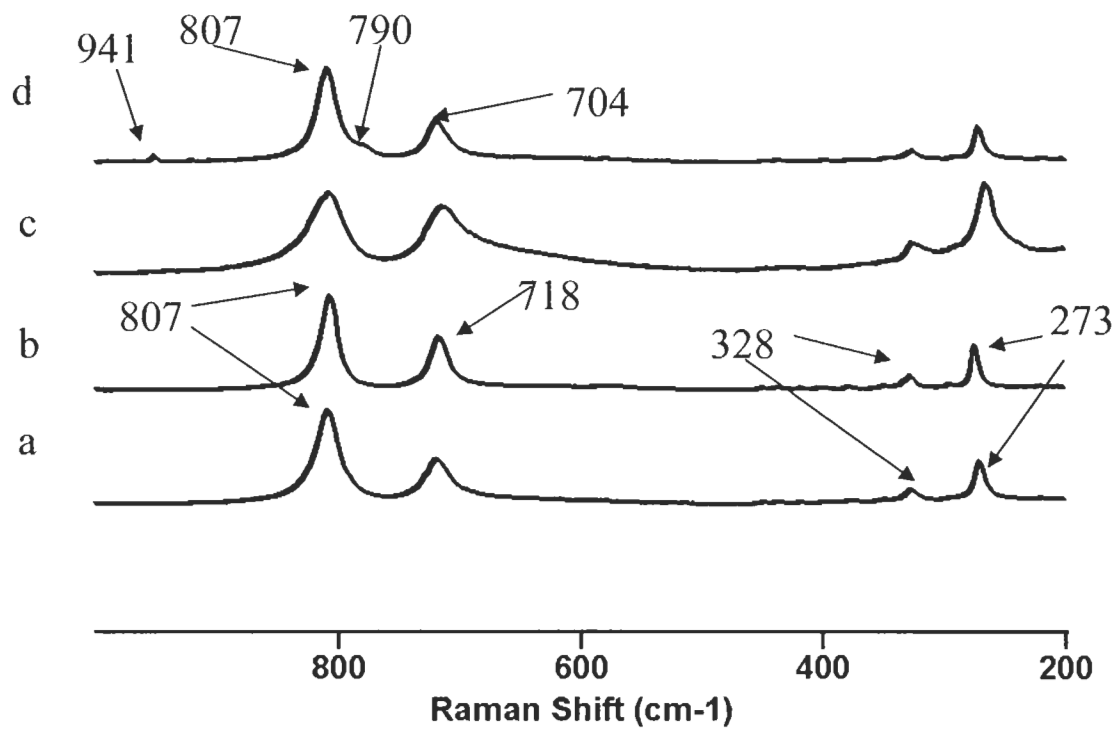


Figure 2.2. Raman Spectra of (a) porous WO₃ sample A1 (b) nonporous WO₃ sample C (c) hydrated WO₃ and (d) WO₃ produced using Na₂WO₄ without ion exchange

The similarity between Figure 2.2 a & b show that little, if any, hydrated tungsten oxide remains upon calcination. Major Raman bands at 807, 718 cm^{-1} (W-O stretching modes) and 273 and 136 cm^{-1} (W-O bending modes, 136 cm^{-1} is not shown) in Figure 2.2 a and b are characteristic of monoclinic WO_3 . Miyakawa *et al.*⁷¹ have shown that the Raman bands at 807 and 718 cm^{-1} were observed for monoclinic WO_3 and do not change as a function of temperature indicating formation of highly stable monocrystalline WO_3 at temperatures up to 500 °C. 328 cm^{-1} is a WO_3 lattice mode.

Raman spectra were collected using a Renishaw Raman Imaging Microscope System 1000. The system is equipped with a diode laser having $\lambda_{\text{ex}} = 785 \text{ nm}$. Signal detection is archived through the use of a sensitive charge coupled device (CCD) array detector.

2.3.2. Infrared Spectroscopy

Infrared spectroscopy was used to detect the presence of residual surfactant (absence or appearance of C-H modes) and as a quick assessment of particle size and surface area. In brief, a smaller particle size exhibits less scattering of the infrared beam and is accompanied by more intense surface W-OH and adsorbed water modes.³³

FTIR spectra were recorded on a Bomem MB-Series spectrometer with a liquid N_2 cooled MCT detector. Typically 200 scans were co-added at a resolution of 4 cm^{-1} . Spectra were recorded in transmission using a thin film technique⁷² or Diffuse Reflection Infrared Fourier Transform (DRIFT) using a Harrick Preying Mantis apparatus equipped with an environmental chamber.

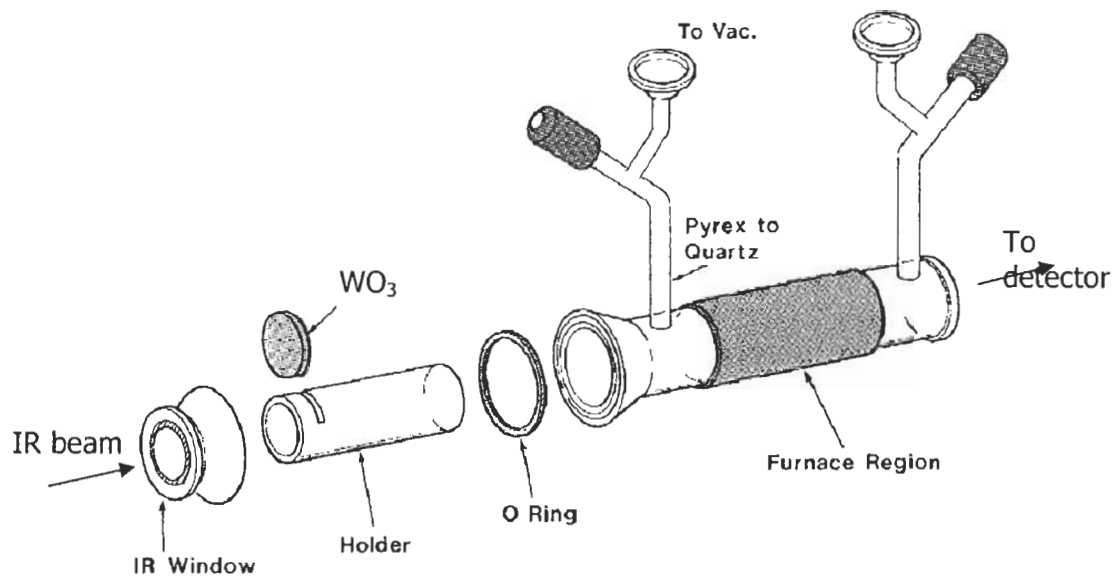


Figure 2.3. Transmission cell used for IR experiments

The transmission cell is shown in Figure 2.3. The WO_3 powder was dispersed on an infrared window using minimal pressure and inserted into the cell. The cell was placed in the FTIR and could be evacuated by connection to a standard glass vacuum line or operated in a flow through arrangement using a carrier gas. The cell contained a furnace region which enabled operation from ambient to $600\text{ }^\circ\text{C}$. Standard vacuum line techniques were used to deliver gaseous compounds to the cell.

The DRIFT apparatus shown in Figure 2.4 was used in the UV illumination experiments. This cell was used instead of the transmission cell because the environmental chamber contained a glass viewing port which enabled UV illumination during collection of IR spectra.

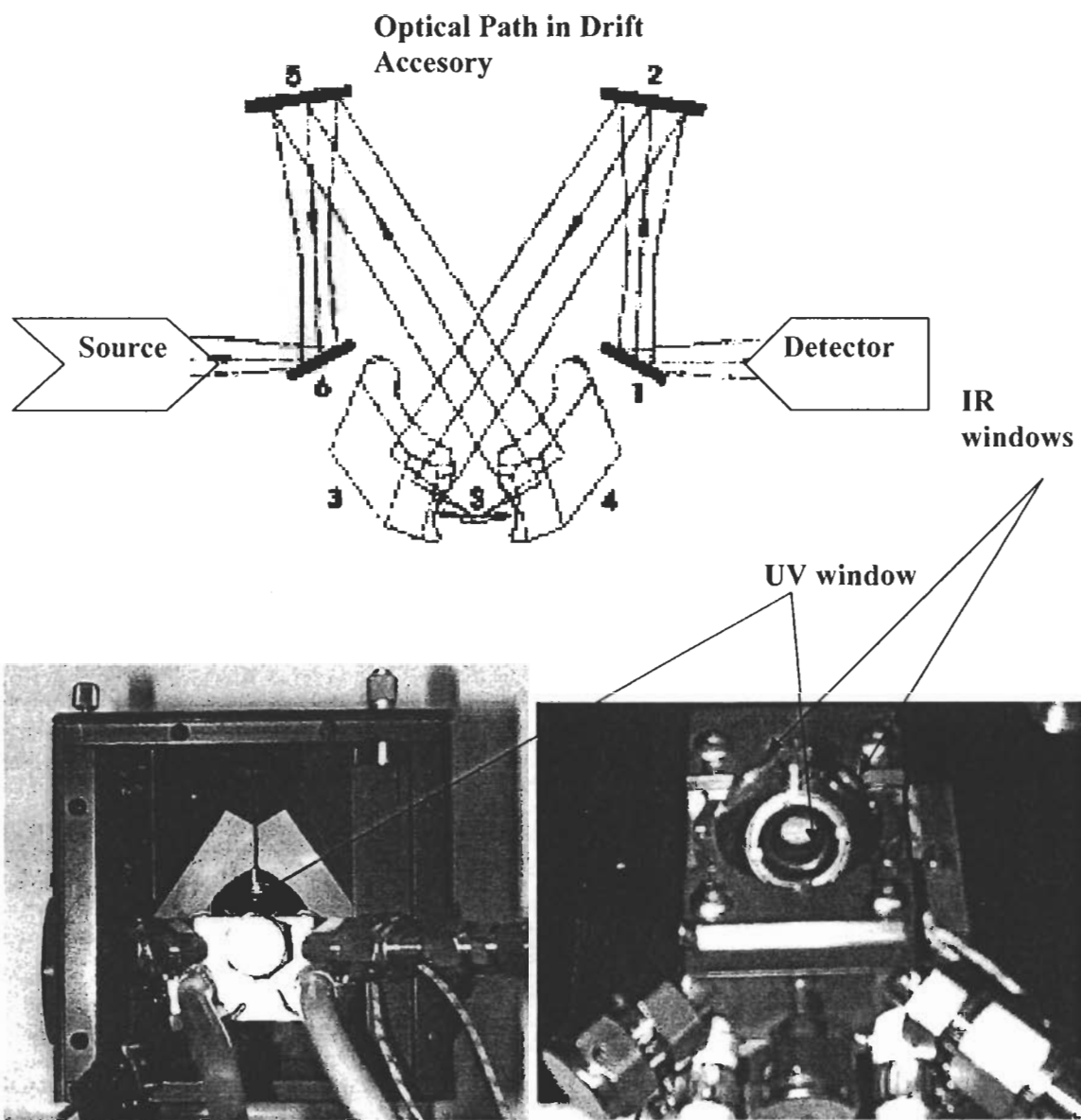


Figure 2.4. DRIFT apparatus for IR measurements.

2.3.3. BET (Brunauer Emmett and Teller) Surface Area Measurement

N₂ adsorption isotherms were used to measure surface area and pore size of the mesoporous WO₃. Brunauer-Emmett-Teller (BET) surface area measurements for WO₃ powders were recorded on a Gemini 2360 Surface Area Analyzer Micromeritics instrument. The surface area measurement in this system is based on the volume of nitrogen uptake by a known amount of sample at liquid nitrogen temperature. Samples were degassed at 150 °C for 4 hours under dry nitrogen flow. Nitrogen and helium pressure was maintained to 25~30 *p.s.i.*. The precision of the data from surface area was +/- 0.2 m²/g at the 95% confidence level.

The Brunauer, Emmett and Teller (BET) technique is one of the most widely used techniques in surface area measurements because of its high reproducibility in measuring the surface area of a wide variety of porous substances. This method was first described in 1938.⁷³ For more reliable results, the sample is first degassed by heating the solid sample to about 110 °C to 150 °C under dry nitrogen flow or vacuum to get rid of absorbed water and other gases from the sample. The solid sample vessel in vacuum is cooled to approximately -196 °C using a liquid nitrogen Dewar. Then the amount of N₂ adsorbed by the sample at liquid N₂ temperature is measured at various partial pressures of N₂ up to the saturation pressure. The saturation pressure for nitrogen is generally close to the atmospheric under experimental conditions. The slight deviations from atmospheric pressure are primarily due to dissolved oxygen and other impurities in the liquid nitrogen surrounding the sample tube. These impurities raise the boiling temperature of liquid nitrogen.⁷⁴

The experimental data of BET is generally expressed as an isotherm plot of adsorbed volume of N₂ as a function of partial pressure. The partial pressure is calculated as a ratio of applied pressure to saturation pressure. Typical adsorption desorption curves are shown in Figure 2.5. The top curve is a desorption isotherm, where readings are first taken at the saturation pressure and then the pressure is systematically reduced and the nitrogen evolved is measured. In the lower adsorption curve, the isotherm is measured by starting at low N₂ pressure and then measuring the volume of nitrogen adsorbed at gradually increasing pressure.

The surface area is calculated from the adsorptive branch of the isotherm using the BET equation for multilayer adsorption equation 2.1,

$$\frac{P}{V(P_o - P)} = \frac{1}{V_m C} + \frac{C-1}{V_m C} \frac{P}{P_o} \quad (\text{Eqn.2.1})$$

Where,

P and P_o are the equilibrium pressure and the saturation pressure of nitrogen at the liquid nitrogen boiling temperature, respectively.

V is the volume adsorbed at the pressure P (mL STP per gm of the solid adsorbent)

V_m is the volume of the nitrogen corresponding to one complete monolayer of adsorbed gas (mL STP per gm of solid adsorbent), and C is a constant.

For most compounds the BET equation applies reasonably well in relative pressure range 0.05 to 0.35. A plot of $\frac{P}{V(P_o - P)}$ vs P/P_o produces a straight line where the monolayer volume V_m can be calculated from the slope and intercept. The surface area of the sample is calculated from determining V_m assuming the area of a nitrogen molecule is 16.2 \AA^2 .⁷⁵

2.3.4. Porosity and Pore Size Distribution

Adsorption isotherms can also be used to distinguish between porous and nonporous materials. “An adsorption isotherm is a plot of the equilibrium amount of a substance adsorbed (in terms of coverage or uptake) against pressure of the adsorbing substance in the gas phase, measured at constant temperature.”⁷⁷ These isotherms are measured using either gravimetric or volumetric techniques. The IUPAC Commission on Colloid and Surface Chemistry recommended classifying sorption isotherms in porous media according to their qualitative behavior⁷⁸ and they fall in six categories for adsorption systems. The calculations of the pore size distribution are based upon the measurements made at high relative pressure in the hysteresis loop area of Figure 2.5.

Figure 2.6 shows these isotherms. A type I isotherm is a typical “ideal” chemisorption process where the amount adsorbed increases and reaches a plateau at $\theta=1$ and no further adsorption occurs.

Here θ is the fractional coverage and it is given by formula

$$\theta = \frac{N_{ads}}{N_m} \quad (\text{Eqn. 2.3})$$

where,

N_{ads} : Number of adsorbate atoms per unit area

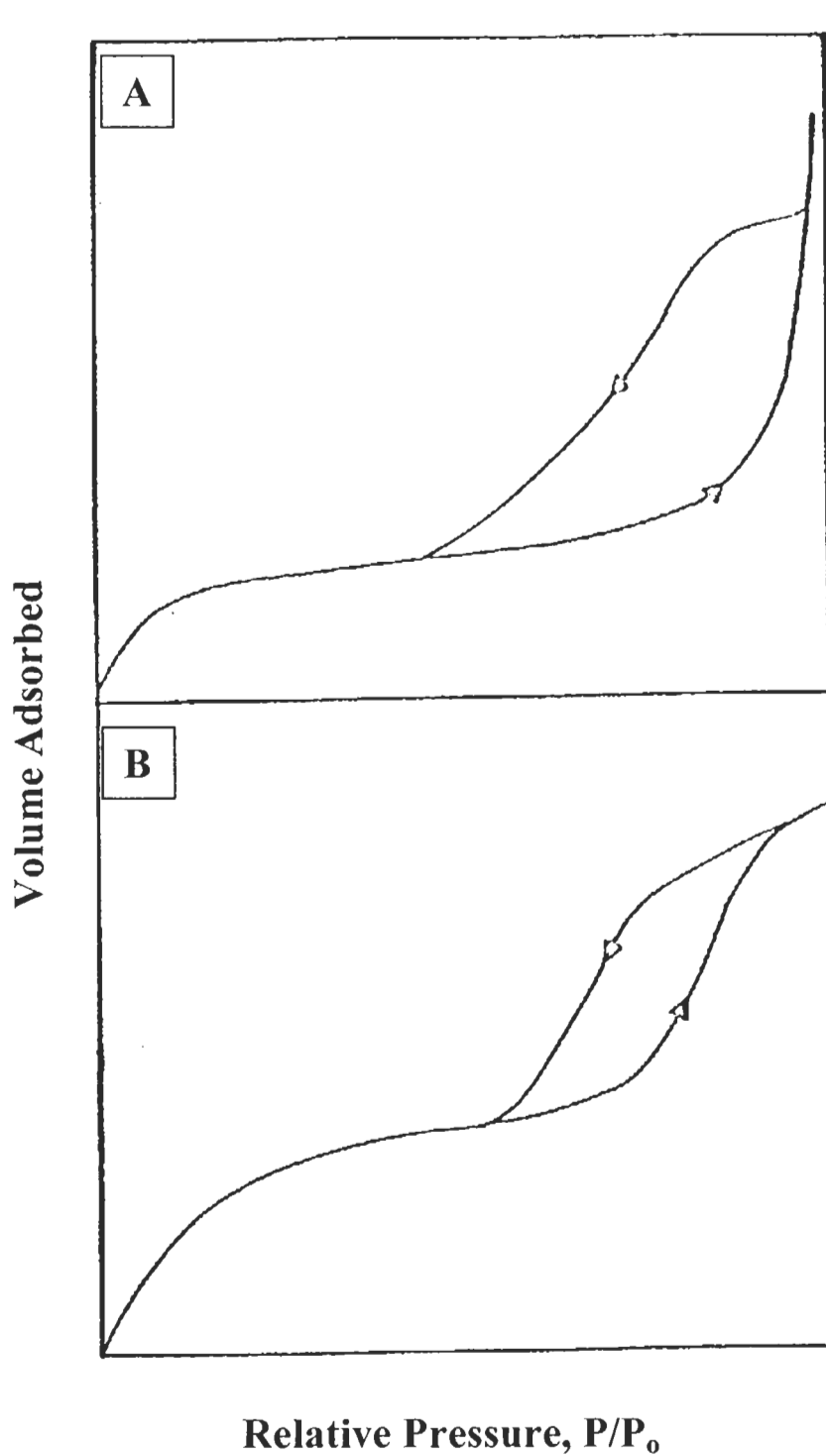


Figure 2.5. Desorption (top part of hysteresis loop) and Adsorption (bottom part of hysteresis loop) curves. Plot A starts with filled pores and Plot B starts with empty pores showing hysteresis in type IV isotherm.⁷⁶

N_m : the number of atoms/molecules adsorbed per unit area to produce one complete monolayer on the surface.

In the case of physisorption, a type II type isotherm is observed where the monolayer plateau is first obtained followed by a second increase at higher partial pressure due to multilayer adsorption. Type III adsorption is associated with multilayer formation from the onset. Type II and Type III are characteristic of multilayer adsorption on nonporous materials with type II due to strong and type III weak interactions between the solid and gas adsorbate. Types IV and V occur when multilayer adsorption occurs on a porous material with corresponding strong and weak fluid and solid interactions, respectively. Type VI interaction occurs when there is a strong fluid to wall interaction in nonporous materials at a temperature close to the melting point of the adsorbed gas.⁷⁹

Mesoporous materials give rise to type IV isotherms for N_2 adsorption whereas their nonporous equivalents produce type II isotherms. The origin of the second sharp rise in the type IV adsorption isotherm distinguishes the isotherm from a type II isotherm and its origin is illustrated in the four stage process shown in Figure 2.7.

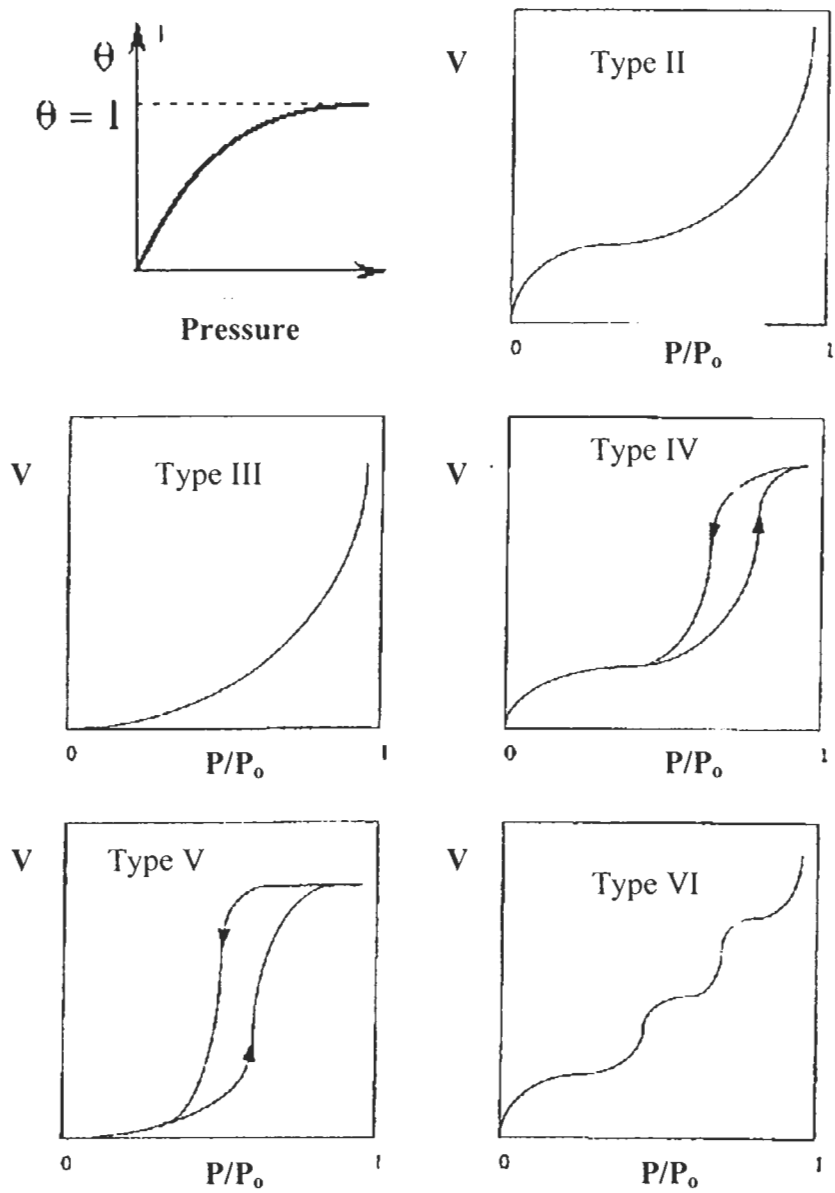


Figure 2.6. Adsorption isotherms shown as coverage θ or volume versus partial pressure of the gas⁷⁷

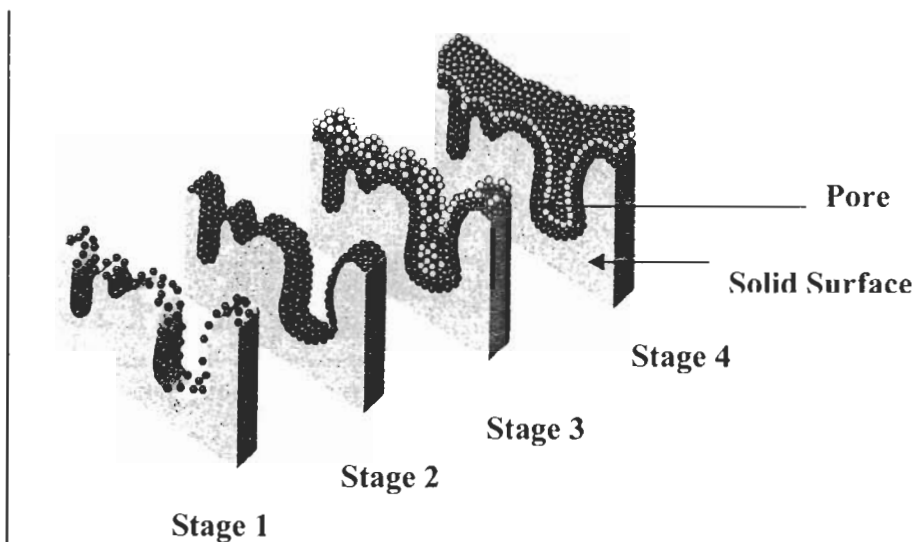


Figure 2.7. Different stages in adsorption of gas molecules on a surface.

Stage 1: Isolated sites on the sample surface begin to adsorb molecules at low pressure.

Stage 2: As the gas pressure increases, the coverage of molecules increases to form a contiguous layer.

Stage 3: Further increasing the gas pressure will cause the beginning of multilayer coverage. If the material is porous, the pore wall fills due to capillary action, producing the second rise in a type IV character adsorption isotherm curve. Smaller pores in the sample will get filled first.

Stage 4: Still further increases in the gas pressure will cause complete coverage of the sample and fill all the pores.

Various adsorption models can be used to determine pore diameter, volume and distribution. Type IV behavior, also known as “hysteresis behavior”, provides information on the porous substrates (see Figure 2.5). This behavior is a characteristic

property of porous media where evaporation from pores requires much more energy than the condensation in pores. Evaluation of the adsorption and desorption branches of type IV isotherms and the hysteresis (Figure 2.5) that occurs between the two branches is used to extract information about pore size, pore volume, and pore shape. Pore volume and pore distribution is generally calculated using the Barrett, Joyner, and Halenda (BJH) method and requires both branches of the hysteresis curve.⁸⁰ Given that the Gemini 2360 could only provide the adsorption branch of the isotherm, we have used Saito and Foley's established method⁸¹ to calculate the pore size for our tungsten oxide powders.

Saito and Foley's cylindrical model is an extension of the slit model by Horvath and Kawazoe⁸². Their assumption was a slab wall geometry with the slit walls comprised of two infinite graphite planes and adsorption occurs on two parallel planes. Saito and Foley proposed a cylindrical model with some assumptions (see Figure 2.8) The assumptions in Saito and Foley's cylindrical model are:

- (1) pores are perfect cylinders of infinite length but finite radius,
- (2) The inside walls of these cylinders are a single layer of atoms or oxide ions which is taken as a continuum of potential interaction. The interaction with the pore wall was taken to be due to only the dispersion forces as assumed by the Horvath and Kawazoe model⁸².
- (3) Adsorption occurs only on the inside wall of a cylinder.
- (4) The interaction of adsorption is taken to be only between the adsorbate and the adsorbent with adsorbate as an oxide ion in mesoporous materials.

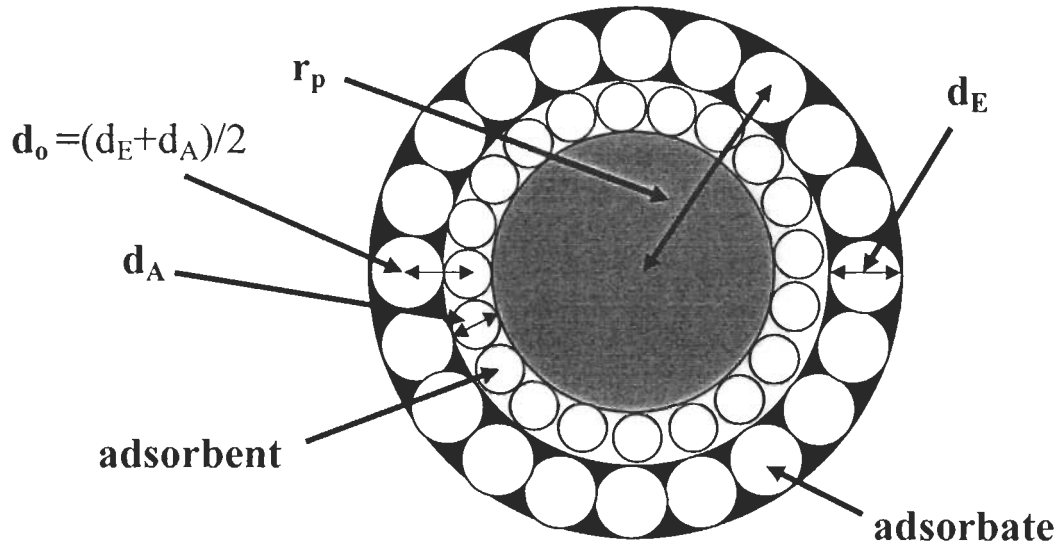


Figure 2.8. Cylindrical geometry where r_p : radius of pore, d_o : mean diameter, d_A : adsorbate diameter, d_E : adsorbent diameter ($d_o = 0.5(d_A + d_E)$)

Utilizing the parameters for the physical properties of surface oxide ion and N_2 as the adsorbate, the cylindrical model equation 2.4 is:

$$\ln\left(\frac{P}{P_o}\right) = 36.27 \sum_{k=0}^{\infty} \left[\frac{1}{k+1} \left(1 - \frac{0.288}{r_p}\right)^{2k} \times \left\{ \frac{21}{32} \alpha_k \left(\frac{0.288}{r_p}\right)^{10} - \beta_k \left(\frac{0.288}{r_p}\right)^4 \right\} \right] \quad (\text{Eqn 2.4})$$

where,

d_o : arithmetic mean of the diameter of adsorbent molecules in the wall and the adsorbate atom.

r_p : radius of the pore

The expression coefficients α_k and β_k in above equations are given in equations 2.5 and 2.6

$$\alpha_k = \left(\frac{-4.5 - k}{k} \right)^2 \alpha_{k-1} \quad (\text{Eqn 2.5})$$

$$\beta_k = \left(\frac{-1.5 - k}{k} \right)^2 \beta_{k-1} \quad (\text{Eqn 2.6})$$

where both α_0 and β_0 are equal to 1.

k is the index and it was varied from 0 to 100 as a close approximation to infinity for calculation purpose

Equations 2.4, 2.5 and 2.6 provide the relationship between the micropore size and relative pressure. This model gives the effective pore diameter (D_{eff}) after correcting for the diameter of the tungsten oxide⁸³ with substituting for d_0 equation 2.7.

$$D_{\text{eff}} = 2r - 0.276 \text{ nm} \quad (\text{Eqn. 2.7})$$

The change in volume per change in D_{eff} plotted against D_{eff} (dV/dD_{eff}) gives values for the pore diameters and pore size distribution plots that are shown in chapter 3.

Unfortunately, we could not verify to our satisfaction if these approximation can give sufficiently reliable results for mesoporous materials. We believe additional information from desorption isotherm may provide that information. Our group may acquire these facilities in near future and we may reveal additional data in future.

2.3.5. X-ray Diffraction (XRD)

XRD also provides key evidence for the existence of a mesoporous structure. In addition to the peaks identifying the crystalline structure of the material, the long range periodic pore structure leads to characteristic peaks at low 2θ values. All XRD measurements were performed using a X2 Advanced Diffraction System which was equipped with a copper anode and a simple crystal lithium doped silicon peltier detector which has a 100% energy absorption from 2-20 Kev with a Beryllium window thickness of 0.005 inches. $\lambda_{\text{Cu K}\alpha} = 1.5406 \text{ \AA}$

2.3.6. Scanning Electron Microscopy (SEM)

Particle size and shape was obtained by Scanning Electron Microscopy (SEM). SEM pictures were taken on an AMRay 1000 instrument at the University of Maine. This instrument has a resolution of 7 nm, a magnification range of 20-100,000 X and accelerating voltage range of 1-30 kV. The powders were mounted on a eucentric goniometer stage, which enabled both tilt and rotation about the viewing axis.

Sample Preparation: Samples were suspended and/or diluted in 95% ethanol. Several droplets of a sample were applied to a carbon underlayment on an aluminum specimen support stub. The suspension was allowed to settle, and dry. After the samples were fully dry (overnight), they were sputter-coated with 200 angstroms of gold using a Conductavac I sputter-coater (Seevac Inc. Pittsburg PA). Samples were examined using an AMRay 1000 SEM (AMRay Inc. Bedford MA), at 5 and 20 kilovolts. Polaroid type 665 positive/negative film was used for capturing images.

2.3.7. Transmission Electron Microscopy (TEM)

Dilute ethanol suspensions of the samples were applied drop-wise to specimen support grids with carbon-coated pioloform as a substrate. Suspensions were allowed to settle (approximately 2 minutes), and the remaining droplets blotted dry from the grid edge using hardened filter paper. After the samples were fully dry, they were examined with a Philips CM-10 TEM (Philips Electronics N.V., Eindhoven, The Netherlands) using a mean energy of 100KV. Photographs were taken using a Gatan Bioscan model 792 digital camera (Gatan Inc. Pleasanton CA) running Digital Micrograph version 3.3.1, for the Macintosh Operating System.

Chapter 3

SYNTHESIS OF POROUS MONOCLINIC WO₃ USING CATIONIC SURFACTANT TEMPLATING METHODS.

3.1. Introduction

An increase in the surface area of WO₃ powders using synthetic methods involving chelating agents or emulsion polymerization³² occurred because these methods produced smaller sized particles. These WO₃ powders had surface areas of about 20 m²/g (chelating agents) and 45 m²/g (emulsion) giving rise to primary particle diameters of about 40 nm and 18 nm, respectively. A substantial increase in surface area by using synthetic methods to further reduce the particle size would be difficult because an 18 nm diameter particle is near the practical lower size limit for metal oxide powders.

Alternatively, much higher surface areas could be achieved by incorporating porosity into the WO₃ particles. For example, nonporous silica particles produced by high temperature flame hydrolysis typically have surface areas of 50 m²/g to 300 m²/g with particle diameters of 40 nm to 7 nm⁸³. In contrast, precipitated silica gels are much larger in size, (> 1 μm in diameter) but these materials have surface areas of 250 m²/g to 700 m²/g due to their porous nature⁸⁴. The highest surface areas are achieved for mesoporous silica and these are in the range of 1100 to 1500 m²/g⁸⁵. Based on these surface areas obtained for mesoporous silica, we would anticipate a substantial increase in surface area with the successful fabrication of mesoporous or porous WO₃ powders.

The last decade has seen an explosion in the synthesis of a variety of novel mesoporous oxides whose structure and shape are defined by the self-assembled architecture of surfactants and polymers. The attraction lies in the simplicity in which the mesoporous structure can be tailored. Various architectures are possible by varying reaction parameters such as the nature and concentration of surfactant, choice of solvent, pH, ionic strength and drying/calcination protocol. Most of the work has been targeted to silica based mesoporous materials templated with ionic surfactants and this area is well established and developed.⁸⁶ In contrast, there is much less work in defining synthetic routes leading to the fabrication of non-silica based mesoporous oxides even though these mesoporous oxides will have use in many industrial applications.⁸⁷ The problem is that non-silica oxides are typically more difficult to fabricate into mesoporous structures because they are more susceptible to hydrolysis, redox reactions, phase transitions and often the structure collapses during the calcination step. Despite these synthetic challenges, various non-siliceous mesoporous materials such as Al_2O_3 ⁸⁷, Ta_2O_5 ⁸⁸, SnO_2 ⁸⁹, TiO_2 ^{90,91} and Nb_2O_5 ⁹² have been produced.

Most of the literature recipes used to generate mesoporous oxides rely on the use of ionic surfactants as the templating agent. From our perspective, the simplest approach would be to apply and if necessary, adapt the established protocols used for other oxides to the synthesis of novel mesoporous WO_3 powders. However, fabrication of mesoporous structures using Group VI elements such as tungsten are especially problematic because of their tendency to form stable ionic compounds rather than a polymerized oxide network.⁹³⁻⁹⁵ As a result, the synthesis of WO_3 particles using ionic

surfactant based recipes have not been reported because the presence of common ions (Na^+ , NO_3^- etc.) leads to mixtures of WO_3 and tungstate salts^{41, 65}.

Current methods to prepare WO_3 generally start by passing Na_2WO_4 through an ion exchange column followed by a condensation of the eluted H_2WO_4 in a solution containing nonionic surfactants or polymers. Nano-sized WO_3 powders have been recently fabricated using nonionic surfactant based emulsion polymerization⁹⁴ and the first example of mesoporous WO_3 has been reported using self-assembly of nonionic PEO as the templating molecule⁹⁶.

The need to exclude common ions and ionic surfactants in generating mesoporous WO_3 drastically reduces the number of synthetic routes and thus limits the number of possible architectures that could be generated for mesoporous WO_3 . In this chapter, we show that the synthesis of monoclinic WO_3 powders is not limited to nonionic surfactants and polymers. In particular, we describe the synthetic protocols that lead to porous WO_3 generated with the same cationic based synthetic procedures used to fabricate MCM-41 and MCM-48 metal oxide powders. While it is not clear that we have obtained mesoporous material because the high calcination temperatures collapses the templating architecture, it is found that the final material morphology and properties can be altered by using different surfactant templating architectures. Moreover, the resulting materials produced by surfactant templates are of interest because they are porous with high surface areas.

Three synthetic approaches leading to porous WO_3 are compared. In the first approach, Na_2WO_4 is passed through an ion exchange column to remove Na^+ ions and the H_2WO_4 exiting the column is added to a solution containing cetyltrimethylammonium

bromide (CTAB). In a second approach, the Na_2WO_4 dissolved in water is added directly to the CTAB solution. In a third approach, we have used NH_4WO_4 as a precursor in an attempt to develop methods that avoid the need for ion exchange. The WO_3 materials were characterized by XRD, TEM, SEM, N_2 adsorption isotherms, infrared and Raman spectroscopy.

3.2. Experimental

3.2.1 Synthesis of Porous WO_3 using MCM-41 Type Templating Architecture

The experimental procedures for preparing the ion exchange columns, tungstic acid and post calcination procedures are described in chapter 2. WO_3 was prepared by adding the H_2WO_4 effluent from the ion exchange column to an aqueous CTAB solution that is commonly used in the preparation of MCM-41 mesoporous silica.⁹⁷ In brief; 0.6 g of CTAB was dissolved in 5 mL of deionised water and stirred until the solution was homogeneous and clear. Then 2 mL of NH_4OH (32 wt %) was added to the CTAB solution and the solution was stirred for an additional 5 min. Next 25 mL of a freshly eluted solution of H_2WO_4 was then added to the CTAB solution; the solution was stirred for 24 hours and then allowed to continue the sol-gel polymerization process without stirring at ambient temperature for an additional 48 hours. The resulting yellow powder was filtered, then washed sequentially with ethanol and deionised water. The dried powder was then calcinated at 500°C for 5 hours. The temperature was raised at $1^\circ\text{C}/\text{min}$ to 500°C and was decreased at a rate of $20^\circ\text{C}/\text{min}$ to ambient temperature. The calcination step served a dual purpose of burning off the surfactant and conversion of the hydrated WO_3 to the monoclinic form of the oxide.³²

3.2.2. Synthesis of Porous WO₃ using MCM-48 Templating Architectures

MCM-48 type materials were prepared by adopting standard recipes used in the synthesis of mesoporous silica.⁹⁷ First, CTAB (1.6 g, 4.4 mmoles) was dissolved in 7 g of distilled water and this was added to 33 mL of technical grade ethanol (0.58 mol) and 8.5 mL of aqueous NH₄OH (29.2 wt %, 0.14 moles). The solution was stirred for 10 min and then 25 mL of eluted H₂WO₄ solution (10 mmoles of WO₃) was added. The mole ratio of the solution prepared was 1 mol WO₃: 12.5 mol: NH₄OH: 54 mol EtOH: 0.4 mol CTAB: 174 mol H₂O. The mixture was stirred for 24 hrs and then left undisturbed at room temperature for an additional 48 hours. The precipitate that formed was filtered and then washed with ethanol and then with deionised water. The calcination protocol was the same as used in section 3.2.1.

3.2.3 Synthesis of Porous WO₃ using (NH₄)₂WO₄·2H₂O

To fabricate porous WO₃ using (NH₄)₂WO₄·2H₂O, we used the same MCM-48 type recipe with some minor modifications. First, 0.15 mL of 37.5% HCl was diluted with 3 mL deionised water and to this 0.5 g CTAB (1.5 mmoles) was added with stirring. After a uniform and clear solution was obtained, 1 g of (NH₄)₂WO₄·2H₂O was added and the solution was stirred for 1 hour at ambient and then allowed to stand overnight at 90 °C. The solution was cooled to room temperature and the pH was adjusted to a value between 6 to 7 with 37% HCl. The solution was then reheated for 3 days at 90 °C to complete the sol-gel process. A light yellow precipitate forms and this was then washed with deionised water, dried and calcined at 550 °C for 6 h. A slightly higher calcination temperature of 550 °C was required to remove all evidence of ammonia and to convert the hydrated WO₃ to the monoclinic form.

The mole ratio of the reagents used in the synthesis of various WO_3 samples is listed in Table 3.1. For example, the molar ratio used to generate the MCM-41 sample labeled A1 was 1 mol $\text{Na}_2\text{WO}_3 \cdot 2\text{H}_2\text{O}$: 1.64 mol NH_4OH : 0.15 mol CTAB: 126 mol H_2O . Samples prepared using MCM-41 protocols are identified as A1 to A4 and those prepared using MCM-48 protocols are designated as B1 and B2. Two separate batches of each material were produced to test for reproducibility. The XRD patterns obtained for both batches of each material were the same.

3.3. Results And Discussion

3.3.1 Raman Spectroscopy

Raman spectra were recorded in order to assess the degree of conversion of the hydrated WO_3 to the monoclinic form and to detect the presence of sodium tungstates. In Figure 3.1, the spectrum of sample A1 in curve 3.1a is shown and this spectrum is identical to the spectrum of the nonporous sample C powder prepared by (curve 3.1b) an emulsion polymerization.³² The Raman spectrum for sample A1 is also identical to the spectrum obtained for samples A2, A3, B1 and B2 (spectra not shown). In figure 3.1a and 3.1b characteristic sharp bands at 811, 723, 330, 274 cm^{-1} due to various W-O modes of the monoclinic form of WO_3 are observed⁹⁸. The presence of hydrated WO_3 gives rise to characteristic broad bands at 807 and 704 cm^{-1} (see curve 3.1c) and these are not observed in the spectrum of sample A1 or C. The presence of sodium tungstates produce characteristic bands at 950 cm^{-1} with a shoulder at 790 cm^{-1} ^{66-71,99} and these too are not observed in the Raman spectra of samples A1 or C. In contrast, the Raman band due to

Table 3.1. Mole Ratios of Reagents

	Na ₂ WO ₄	NH ₄ OH	CTAB	Water	Ethanol
A1	1	1.64	0.15	252	0
A2	1	1.64	0.15	160	0
A3	1	1.64	0.15	126	0
B1	1	12.5	0.4	174	54
Ammonium Tungstate					
B2	1	12.5	0.4	174	54
Without column					
A4	1	1.64	0.15	252	0

sodium tungstates appears in sample A4 or when Na_2WO_4 is used as a precursor regardless of the initial concentration of the Na_2WO_4 (see curve 3.1d).

3.3.2. X-ray Diffraction (XRD)

Figure 3.2 shows the XRD pattern for sample A1 and a nonporous monoclinic WO_3 powder (sample C). Before calcination, sample A1 has numerous XRD peaks above $2\theta = 20^\circ$ along with a peak at $2\theta = 8.6^\circ$, whereas sample C shows weak broad peaks. After calcination both sample C and A1 show characteristic peaks above $2\theta = 20^\circ$ that are due to the monoclinic form of WO_3 . In the region below $2\theta = 20^\circ$, the XRD pattern of sample A1 (curve 3.2a) shows a sharp band at $2\theta = 7.32^\circ$ and this corresponds to a d-spacing of 12.0 Å. Peaks below $2\theta = 20^\circ$ are not present in the nonporous sample C and therefore bands in this region are characteristic of the longer range periodicity within sample A1.

An attractive feature of synthetic methods used in generation of MCM-41 type mesoporous oxides is that it is possible to tune the pore size through changes in the synthetic procedures and conditions. For example, it has been shown that an increase in the Si precursor to CTAB ratio leads to different types of mesoporous silica.^{97, 100-104} Samples A2 and A3 are prepared using MCM-41 based recipes in which the tungstic acid to CTAB is kept constant and the CTAB to water ratio is increased. By increasing the CTAB to water ratio, the packing density of the rod-like micelle in the templating architecture increases.¹⁰⁵

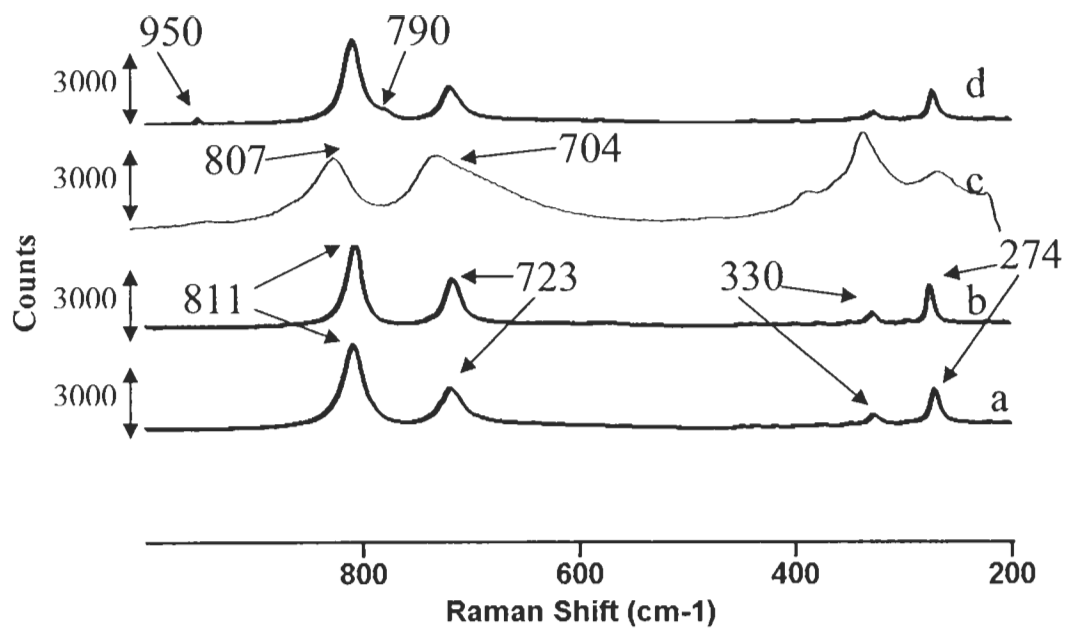


Figure 3.1. Raman Spectra of (a) sample A1 (b) nonporous WO₃ sample C (c) hydrated WO₃ and (d) WO₃ produced using Na₂WO₄ without ion exchange (sample A4).

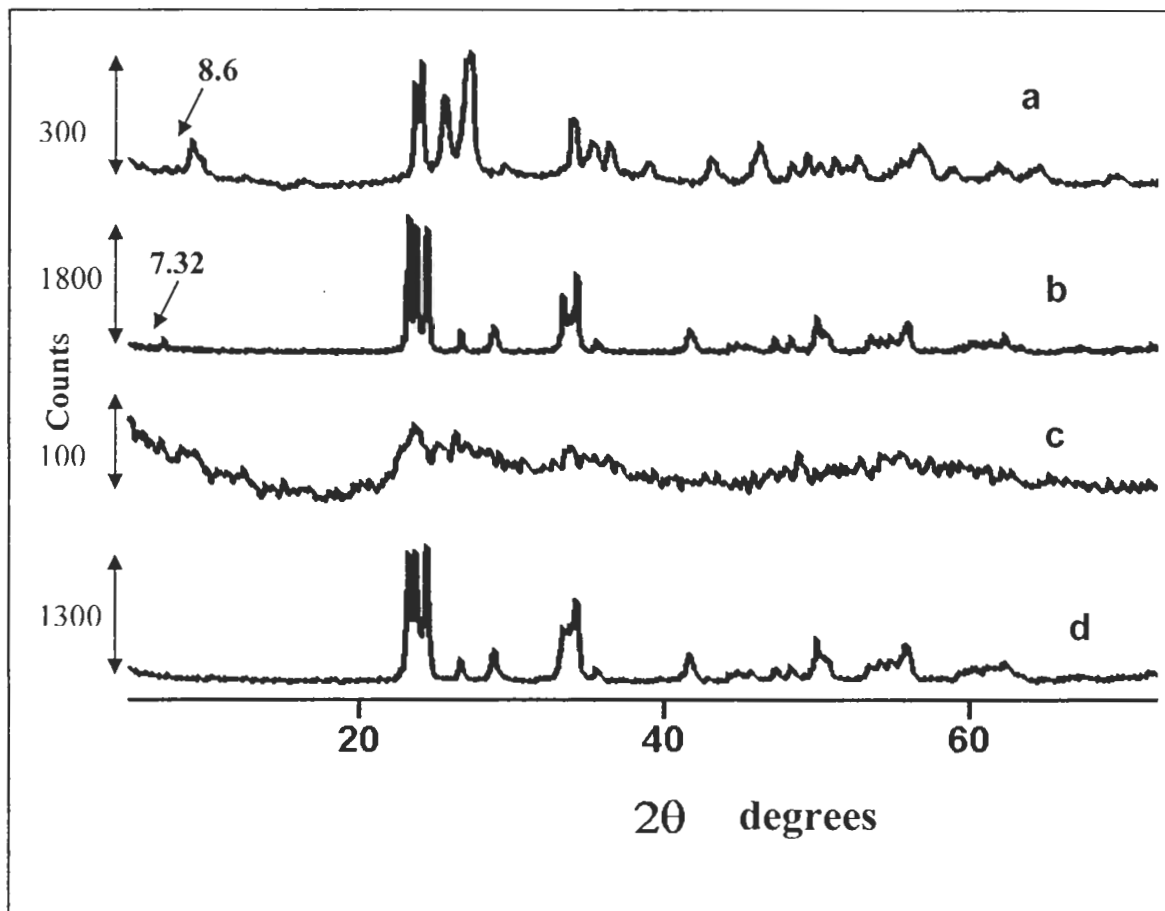


Figure 3.2. XRD spectra of uncalcinated and calcinated WO_3 (a.) Uncalcinated A1 sample, (b) A1 sampled after calcination at 500°C , (c) non-porous C sample before calcination and (d) non-porous sample after calcination at 500°C .

The XRD patterns for samples A1-A3 recorded prior to calcination are shown in Figure 3.3 and the corresponding patterns obtained for the same samples after calcination are shown in Figure 3.4. The XRD pattern for the uncalcined sample A2 shows similar patterns to A1 above 20° and different peak positions below 20°. For sample A3, a completely different pattern from either samples A1 or A3 emerges in which there a multitude of peaks is located across the entire region. All three samples show XRD peaks at low 2θ values which is indicative of a long range periodicity within the material. As found with sample A1, calcination of samples A2 and A3 lead to a change in the long range periodicity (peaks below 20° disappear or shift their 2θ positions) along with characteristic XRD peaks of a monoclinic WO₃. The positions of the main peaks for 2θ < 20° are listed in Table 3.2 along with their respective d spacing.

Table 3.2. XRD Low Angle Peaks

Sample	After Calcination	
	XRD 2θ	d spacing
A1	7.32°	12.1 Å
A2	13.2°	6.7 Å
A3	20.5°	4.3 Å
B1	2.7°	32 Å

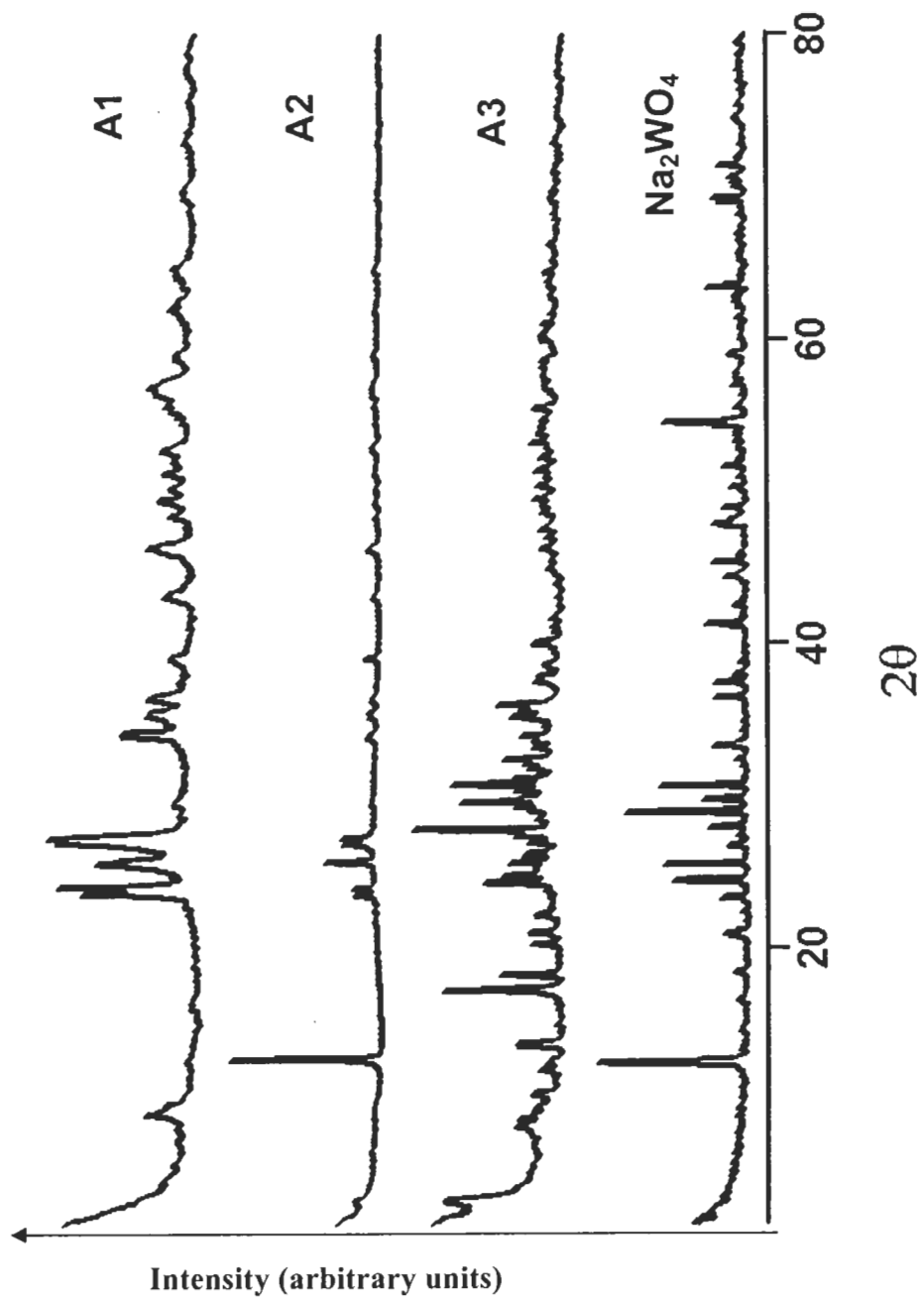


Figure 3.3. XRD spectra of WO_3 samples A1, A2 and A3 before calcination and Na_2WO_4

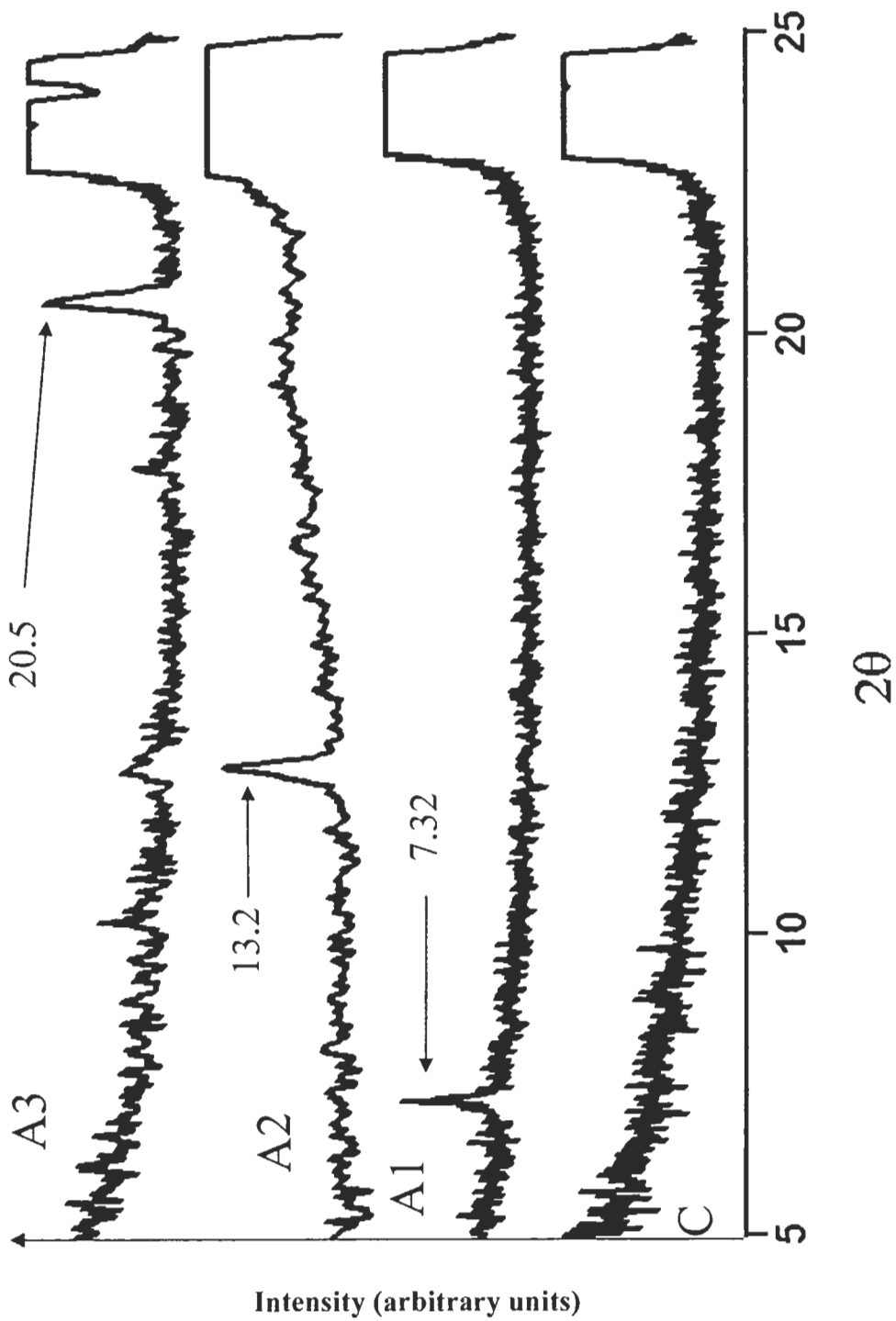


Figure 3.4. XRD patterns for various porous WO_3 samples after calcination at 500°C . The XRD pattern for non-porous WO_3 sample C is provided for comparison.

The absence of XRD peaks in sample C before calcination is expected and consistent with formation of hydrated amorphous tungsten oxide network. In sample A1, an amorphous tungsten oxide network would also form but in this case, the structure would exhibit long range periodicity arising from the surfactant templated architecture. The most likely explanation for the numerous peaks above 20° in the XRD patterns for samples A1-A3 is that they are due to CTAB polytungstate salts. Tungstate salts are known to produce numerous XRD peaks in this region (for example, see the XRD pattern of Na_2WO_4 in Figure 3.3.).

Evidence supporting a decomposition of the CTAB polytungstate salts after calcination is provided by the Raman spectra shown in Figure 3.5. Figure 3.5a and 3.5b are the spectra of sample A1 recorded prior to calcination and after calcination, respectively. The Raman peaks at 1004, 977 and 950 cm^{-1} in Figure 3.5a are not due to CTAB (see Figure 3.5c), hydrated WO_3 (see Figure 3.1c) or monoclinic WO_3 (Figure 3.1b) but rather are characteristic of tungstate ions.⁷¹ The broad bands located at 660 cm^{-1} and 226 cm^{-1} in Figure 3.5a is indicative of a highly hydrated polytungstate. The spectrum in Figure 3.5a shows that a polymerized tungsten oxide network forms that is negatively charged with CTAB cations as the counter ion. After calcination, this network is converted to monoclinic WO_3 , giving rise to a Raman spectrum with distinctive peaks at 807 and 718 cm^{-1} (Figure 3.5 b).

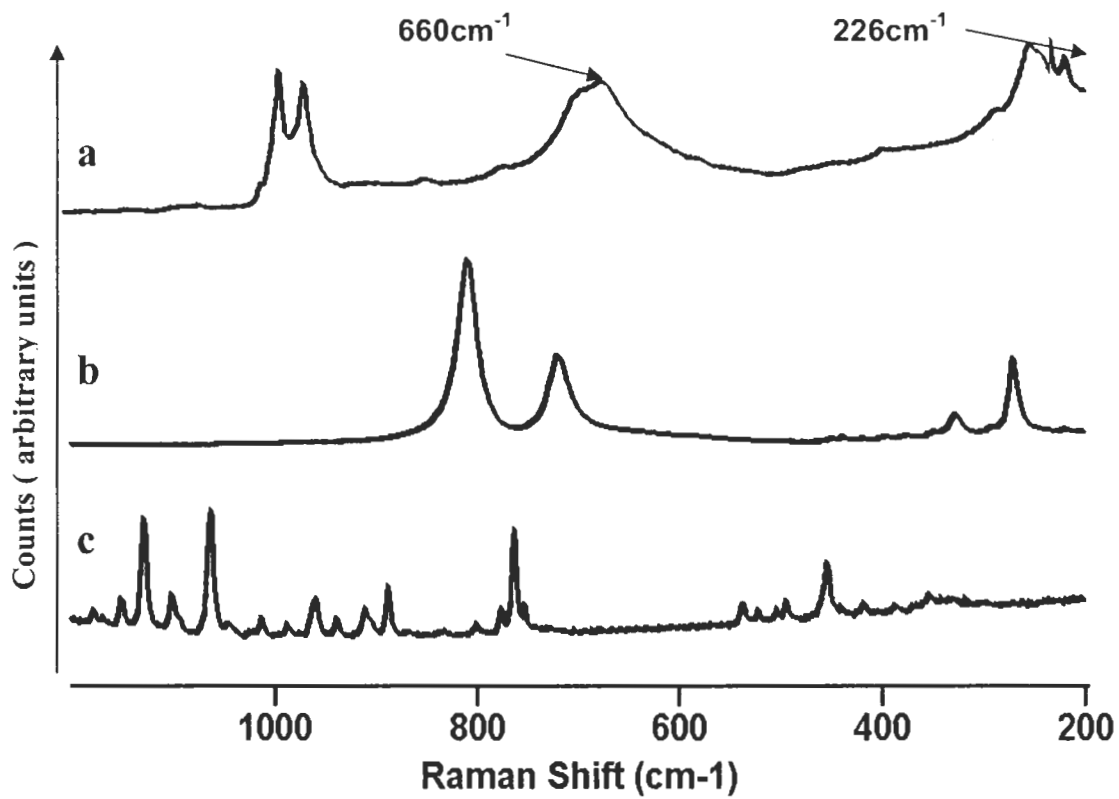


Figure 3.5. Raman spectra of sample A2 (a) before calcination and (b) after the calcination step. Curve (c) is the Raman spectrum of solid CTAB.

The Raman spectra of uncalcined samples A1-A3 are shown in Figure 3.6. The Raman spectrum of Na_2WO_4 is provided for comparative purposes. Thus, similar information was obtained from both XRD patterns and the Raman spectra for these samples. As with the XRD patterns, the Raman spectra for samples A1 and A2 are very similar and differ from the spectra obtained for A3. The bands due to a hydrated polytungstate are much weaker in the Raman spectrum of sample A3. At the higher CTAB/ H_2O loading in sample A3, there is less hydrated polytungstate and the spectrum is more like that of an ionic salt giving rise to Raman and XRD data closer to that of simple tungstate salts.

The XRD peak pattern for the precalcined sample B1 is shown in Figure 3.7 and the corresponding Raman spectrum is shown in Figure 3.6.d. The Raman spectrum shows that a tungstate salt similar to the sample A3 is formed. While the appearance of XRD peaks at low 2θ values provide evidence of a surfactant templated structure, it is noted that the XRD peak pattern for sample B1 is different from those obtained for samples A1-A3. This is expected given that a MCM-48 surfactant based recipe should lead to a cubic structure instead of a hexagonal array generated with MCM-41 based recipes.¹⁰⁶ However, it is found that the peaks obtained for the uncalcined sample B1 in the low 2θ region do not index to a body-centered cubic structure that is expected when using a MCM-48 templating recipes. On closer inspection of the literature, the assignment of MCM-48 to a body-centered cubic structure based on XRD data is debatable. Although it is generally accepted that MCM-48 produce body centered cubic structures indexed in the space group $\text{Ia}3\text{d}$ ¹⁰⁷, the XRD peaks in the original paper

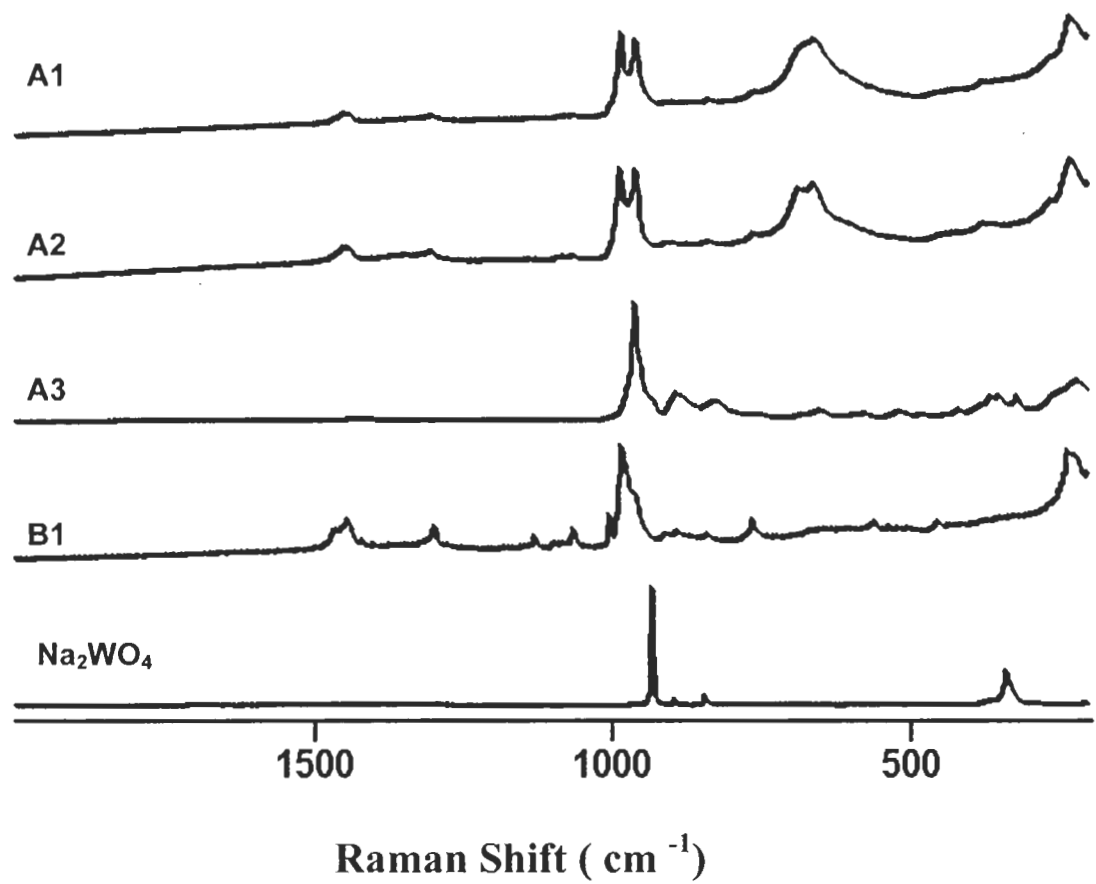


Figure 3.6. Raman spectra of uncalcinated and Na₂WO₄

describing the synthesis of MCM-48 materials¹⁰⁶ and those in subsequent articles¹⁰⁷ do not index to a body centered cubic structure. In the end, the structure of MCM-48 materials remains ill-defined.

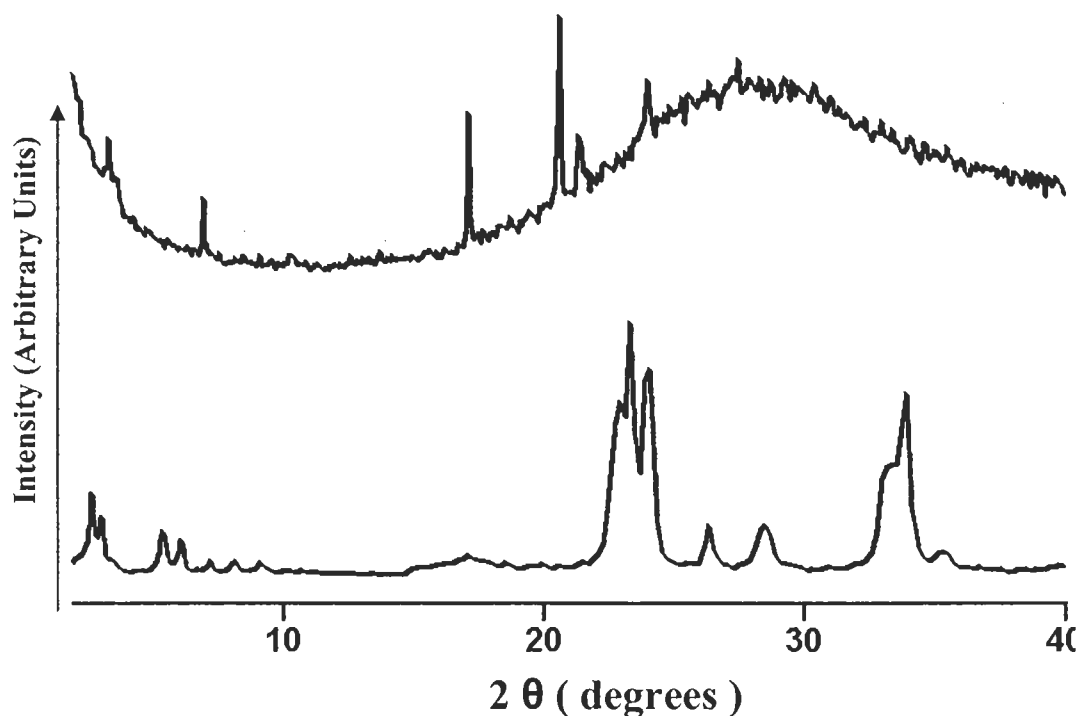


Figure 3.7. XRD spectra of WO₃ top curve showing B1 sample before calcination and bottom curve showing B1 sample after calcination at 500 °C.

After calcination of sample B1, all XRD peaks are removed and replaced by characteristic peaks of a monoclinic WO₃ along with a series of sharp peaks in the region below 20°. The sample labeled B2 also follows this trend producing a series of bands in the low 2θ region. Here we limit our discussion to sample B1 as the analysis of sample B2 will be discussed in section 3.3.6. As found for the A1-A3 samples, the severe calcination process resulting in the formation of monoclinic WO₃ lead to a collapse of the long range periodic structure in MCM-48 templated materials. While the calcination step

for both A and B samples lead to peaks at low 2θ values, samples A1- A3 are dominated by a single XRD peak in this region whereas the sample B1 gave rise to a series of peaks. For sample B1, the peak pattern below 20° is very similar to those reported for mesoporous MCM-48 silica¹⁰⁷, but again, the peaks do not index to a body-centered cubic structure.

3.3.3. TEM Micrographs

TEM micrographs are important because they provide a visualization of the templated structure. Figures 3.8 and 3.9 shows the micrographs of samples A1-A3 and B1, respectively. There are differences in the general features of samples A1-A3 compared to sample B1. Sample A1 clearly show a crystal habit whereas B1 appears as a noncrystalline spherical particle. A thin section of sample B1 shows a honeycomb type structure whereas it is not observed in samples A1-A3. Thin sections of both samples A1 and B1 also show long range periodicity with the appearance of parallel planes spaced at regular intervals. This ordered pattern explains the appearance of XRD peaks below 20° . The spacing between the parallel planes is approximately 12 Å and 28 Å for samples A1 and B1, respectively. A 12 Å and 28 Å d-spacing would produce XRD peaks at about 2θ values of 7° and 3° and this is consistent with the XRD peaks observed for these two samples. Sample A1 has a single XRD peak at 7.12° whereas sample B1 has two peaks at 2.72° and 3.09° . The second order peaks for sample B1 would be assigned to peaks at 5.42° and 6.14° and third order peaks are located at 8.16° and 9.13° . Other peaks located at 6.84° and 7.28° in sample B1 remain unassigned. Note that these parallel planes are not observed in the TEM micrographs of nonporous sample C (see Figure 3.10) and we recall the XRD pattern of sample C has no bands below 20° .

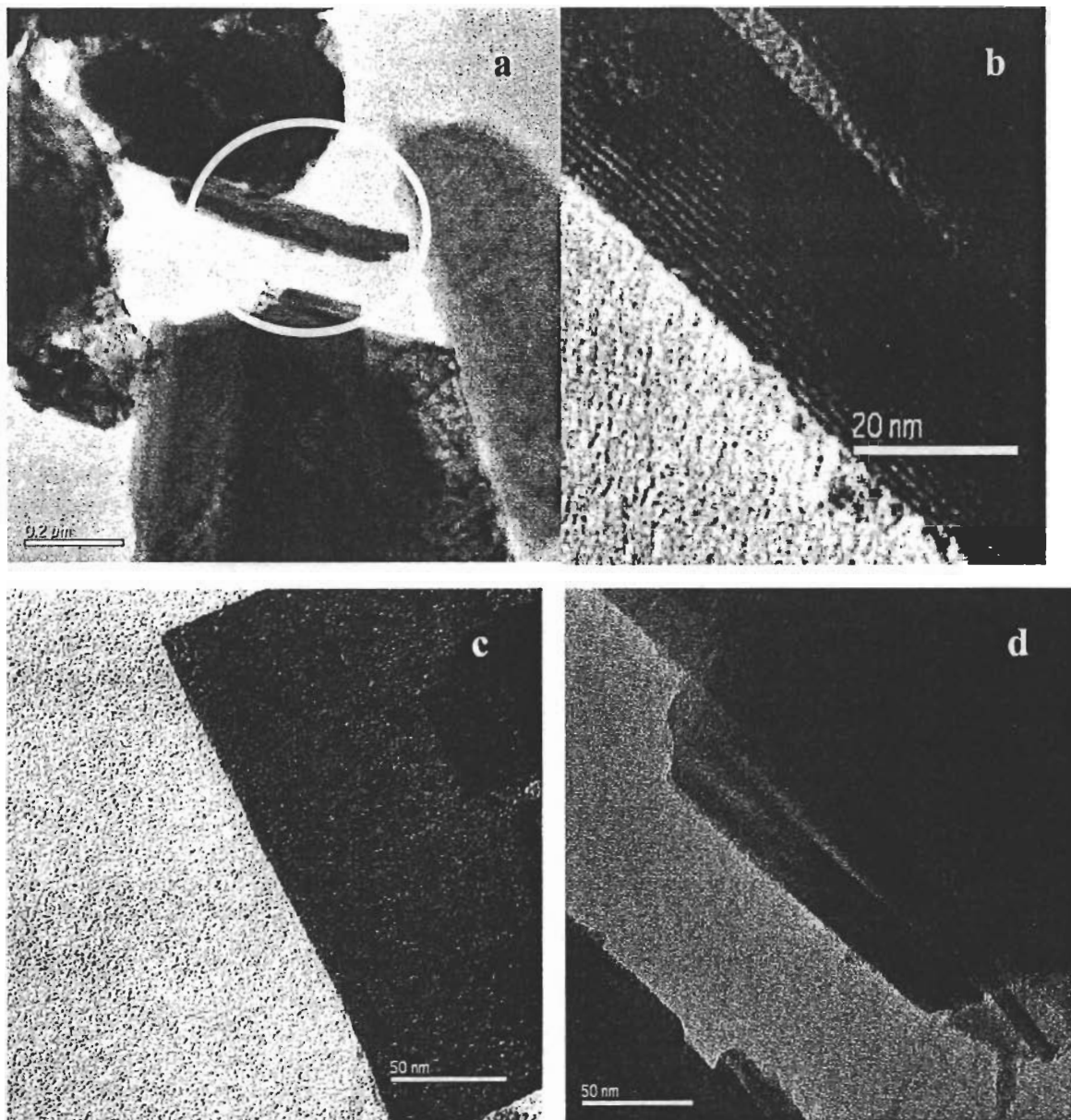


Figure 3.8. TEM micrograph of sample A1. Small part in circle in a is magnified in picture b. (a) A1 (b) A1 sample magnified (c) A2 sample (d) A3 sample

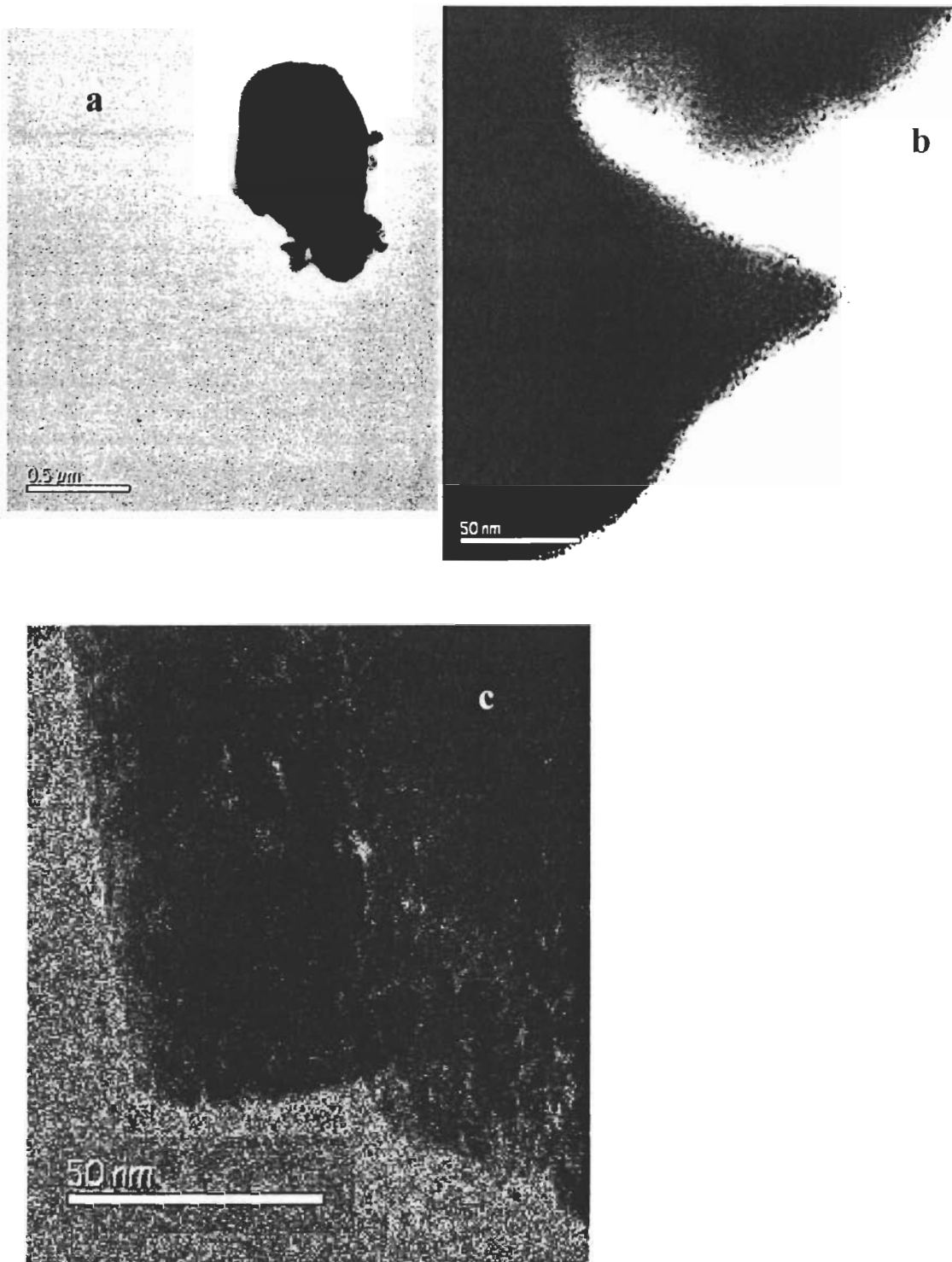


Figure 3.9. TEM micrograph of porous WO₃ samples (a) B1 sample, (b) picture shows sample B1 under higher magnification (c) B2 sample.

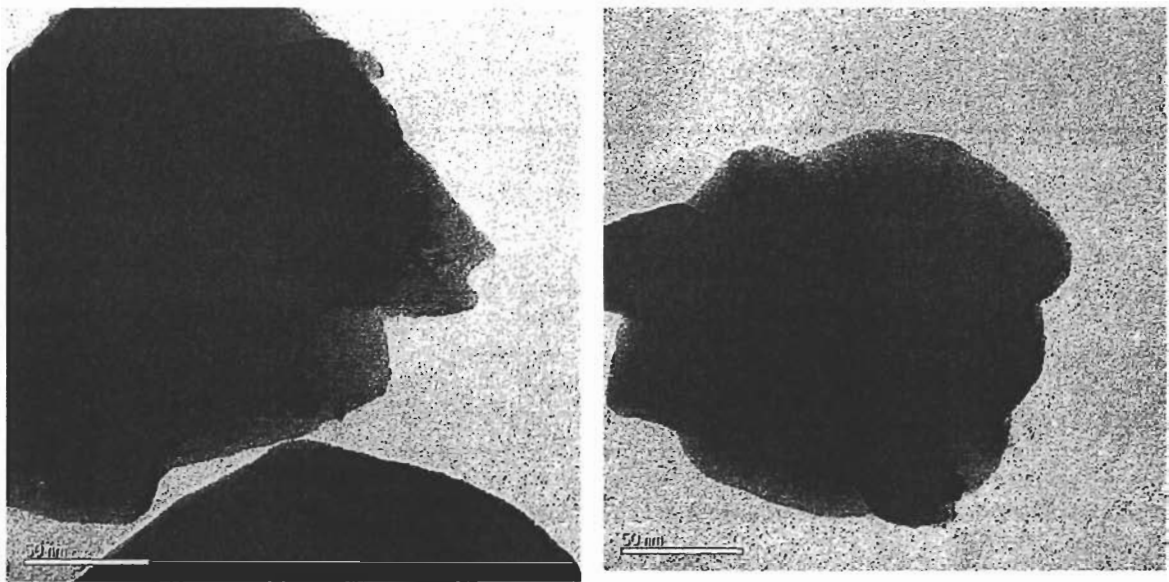


Figure 3.10. TEM micrograph of non-porous WO_3 sample.

A similar structure of parallel planes in the TEM micrographs of MCM-48 based mesoporous silica has been reported when viewed along the cubic [110] plane.¹⁰⁷ In this article, the spacing of the planes was approximately 30\AA and was used as an estimate of the pore size. It is tempting to assign the B1 structure to a cubic mesoporous material given that both the XRD pattern and TEM micrograph of sample B1 are similar to those reported for MCM-41 mesoporous silica.¹⁰⁷ However, it is unlikely that the WO_3 samples have retained a mesoporous structure because the conversion of the amorphous WO_3 material to a crystalline material results in the collapse of the surfactant template. This is in contrast to the preparation of mesoporous silica in which the calcination temperature usually does not exceed 400°C , the XRD pattern does not change drastically during calcination, and there is no transformation from an amorphous to crystalline state.¹⁰⁸ Given that we have generated a crystalline material, a plausible explanation for the appearance of parallel planes in the TEM micrographs of sample A1 and B1 is that it is simply due to formation of crystallographic shear planes¹⁰⁹

3.3.4. SEM Micrographs

From a materials standpoint, we find it interesting that the starting CTAB architecture is important in dictating the final material properties of the calcined product. The TEM micrographs and XRD show that the materials produced with MCM-41 based recipes differ from those starting with MCM-48 type recipes and this is consistent with the pictures of the SEM micrographs shown in Figures 3.11. Samples A1-A3 that are templated with MCM-41 based recipes lead to large platelet materials whereas sample B1 appears as micron-sized spherical particles.

The surface topology of sample A1-A3 are also quite different from B1. Sample A1 shows a highly “wrinkled” surface with many pores whereas the surface of sample B1 resembles interwoven tubular structures. The continuation of this entangled web of tubular structures into the internal volume could explain the honeycombed pictures obtained by TEM.

3.3.5. N₂ Adsorption Isotherms

From our perspective, the most interesting property of the surfactant templated WO₃ materials is that the calcined materials have relatively high surface area. The measured BET (N₂) surface areas are given in Table 3.3. For MCM-41 based samples (A1-A3) the surface areas are 98 to 120 m²/g whereas the surface areas MCM-48 based samples are slightly higher at 130-150 m²/g. These surface areas are substantially higher than the surface areas obtained for nonporous powders generated from emulsion based methods (about 40 m²/g) or those using chelating agents (about 20 m²/g).

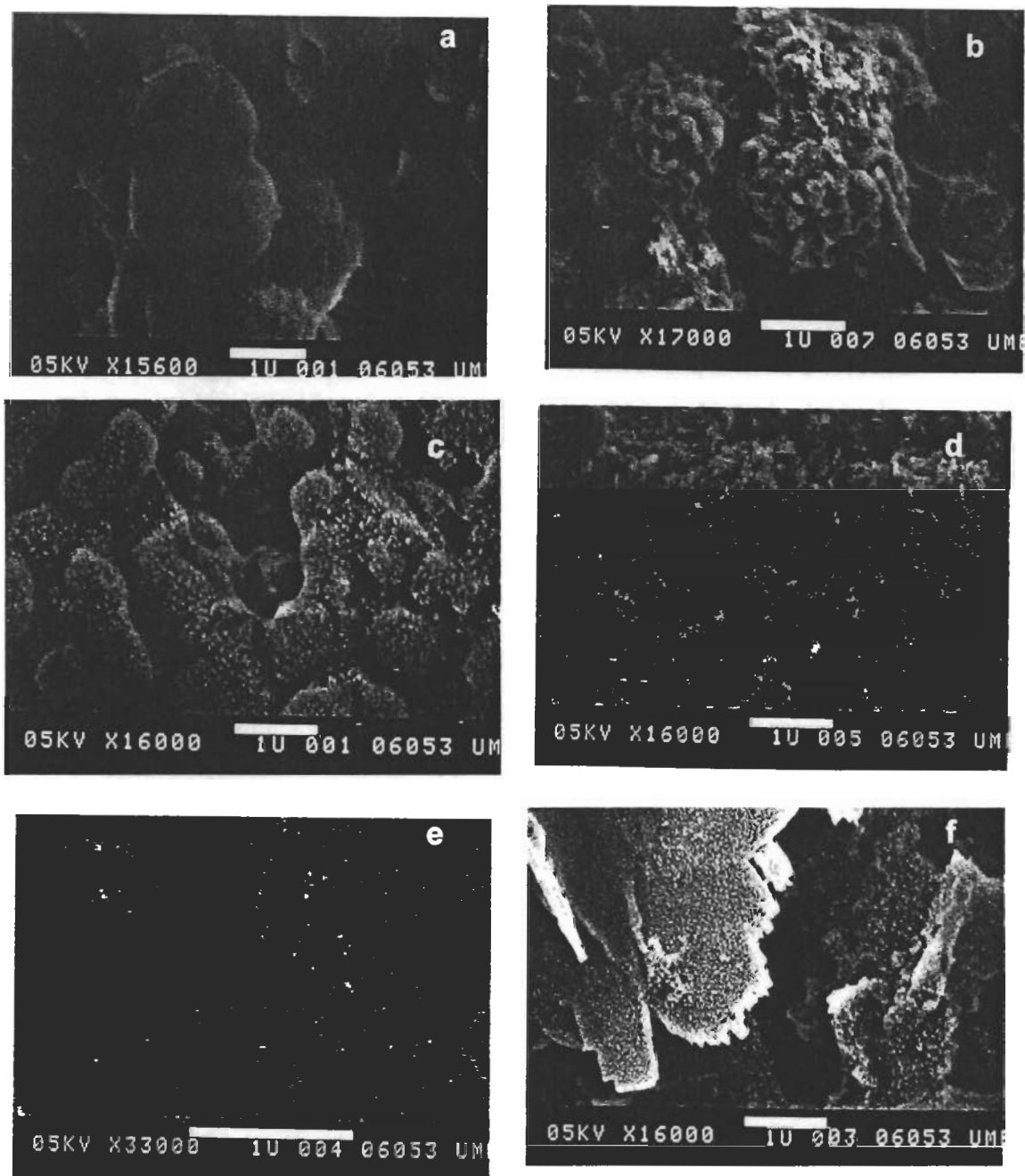


Figure 3.11. SEM picture of sample porous WO₃ (a and b) B1, (c) B2, (d) A1, (e) A2 and (f) A3.

Table 3.3. d-Spacing and Surface Area of Samples.

Sample	Type	XRD	d	Surface Area
		2 θ	Å	m ² /g
A1	MCM-41	7.32	12.0	120
A2	MCM-41	13.2	6.71	112
A3	MCM-41	20.6	4.31	98
B1	MCM-48	several	-	150
B2	MCM-48	several	-	130

Both chelating and emulsion based methods achieved a higher surface area powder by reducing the size of the WO₃ particles. For a spherical particle the surface to volume ratio is calculated as:

$$\frac{\text{Surface}}{\text{Volume}} = \frac{4.\pi.r^2}{\left(\frac{4}{3}\right)\pi.r^3} = \frac{3}{r} \quad (\text{Eqn 3.1})$$

Where r is the radius of the particle.

Surface areas are usually quoted in units of m²/g by including the density of the material:

$$\text{Surface Area}(S.A.) = \frac{3}{r \cdot \rho} \quad (\text{Eqn. 3.2})$$

where ρ is the density.

For the nonporous powders of 20 m²/g, the particle diameter calculated using equation 3.2 is about 40 nm. This calculated particle size is consistent with the diameter of these particles shown in the TEM micrograph (see Figure 3.10) and measured by SEM³². Based on the much higher surface areas obtained for samples A1-A3 and B1, smaller particles of diameters in the range of 5.5-7 nm would be predicted. However, the SEM pictures in Figure 3.11 of both A and B series powders show that the particles are several microns in diameter. The external surface area for a 2 μm particle would be 0.4 m²/g and therefore can not account for the measured areas of 98-150 m²/g.

It is noted that the above spherical model is an oversimplification as the SEM pictures clearly show that the external surface area of both A1-A3 and B1 particles are highly “wrinkled”. While this “wrinkling” effect would lead to an increase in the external surface area, it is unlikely that the highly wrinkled WO₃ surface would account for the factor of 300 times difference between a measured surface area of 150 m²/g and the surface area of a smooth micron sized nonporous particle of the same size. It is noted that roughening of the surface of nonporous silica particles is a common practice to increase surface area but this process only leads to a 30 to 50% increase in area.⁸³

The combination of high surface area and large particle size is indicative of a porous material. Nonporous fumed silicas have surface areas ranging from 50 m²/g to 380 m²/g whereas porous silica gels are much larger particles (> 1 μm in diameter) and have surface areas of 250 m²/g to 700 m²/g. Although at first glance the surface areas

obtained for WO_3 are not as impressive as those obtained for silica, one must remember that the density of the oxide enters into the surface area calculation. Thus a $150 \text{ m}^2/\text{g}$ surface area for WO_3 (density of $7.2 \text{ g}/\text{cm}^3$) would be equivalent to a silica (density of $2.2 \text{ g}/\text{cm}^3$) of $490 \text{ m}^2/\text{g}$. This is in the porous domain as nonporous silicas with surface areas near $500 \text{ m}^2/\text{g}$ are not available.

Additional evidence supporting the formation of a porous WO_3 is provided by the N_2 adsorption isotherm. Figure 3.12 shows the N_2 adsorption isotherm of samples A1, B1, B2 and C. While the nonporous WO_3 powders (sample C) exhibits a characteristic type II isotherm, the mesoporous samples A1, B1, and B2 are typical type IV isotherm with a characteristic sharp inflection due to capillary condensation inside a porous material. The P/P_0 location of the sharp step in the adsorption isotherm provides a measure of the pore size while the sharpness of the step is a measure of the pore distribution.¹⁰⁷ It is possible that the sharp inflection is due to adsorption on a heterogeneous surface containing both strong and weak adsorption sites. However, this is unlikely because infrared studies show that the adsorption behavior of water, pyridine and methanol are similar on samples A2, B1 and C.¹¹⁰

The appearance of a sharp step at the relative pressure range of $P/P_0 = 0.2-0.3$ is not associated with adsorption in micropores but rather with capillary condensation in a mesoporous material having pores greater than 20 \AA in size. Thus A1, B1 & B2 samples possess some level of mesoporosity. By inspection of the curves in Figure 3.12, sample B1 and B2 have have larger pores and a narrower pores size distribution than sample B1.

P/P_0

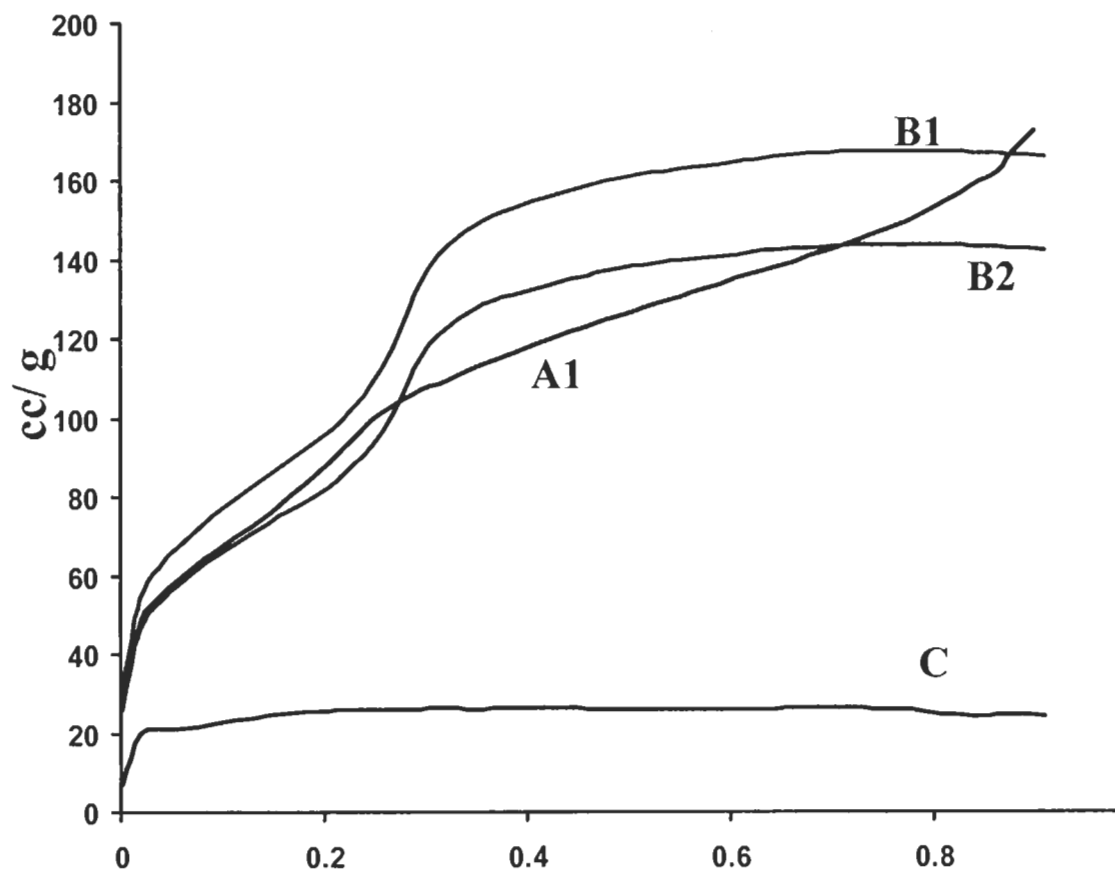


Figure 3.12. N₂ Adsorption Isotherms for porous samples B1, B2,A1 and a non porous C sample is shown as curve d for comparison

3.3.6. Porous WO₃ Generated using (NH₄)₂WO₄ as the Precursor

The synthesis of porous WO₃ required the initial step of passing the sodium tungstate through an ion exchange column. All our attempts at making mesoporous WO₃ by adding a solution of sodium tungstate directly to the CTAB solution failed in that it lead to mixtures of sodium tungstates and WO₃ with low surface area (< 1 m²/g). It is for this reason that nonionic surfactants³² and polymers⁹⁸ have been the main approach for synthesis of mesoporous WO₃. However, our results clearly show that the presence of ions such as CTAB cations can be used as templating agents in the sol-gel polymerization of monoclinic WO₃. The failure to get mesoporous WO₃ in the presence of metal cations may be due to crystalline and non-volatile nature of the tungstate salts.

It has been shown that a change in Na⁺ concentration during the precipitation of tungsten oxide dihydrate leads to considerable changes in morphology of the grains.¹¹¹ The Na⁺ form salts with tungstic acid during calcination, disrupting the formation of the long-range mesoporous architecture. This does not occur with CTAB because the tungstate salts formed with the CTAB cation are easily decomposed with heating to elevated temperature. We recall that the Raman spectra of all uncalcined samples showed that CTAB tungstate salts formed during the sol-gel process and that these decompose during calcination to form a monoclinic WO₃.

The success of using a CTAB cation in the synthesis of WO₃ lead us to attempt the synthesis of porous WO₃ using (NH₄)₂WO₄ as a substitute for Na₂WO₄. As found in the CTAB cation, the ammonium ion should also decompose with the calcination step and lead to the formation of a porous WO₃. In this case, the use of the ammonium

tungstate would have the advantage of eliminating the slow and tedious step of using an ion-exchange column.

The Raman, XRD and N₂ adsorption data of sample B2 showed that a mesoporous WO₃ material was produced using (NH₄)₂WO₄. The Raman spectrum (not shown) was identical to the spectrum shown in Figure 3.1a. This shows that the hydrated WO₃ was fully converted to a monoclinic WO₃. As with sample B1, the XRD pattern produced several peaks at low 2θ values along with peaks due to monoclinic WO₃. (see Figure 3.13)

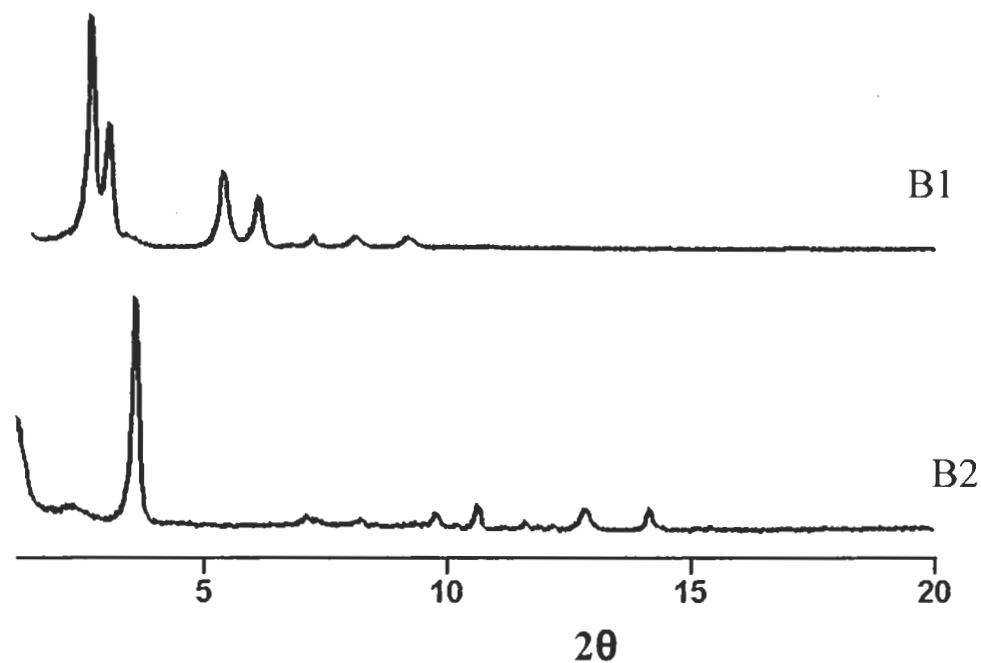


Figure 3.13. XRD of MCM-48 samples B1 and B2.

The N₂ adsorption isotherm of sample B2 was type IV and the surface area for B2 was 130 m²/g and this is slightly lower than the 150 m²/g obtained for sample B1(Figure

3.12). We attribute the slightly lower surface area to higher calcination temperature of 550 °C compared to 500 °C used with the Na₂WO₄ produced material. A 20-60% decrease in the surface area for non-porous WO₃ has been observed when calcination temperature is increased from 500 °C to 550 °C.³² While 500 °C is the preferred maximum calcination temperature, material produced using (NH₄)₂WO₄·2H₂O showed residual amounts of NH₄⁺ and hydrated WO₃ when calcinated at 500 °C. These were eliminated by increasing the temperature to 550 °C.

3.4. Summary

We report here the synthesis of porous monoclinic WO₃ using cationic surfactant based recipes as templating molecule. Though the synthesis of WO₃ films and powders have been reported using nonionic surfactants, our work shows that unique materials can be produced using cationic surfactant based recipes. Both MCM-41 and MCM-48 type synthetic methods were used in preparation of porous WO₃ using CTAB as the templating molecule and Na₂WO₄ or NH₄WO₄ as the precursor. When using Na₂WO₄ as a precursor, it is important to remove Na⁺ ions during the synthesis as this leads to sodium tungstates, which disrupts the formation of the mesoporous oxide. However mesoporous WO₃ is produced when metal cations are removed by ion exchange or replaced with combustible cations (CTAB, NH₄⁺). Removal of Na⁺ is accomplished by first passing the Na₂WO₄ through an ion exchange column. The use of (NH₄)₂WO₄ has an advantage in that no ion exchange column is needed. The NH₄⁺ cations are easily removed during the calcination step but this requires a slightly higher temperature which leads to a slight reduction in the surface area.

Chapter 4

SIZE SELECTIVE DETECTION IN POROUS WO₃ BASED SENSORS

4.1. Introduction

As discussed in Chapter 1, the development of new approaches that would lead to a reduction in the number of “false alarms” is a critical requirement for SMO sensor technology. Given the success in fabricating porous WO₃, the next step was to investigate the usefulness of these materials in improving detection selectivity in a working sensor. Detection selectivity is anticipated because the access and adsorption of a gas molecule in the interior pore structure of the porous WO₃ would be size dependent leading to a size dependent magnitude change in conductivity of the SMO sensor. In essence, use of the porous WO₃ incorporates a filtering approach directly into the sensor element itself. It is noted that the powder based sensors have been shown to be equal in sensitivity with thin film based sensors. Therefore any improvement in selectivity obtained by using the porous WO₃ powder sensors would occur without a sacrifice in sensitivity.

Work at LASST has centered on nerve agent detection and the structures of two agents are shown in Figure 4.1. For obvious safety reasons, research on nerve agent detection in academia is accomplished with benign analogues. The choice of the simulant depends on the particular nerve agent characteristic to be mimicked, and by far, the most common molecule used as a simulant is DMMP. The structure of DMMP is shown in Figure 4.1.

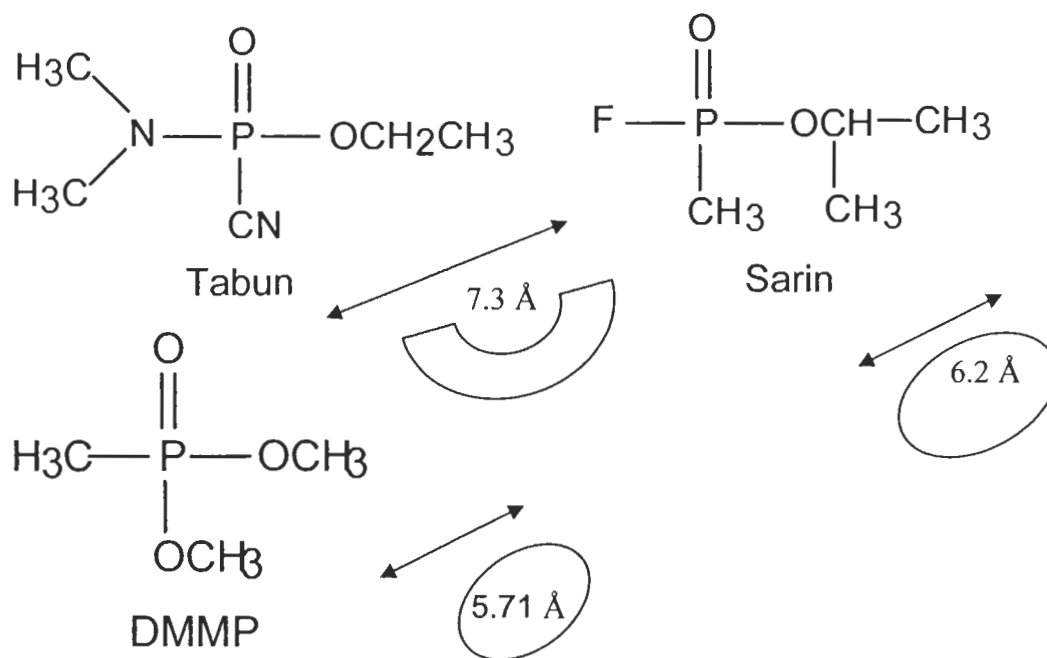
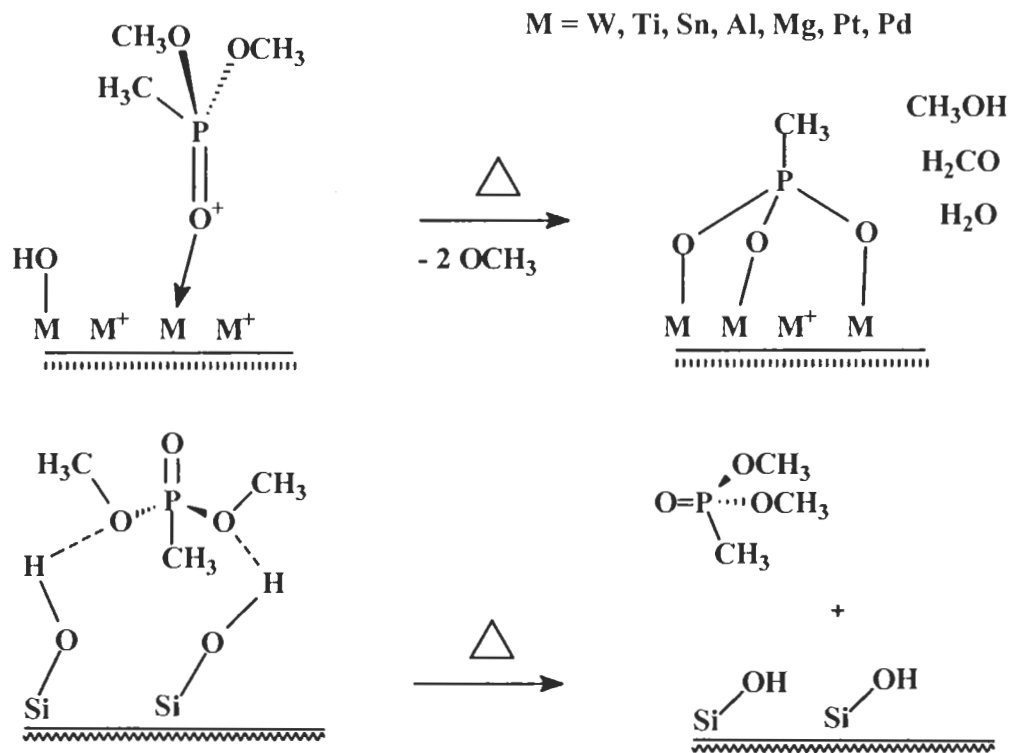


Figure 4.1. The Structures of Nerve Agents, Tabun, Sarin and Simulant DMMP showing their relative size and shapes.

There have been numerous infrared studies on the adsorption of DMMP on oxide surfaces and the general findings are described by the reaction equations shown in Figure 4.2. On most oxides such as Al_2O_3 ,¹¹²⁻¹¹⁵ TiO_2 ,^{31,114,116,117} WO_3 ,^{31,114} La_2O_3 ,¹¹⁵ MgO ,^{114,115,118-121} Fe_2O_3 ,^{115,122-124} and Ag_2O ,¹²⁵ DMMP adsorbs through the P=O functionality and decomposes via elimination of the methoxy groups at elevated temperatures producing a stable methyl phosphonate (phosphate in the case of Fe_2O_3) on the surface. This is in contrast to the adsorption behavior on silica, where DMMP adsorbs via a hydrogen bond between the methoxy moieties and the surface SiOH groups with subsequent evacuation at elevated temperature resulting in the complete desorption of intact DMMP molecules from the surface.¹⁷

Reaction on other oxides



Reaction on Silica

Figure 4.2. Reaction equations of DMMP at elevated temperature on various metal oxides

The decomposition of DMMP on WO_3 liberates methanol in the process, and it is the subsequent oxidation of methanol to formaldehyde that leads to a change in conductivity.¹¹⁸ Since the mechanism of signal generation for DMMP and methanol are the same, (i.e., oxidation of methanol) developing a method that can distinguish between DMMP and methanol has been a critical goal and benchmark for demonstrating detection selectivity for toxic nerve agents by this technology.

4.2. Experimental

Development of the sensor platform is a major task in itself which lies outside the scope of this thesis. Dr. Lad's group at LASST has been at the forefront of sensor platform research and their platforms have been used with our WO_3 powders.¹²⁷ In brief, Sensor platforms were prepared using photolithographic lift-off techniques. The sensor platform, a 6 mm square device, is composed of an interdigitated electrode pattern composed of 300 nm of platinum on 20 nm of zirconium as an adhesion layer. The substrate is R-cut sapphire. The reverse side contains a serpentine heater and a resistance temperature device (RTD) of the same material as the electrode. To produce the sensor, photoresist was spun on a clean 3 inch sapphire wafer. After a soft bake at 115 °C, the electrode pattern was produced using an ultraviolet mask aligner. After development, the wafer was hard baked at 115 °C and placed in an ultra high vacuum chamber for metal deposition. Zirconium and platinum were deposited using electron beam evaporation.¹²⁸ Subsequently, the wafer was placed in a photoresist stripper to remove the excess metal. The heater/RTD side of the wafer was then processed identically. After removal of the

excess metal, the wafer was rinsed in solvents and deionised water, then placed in a furnace at 500 °C to stabilize the platinum. Before introduction of the powders, the wafer was diced into individual sensors.

A suspension of WO₃ powders (25 mg) in 1 mL of deionised water was prepared and sonicated for 30 minutes. A drop of the suspension was placed on the sensor platform to cover the electrodes and dried in a nitrogen environment. WO₃ powder films produced with this simple deposition procedure were remarkably robust and stable, routinely generating sensor data over months of operation at temperatures above 300 °C. Furthermore, the powder based sensors showed good sample-to-sample reproducibility as the response signal was insensitive to variations in powder film thickness. Above a minimum threshold thickness, the rapidity and magnitude of the sensors response to target gas pulse showed little, if any, thickness dependence. Both the nano-sized nonporous and porous powder sensor show very fast response to a gas pulse because the migration of bulk lattice oxygen to the surface is dictated by particle size (or wall thickness in porous materials) and not the thickness of the powder layer deposited on the sensor platform. Below a minimum thickness the devices usually failed because the films were not contiguous with large cracks appearing leading to an equivalent electrical open circuit.

The RTD of each sensor was then calibrated in an oven at various temperatures up to 400 °C. The response of the film was measured at the same time. After RTD calibration, the sensor platform was bonded into a standard header. The sensors were then placed in a test chamber and heated using a Watlow temperature controller. Temperatures ranged from room temperature to 400 °C. Several samples were also

prepared by calibrating the RTD prior to the WO_3 powder films being placed on the electrodes. Therefore, these devices were not heated prior to introduction into the test chamber.

Once bonded into a header package, the sensors were placed in a stainless steel test chamber in a chemical fume hood. A picture of the test chamber is shown in Figure 4.3. A principle advantage of this test chamber is that up to four sensors can be tested simultaneously to the same gas pulse. The entire test system is composed of eight Tylan General mass flow controllers, each mixed and plumbed into one inlet for the test chamber. The ability to perform simultaneous measurements on more than one sensor element is a critical element of the work described in this chapter as the selectivity is derived from normalizing the sensor response obtained from the mesoporous WO_3 sensors to the same response obtained for a nonporous WO_3 sensor.

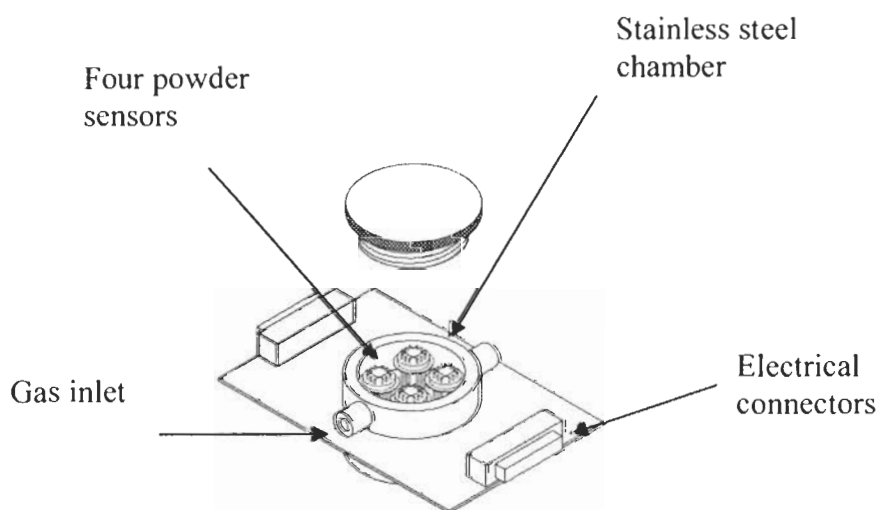


Figure 4.3. Sensor testing device

A test protocol program written in C+ controls each mass flow controller.¹²⁹ The same program also records the resistance of each sensor by cycling through the four sensors in the test chamber starting with sensor 1. Data is collected by a HP 34970A Data Acquisition System. The operating temperature was fixed at 360 C and target gas flow rate was 100 sccm. The test protocol consists of first flowing air with all hydrocarbons removed, zero air, for 20 minutes to establish a baseline. Second, the target gas is switched on for five minutes, followed by a two-minute purge of the target gas line. Third, the system flows zero air over the sensors for either 20 minutes or 40 minutes to again establish a baseline. For this experiment, only one target gas line was used.

Following exposure to the selected target gas, the input line was switched to a new target gas. The target gas methanol was supplied at a pressure of 30 psig. However, for the other targets, a bottle of gas was not prepared. In this case, following exposure to methanol, the input line was placed in a bottle containing the alcohol and left above the liquid level. The bottle was then sealed with the gas line inside.

After stabilization of the film, the sensors were tested against a series of random pulses of the five alcohols and DMMP with a minimum of three separate pulses per alcohol (at least 15 random alcohol pulses in total). The alcohol pulses were performed before DMMP because the alcohols do not poison the sensor enabling repeated measurements. The last gas pulse was reserved for DMMP as this led to poisoning of the sensor, and thus ending its usefulness for further testing.

Prior to performing sensor testing with random alcohol sequences, a series of measurements using sample A2 and sample C coated sensors were performed to examine device-to-device reproducibility. On four separate occasions, new sensor platforms were

coated with sample A2 and C powders and the response of these sensors measured to pulses of methanol and DMMP. The device-to-device reproducibility was high and data from these measurements are included in the calculation of error bars (95% confidence level) in Figure 4.7.

The shape and size for the structures for Figure 4.4 and 4.5 were obtained from Hyperchem program.

4.3. Results and Discussion

The space filling models of DMMP and methanol depicted in Figure 4.4 show that the largest diameter of DMMP is about 5.71 Å and for methanol it is 2.8 Å in diameter.

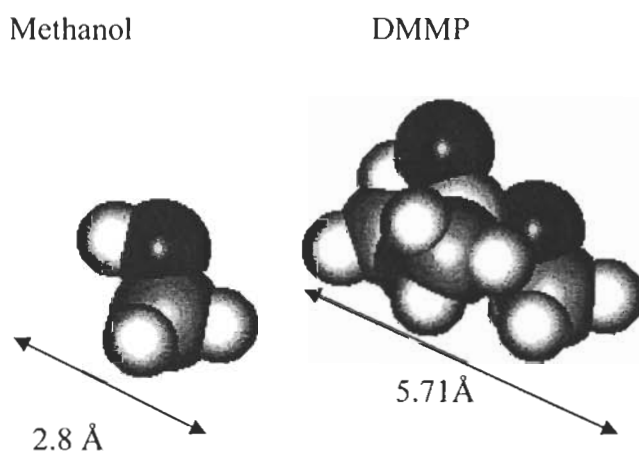


Figure 4.4. Methanol and DMMP space filling models and their sizes

Thus, obtaining size selectivity in detection between methanol and DMMP, would require a microporous material with pores larger than 2.8 Å and less than 5.71 Å. By definition mesoporous material has pore sizes greater than 20 Å and these larger pores would not be expected to get exhibit size selectivity between adsorbed methanol and DMMP.

At first glance, the use of a porous WO_3 samples with pore sizes between 3-5.5 Å will operate as a selective sensor for methanol rather than the target DMMP or the even larger sized nerve agents. This is in an opposite direction to our goal. The intent is to detect the larger DMMP or nerve agents whereas methanol is an interferent giving rise to false alarms. While methanol would adsorb inside 3- 5.5 Å pores, the larger DMMP (5.71 Å diameter) would be excluded from the inner pore area and this exclusion would be more severe for the even larger nerve agents. The solution to this problem is to operate the sensor in a difference detection mode where the response of a target molecule on the porous WO_3 is compared to a second sensor containing the nonporous WO_3 powder.

On the nonporous WO_3 sensor, there should be minimal, if any size dependence in the availability of surface sites to the target gas. In contrast, a molecule too big to enter a pore will result in a lower adsorbed amount on the porous based sensor, leading to a lower change in resistance relative to the same signal measured on the reference, nonporous WO_3 sensor. Hence, the lower the change in resistance, the larger the difference when exposed to the reference sensor.

4.3.1. Adsorption of Methanol and DMMP

In chapter 3 we clearly showed that porous WO_3 materials were fabricated. However, the exact nature of the pore size distribution is currently not known. While the

N_2 adsorption isotherm for these material show a sharp rise in P/P_0 at 0.2-0.3 nm characteristic of mesopores, determination of the microporosity (if any) requires analysis of the adsorption isotherm in the $P/P_0 < 10^{-3}$ region. This low pressure range is below the operational range of our Gemini instrument. Although we now have IR data suggesting that there is a size dependant adsorption occurring on the porous powders, our initial choice to perform powder based sensor tests using sample A2 and A3 material is in hindsight, fortuitous and were based solely on the fact that these materials showed large differences in sensor response to methanol and DMMP.

To fully explore a possible size dependence in selectivity, we have performed experimental measurements not only with the two test molecules of methanol and DMMP, but also with a series of alcohols of different shapes and sizes. The additional alcohols used were ethanol, isopropanol, t-butanol and 2-hexanol and their structures and relative size are shown in Figure 4.5.

Figure 4.6 shows a typical sensor response curve to three consecutive gas pulses of methanol, t-butanol and DMMP. The upper curve is the data obtained from the porous A2 sample and the lower curve is the response obtained from the nonporous C sample WO_3 sensor. The curves are on the same ordinate scale and are offset for clarity.

It is noted that the gas pulses were done without strict controls on the dosing protocol. The carrier gas was simply passed over a vial containing the alcohol for a period of about 2 minutes. This means that each pulse was ill-defined with no control in concentration and mixing with the carrier gas. While this would account for pulse-to-pulse differences in the magnitude and shape of the sensor response on the same detector, it is noted that the shape including the fine features of the response on each sensor for the

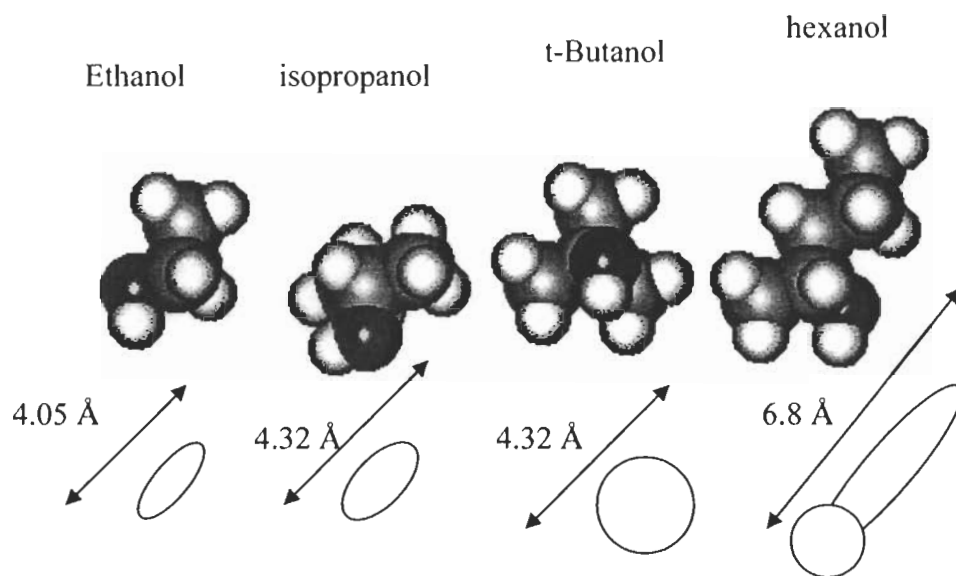


Figure 4.5. Space filling models of various alcohols showing relative size and shapes

same pulse was very similar. This is not surprising as both sensors are in contact with the same ill-defined gas pulse at the same time. While the initial slope of the change in resistance was rapid for both mesoporous and nonporous sensors, the slope was always steeper on the nonporous oxide and this is perhaps indicative of a slower diffusion of the gas in the porous oxide. However, the variation in the initial slope showed large pulse-to-pulse variations in value for repeated measurement to the same target gas. Therefore, no trend was discernable from the initial slopes for different gases. Given the ill-defined nature of the gas pulse, the result is consistent with recent work by Frederick *et.al.*¹²⁹ that showed the pulse-to-pulse variation in the initial sensor response is controlled by the gas delivery system.

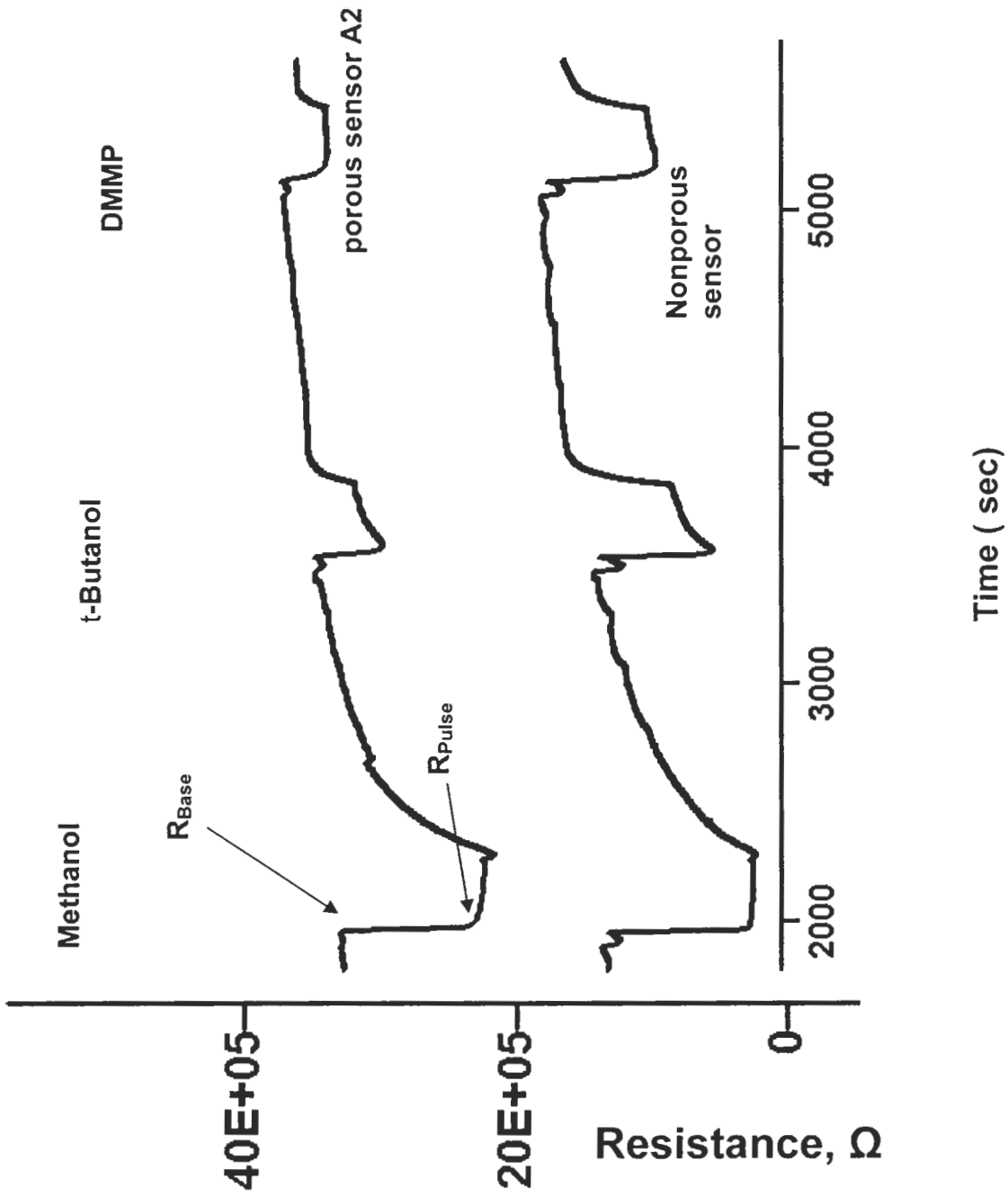


Figure 4.6. Typical 3 pulse sequence of methanol, t-butanol and DMMP

By far, the biggest difference in sensor response for these sensors to a given gas pulse was the relative change in magnitude in resistance. While the magnitude of the resistance change for methanol is about the same on both sensors in Figure 4.6, the magnitude of the response is clearly lower for both t-butanol and DMMP on the mesoporous sensor relative to the nonporous material. For each pulse, we calculated the change in conductivity (ΔC) with equation 4.1:

$$\Delta C = \frac{1}{R_{Pulse}} - \frac{1}{R_{Base}} \quad (\text{Eqn. 4.1})$$

where R_{Pulse} is the resistance measured in the plateau region of the pulse and R_{Base} is the based resistance measured just prior to the gas pulse. An example of the selection points for R_{Base} and R_{Pulse} are indicated for the methanol pulse in Figure 4.6.

The value of ΔC is proportional to the number of carriers generated in the WO_3 which is related to kinetics of the redox reaction of the surface with the gaseous molecule. The ΔC obtained on each mesoporous WO_3 sensor is then ratioed to the corresponding ΔC obtained on the nonporous WO_3 sensor ($\Delta C_{porous} / \Delta C_{nonporous}$). A plot of this ratio versus volume of the molecule is given in Figure 4.7 and these curves clearly point to a selective detection method for methanol from DMMP. The error bars in Figure 4.8 represent the 95 % confidence level.

It is possible that the difference in $\Delta C_{porous} / \Delta C_{nonporous}$ arises from different reaction chemistry on the nonporous and porous materials. This would alter the kinetics of the surface reduction and hence change the number of charge carriers under steady state conditions. However, our infrared data suggests that there is very little difference in the adsorption behavior of the various alcohols on sample A2 or the nonporous sample C. Figure 4.8 shows the FTIR spectra of sample A2 and sample C. Of particular note is the

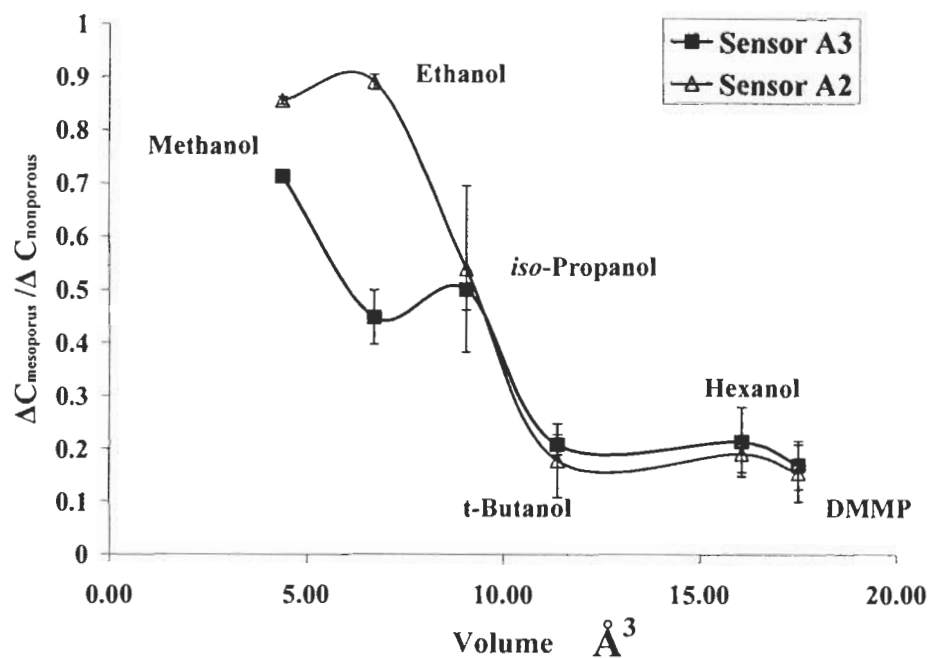


Figure 4.7. $\Delta C_{\text{porous}} / \Delta C_{\text{nonporous}}$ value as a function of size of the molecule

similarity in the intensity ratio of the two bands at 1394 cm^{-1} and 1124 cm^{-1} on both materials which indicates the same relative amount of undissociated and dissociative adsorption on both materials. The band at 1394 cm^{-1} is the O-H bending mode of molecularly adsorbed water and the band at 1124 cm^{-1} is the O-C structure mode of adsorbed CH_3 group on the surface.¹²⁹

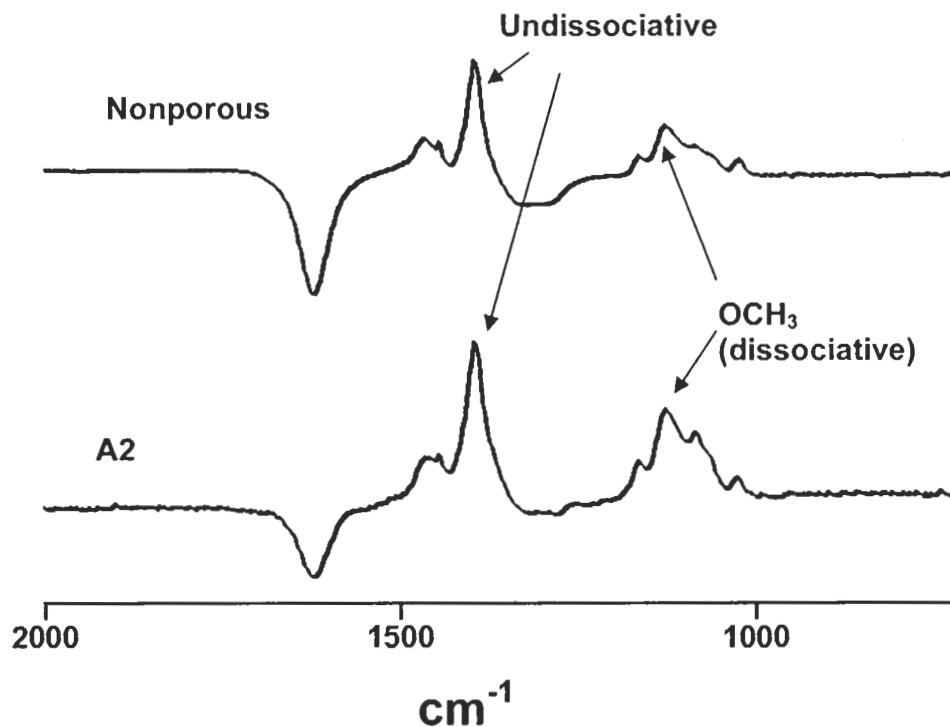


Figure 4.8. FTIR of Methanol on porous and nonporous tungsten oxide.

This similarity in the IR spectra of methanol on the sample A2 and A3 is also observed for other alcohols and DMMP used in this study. However, we note that changes in the conductivity can arise from minute changes in the surface kinetics. Thus the IR data does not eliminate the possibility that the difference in sensor response is due to differences in reaction kinetics arising from subtle differences in surface chemistry.

4.3.2. Adsorption of a Series of Alcohols

On the other hand, the IR data does support a size selectivity explanation for the detection selectivity. In a series of thin film infrared experiments, samples A2, A3 and C were evacuated at room temperature and exposed to the saturation vapor pressure of various alcohols. Typical spectra obtained on the nonporous WO_3 are shown in Figure 4.9. Each alcohol produces unique bands that could be used to measure the relative

adsorbed amount of each alcohol on all three powders. For each alcohol, the value obtained for the integrated intensity of a C-H bending mode was first normalized by the value obtained for the intensity of the WO_3 bulk mode. This value gives the relative adsorbed amount of the alcohol per gram of WO_3 probed by the IR beam.

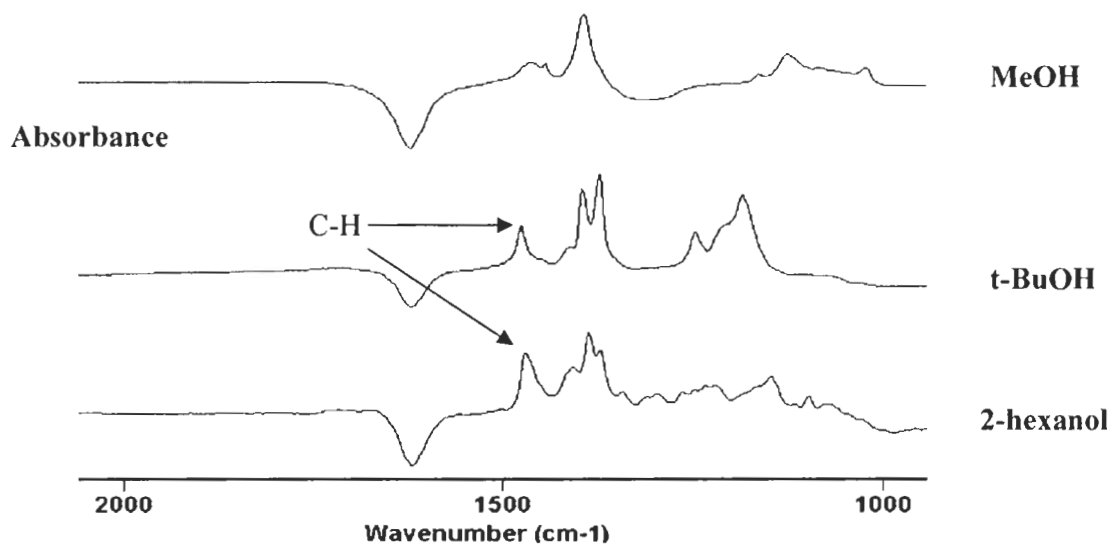


Figure 4.9. Typical FTIR spectrum of various alcohols adsorbed on WO_3

For a given alcohol, we then compute a second ratio in which the above values for the adsorbed amount per gram of WO_3 on the porous sample is normalized by the same value obtained on the nonporous oxide. A plot of this normalized value as a function of the size of the alcohol is shown in Figure 4.10. The trend obtained from the infrared measurements clearly show the strong correlation between the relative amount of adsorbed alcohol and the $\Delta C_{\text{porous}} / \Delta C_{\text{nonporous}}$ values plotted in Figure 4.7.

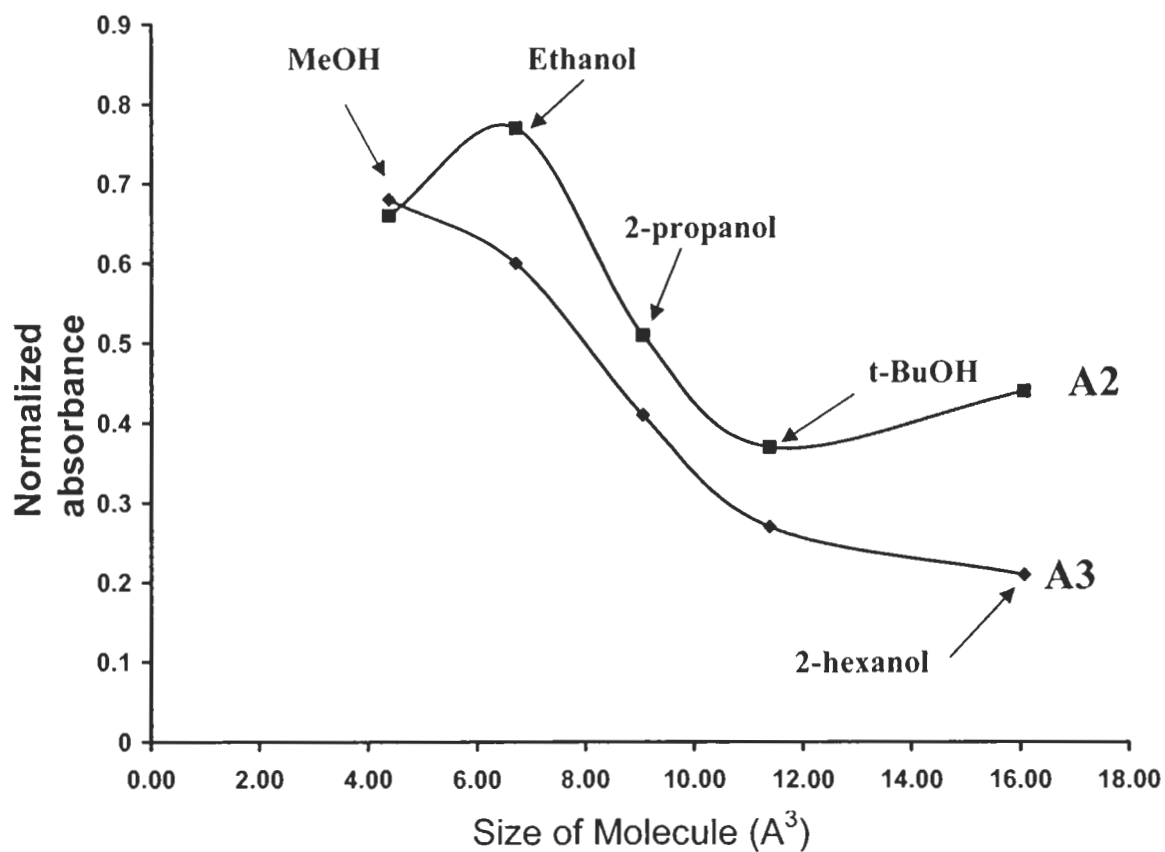


Figure 4.10. Relative adsorbed amount of various alcohols on WO_3 samples A2 and A3 as determined by IR spectroscopy.

We recall that, our initial intent was to develop a strategy for distinguishing between methanol and DMMP in SMO detection. This is clearly demonstrated as the $\Delta C_{\text{porous}} / \Delta C_{\text{nonporous}}$ for methanol is about 0.8 and for DMMP this value is 0.2 for both porous materials. This is a factor 4 of a difference in magnitude and this same factor is obtained when comparing methanol to t-butanol. Similarly, the IR also shows a large difference in adsorbed amounts of methanol relative to t-butanol. The adsorbed amount ratio for t-butanol is a factor of 2.5 times lower than the value obtained from methanol. Given the large difference in both adsorbed amount and $\Delta C_{\text{porous}} / \Delta C_{\text{nonporous}}$ measurements as a function of size of the alcohol. We conclude that with a narrow pore size distribution we expect a sharp reduction in $\Delta C_{\text{porous}} / \Delta C_{\text{nonporous}}$ values with molecules too large to fit in the pores if the difference arises from the microporosity of the WO_3 material. The fact that a sharp size selectivity is not observed could be due to a combination of a wide pore size distribution coupled with a size independent contribution from adsorption on the highly “wrinkled” external surface.

Perhaps more interesting is that the results point to a strategy for developing a very narrow “Notch” detection system. For example, the data in Figure 4.7 show that by comparing the response from two closely related porous powders, we have a system that can detect ethanol. This is shown in Figure 4.11. A possible explanation for this effect is that a slight difference in the pore size distribution between the two porous materials enhances the capillary condensation of ethanol over methanol. This produces a higher relative adsorbed amount of ethanol leading to highly selective “Notch” detector. In principle, this concept could be applied to any size molecule. In the case of DMMP, we

predict that two porous materials with average pore size distribution near 5.7 Å and different pore size distribution would lead to a DMMP notch detector.

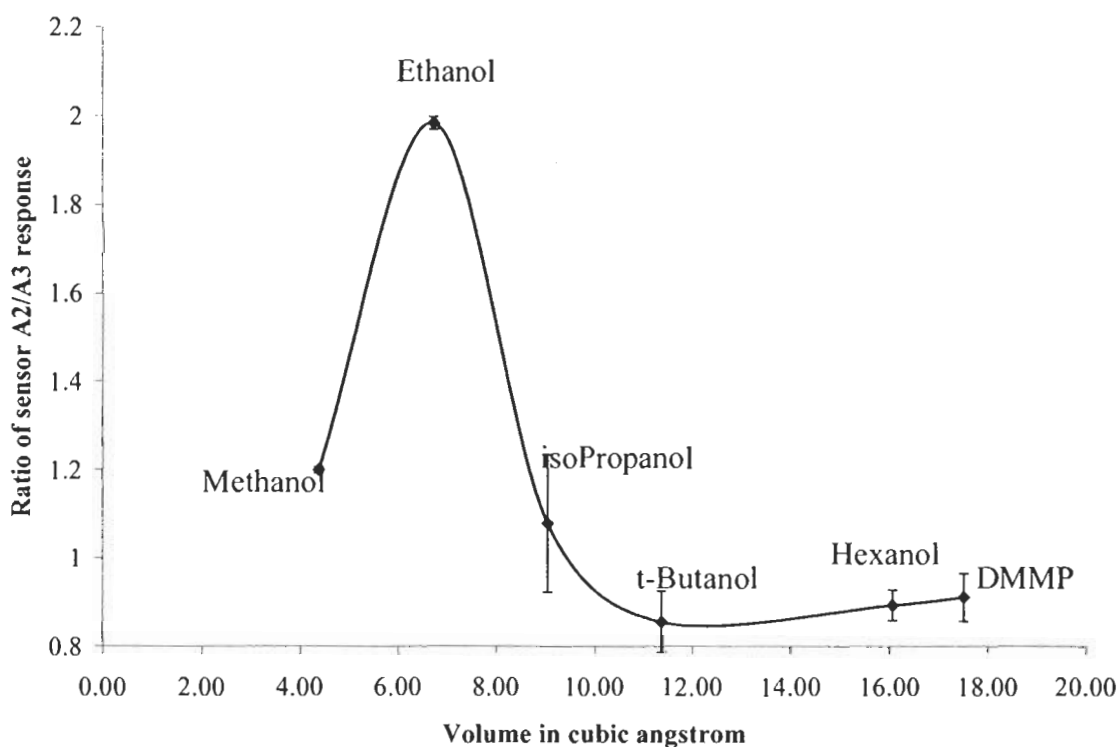


Figure 4.11. Ratio of response of A2 sensor to A3 sensor for each alcohol

4.4. Summary

Use of porous WO_3 materials in SMO detection has been shown to provide a route to achieve detection selectivity between methanol and DMMP. The key to achieving detection selectivity is to perform measurements on a dual detection system in which the response of a sensor based on porous powder is compared to that of a nonporous counterpart. IR adsorption measurements show that the difference in sensor response is

due to a size dependent difference in the adsorbed amount of the target compound on the surface of the porous WO_3 relative to the amount adsorbed on a nonporous WO_3 powder.

As a final comment, we believe the strength of this approach is in its simplicity.

Identification of a particular molecule is not done by comparing the response of different gases on a single sensor, but rather the same gas pulse on two different detectors. While each pulse has different pressures and gas delivery characteristics and different gases would have different reaction rates, these differences are normalized in calculating the values for the curves in Figure 4.8 and Figure 4.11.

Chapter 5

UV ILLUMINATION OF WO₃ POWDER SENSORS

5.1. Background

In the last chapter, we demonstrated a size selective approach to improving selectivity in SMO sensors and this was obtained by tailoring the architecture of the WO₃ powders. However, we recall that the original intent in establishing a research effort in the synthesis of WO₃ powder was not to produce new sensor material but rather, to generate material with sufficient surface area to enable IR adsorption studies. In this respect, the porous oxides also represent a factor of 3 improvement in surface area compared to the highest area material produced by the emulsion-based synthesis. The porous WO₃ had surface areas in the 110-150 m²/g range whereas the highest surface area obtained for nonporous WO₃ material was 45 m²/g. Given that the same high surface area WO₃ powders are amenable to both IR studies and sensor fabrication, we are now in a position to use the IR studies to gain a molecular understanding of the sensor behavior and to provide some insight to the development of new materials and approaches in an array-based detection system. Current and planned IR studies in nerve agent detection include photooxidation catalysts and powders impregnated with metal catalysts as well as the detection of other hazardous sulfur-based molecules (SO₂, H₂S, mercaptans) and NO_x compounds.

In this chapter, we examine the potential use of UV illumination as a means to increase selectivity in SMO sensors. For photooxidation catalysts such as TiO₂, it is well known that UV radiation of energy above the band gap generates electron-hole pairs that

migrate to the surface to initiate redox reactions leading to the decomposition of many organic molecules.¹³¹ While TiO₂ is the most widely used photooxidation catalyst, WO₃ also has the same band gap of 3.2 eV as TiO₂ and when WO₃ is radiated with UV light this material is well known to exhibit photochromism.¹³¹ In WO₃ powders, the photochromism is due to the injection of H⁺ and electrons¹³² (or OH⁻)¹³³ into the WO₃ lattice to produce a tungsten bronze structure. W⁺⁶ is partly reduced to W⁺⁵ or W⁺⁴ in the tungsten bronze and the blue coloration of the material results in electron transfer between adjacent W⁺⁶ and W⁺⁵ or W⁺⁴ sites.¹³³ While the source of the H⁺ is adsorbed water, it remains unclear as to whether the decomposition of the water is initiated by electron-hole pairs generated in WO₃ or by direct ionization under UV illumination.

Our interest in UV illumination of WO₃ stems from its potential use for selective oxidation of specific adsorbed compounds on the surface, thus providing an additional selective lever in a sensor array approach in SMO detection. Given the emphasis of nerve agent detection at LASST, our work in this chapter has focussed on photodecomposition of DMMP on WO₃. Using our two pronged approach, we performed both infrared studies and sensor measurements with and without UV illumination. The infrared studies under UV illumination were used to identify the conditions leading to decomposition of DMMP as well as for identifying the species formed on the surface. However, a sensor could also respond to UV illumination alone as the generation of electron-hole pairs or tungsten bronzes would cause a change in conductivity in the base material. Therefore, we also needed to measure the sensor response in order to understand the impact of UV illumination on the conductivity of the bare WO₃ powders as well as during exposure to a target gas pulse.

5.2. Experimental

The UV lamp was obtained from Pen-Ray (part # 90-0030-01) and produced 254 nm radiation at a power density of 3 milliwatts/cm² measured at a distance of 0.5" from the source. In the infrared measurements using DRIFT (See chapter 2 for details on the DRIFT accessory) the UV lamp was placed against the environmental viewing port at a distance of about 1 cm away from the powder sample. For the sensor testing data, the top plate of the sensor chamber was modified with a viewing port containing a UV-grade 2 in. glass disc. The UV lamp was placed in intimate contact with the glass window at a distance of approximately 4 cm from the sensor surface. All other experimental details are provided in chapter 2.

5.3. Results and Discussion

5.3.1. IR Studies

The infrared spectra of adsorbed DMMP on the WO₃ powder evacuated at various temperatures have been reported by Kim *et. al.*³¹ Figure 5.1 shows the spectra obtained in the low frequency region after the addition of DMMP on a nonporous powder at room temperature (curve a) and subsequent evacuation at elevated temperatures.

The assignments of the various bands are listed in Table 5.1. In brief, Kim *et. al.* showed that the features associated with the methoxy group decrease in intensity at 200°C and disappear at 350 °C (bands at 2955, 2854, 1064 and 1037 cm⁻¹) whereas the methyl group (band at 1313 cm⁻¹ remains at 350 °C along with several P-O bands in the 1200 –1000 cm⁻¹ region associated with a methyl phosphate species remaining on the

surface. The removal of the methoxy group results in the formation of methanol and it is the subsequent oxidation of the methanol on the WO_3 surface that leads to a change in conductivity.¹²⁶

Figure 5.2 shows the infrared spectra obtained for DMMP adsorption under UV illumination. An excess quantity of DMMP vapor was added to the WO_3 powder at room temperature for 5 minutes, the cell was evacuated, and spectra were recorded as a function of time of illumination. No change in the spectrum was observed for illumination over a period of 24 hrs. It was only after the sample was exposed to air that noticeable changes did occur in the spectrum. The curves in Figure 5.2 were obtained as a function of time of illumination in air and the changes that occur are very similar to the spectral changes with evacuation at elevated temperature shown in Figure 5.1. We therefore conclude that the adsorbed DMMP decomposes under UV illumination in air to form a methyl phosphate.

In a separate experiment, there was no decomposition of adsorbed DMMP observed when the UV illumination is performed in the presence of N_2 gas instead of air. O_2 is needed for this reaction to occur and it is most likely that decomposition of adsorbed DMMP occurs because of reaction with oxygen radicals or ozone generated by the UV lamp and not a photooxidative process involving WO_3 or by O^- adsorbed on the surface. There is evidence provided by ESR¹³⁴ showing that the electron-hole pairs formed by irradiation of a metal oxide can be captured by surface hole trapped centers leading to formation of reactive O^- sites. The presence of stable O^- species on the surface of silica supported WO_3 catalysts at room temperature have been detected by ESR spectroscopy¹³⁵

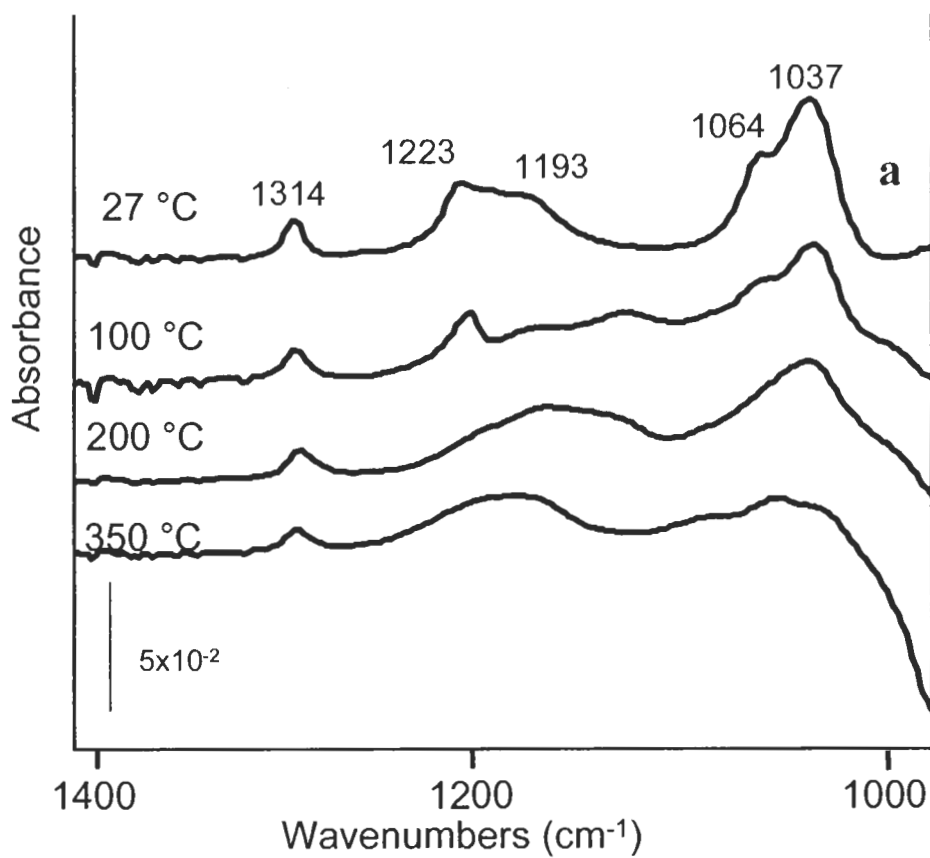


Figure 5.1. IR spectra of DMMP adsorbed on nonporous WO_3 at a) 27 °C and then evacuated at the specified temperature for 30 minutes. All spectra were recorded at room temperature.

Table 5.1. A Summary of Band Assignments for DMMP Adsorbed on TiO₂ and WO₃ Surfaces at 27 °C.

TiO ₂	WO ₃	Assignments
3006	2998	ν _a (CH ₃), ν (CH ₃ O)
2958	2955	ν _a (CH ₃ O)
2918	2917	ν _s (CH ₃), ν (CH ₃ O)
2854	2854	ν _s (CH ₃ O)
1459	1449	δ (CH ₃ O)
1418	1409	δ _s (P-CH ₃)
1314	1313	δ _a (P-CH ₃)
1237	1223	ν (P=O)
1186	1193	ρ (O-CH ₃)
1061	1064	ν (C-O)
1037	1037	ν (C-O)
919	918	ρ (P-CH ₃)

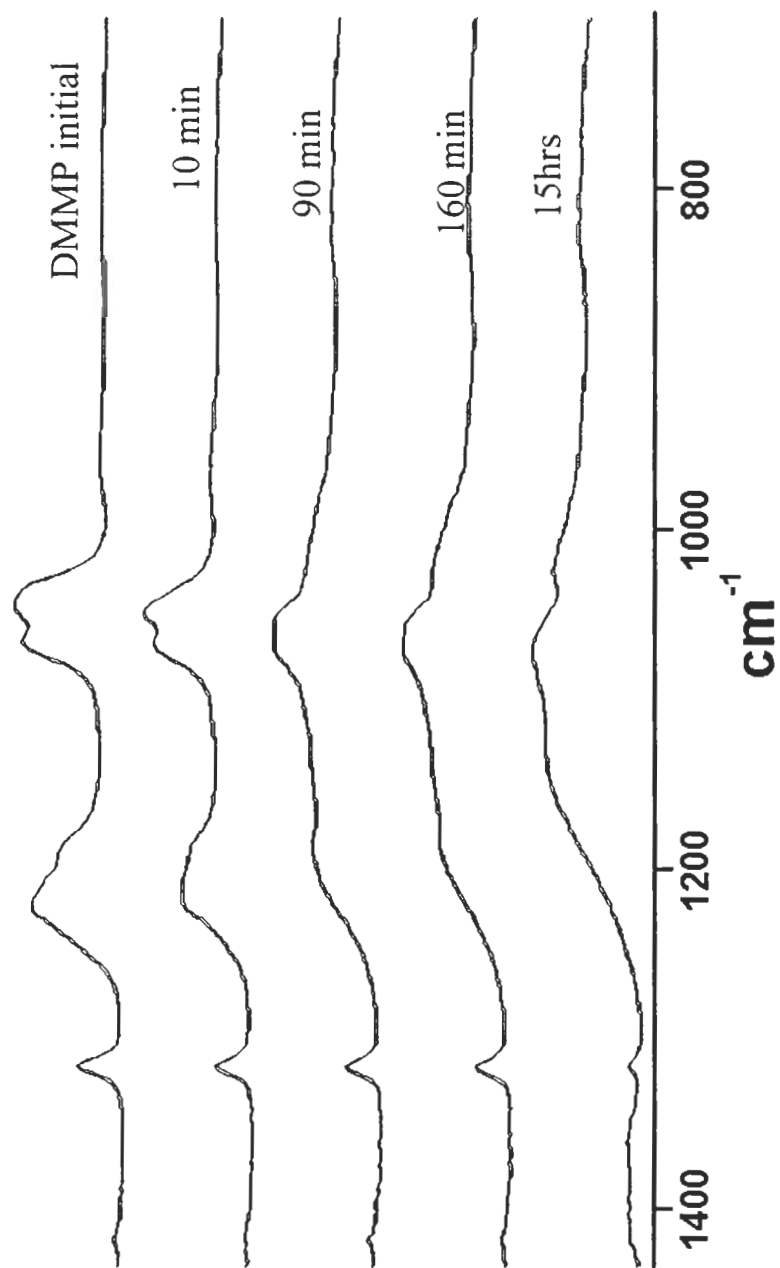


Figure 5.2. IR spectra of a) DMMP adsorbed on WO_3 at room temperature followed by UV illumination in air for the indicated time.

Given that a change in resistance in the WO_3 sensor is due to reaction with lattice oxygen and not ozone or oxygen radicals in the air, it is possible that the UV illumination will still be an approach to aid in detection selectivity in SMO sensing because the UV illumination could accelerate the methanol production or lower the temperature at which the sensor could operate. While the results with DMMP do not exclude other molecules from being directly photooxidized by WO_3 , it does show that we need to understand how UV illumination and secondary reactions such as ozone generation alter the operation of a WO_3 based sensor.

5.3.2. Sensor Testing under UV Illumination

Figure 5.3 is the sensor response curve obtained for methanol pulses on a nonporous WO_3 sensor operated at 400 °C. The sensor response to the first pulse was recorded with the UV lamp off and the response to the second pulse was recorded under UV illumination. UV illumination did not have any effect on the sensor response to the alcohol pulse. There is no change in the base resistance when the UV lamp was turned on or off and the initial drop in resistance was the same for both methanol pulses. We anticipated a change in the base conductivity with the generation of electron-hole pairs and this was not observed.

The results obtained with the sensor operating at 400 °C are in contrast to the change in resistance when a powder sensor is illuminated at room temperature. The curve in Figure 5.4 shows a sharp and immediate lowering of the resistance after the UV lamp was turned on. After 1 minute of UV exposure, the lamp was turned off and this resulted in a slow gradual return to the base resistance. In a second experiment, the resistance change was measured under continuous UV illumination at room temperature and the

sensor response is shown in Figure 5.5. As in Figure 5.4, there was an initial rapid drop in resistance when the lamp was turned on but this time, it was followed by an increase in resistance to a value well above the starting base resistance.

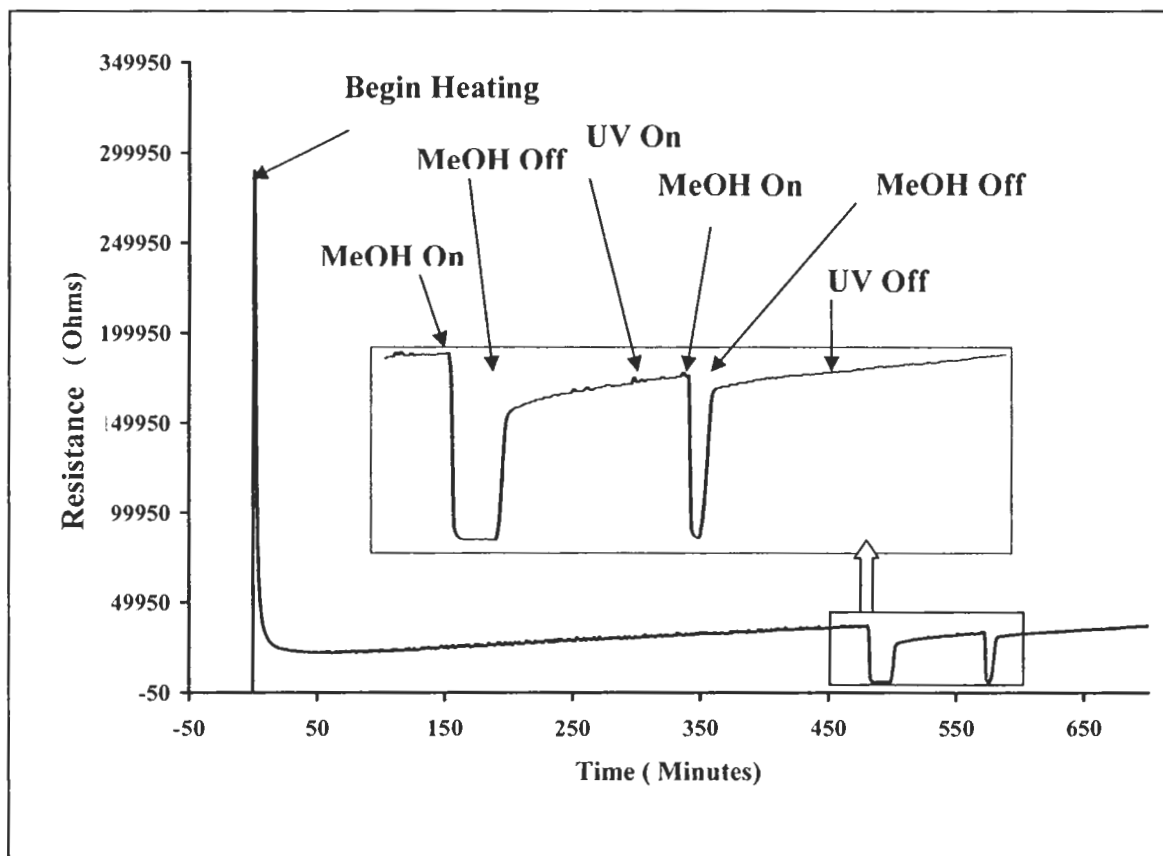


Figure 5.3. Sensor response curve to methanol pulses at 400 °C using a nonporous WO_3 powder sensor.

In metal oxides, both electrons and ions can be charge carriers. Since the mobility of electrons is typically 10^4 - 10^8 times higher than the mobility of ions, the concentration of ionic carrier must be 10^4 - 10^8 times higher than the concentration of electronic carriers before ionic conduction is a contributing factor to the overall conduction of the material¹⁰. The density of electrons and holes in WO_3 has been estimated at $10^5 / \text{cm}^3$ at 500 K¹⁰. By increasing the temperature, the conductivity of WO_3 increases because there is an increase of carriers due to the generation of sub-stoichiometric WO_{3-x} and because of an increase in the number of electrons in the conduction band due to thermal excitation. For example, Barak and Sienko¹³⁶ have measured carrier concentrations of $5 \times 10^{19} / \text{cm}^3$ at 417° K for $\text{WO}_{3-0.0076}$. This value is 10^{14} times greater than the estimated carrier concentration for stoichiometric WO_3 .

This larger difference in electron carrier concentration at room temperature and 400 °C could explain why a change in resistance is observed only at room temperature with UV illumination. At room temperature, the number of electron-hole pairs generated by UV illumination with sufficient energy to be excited in to the conduction band would result a in significant increase above the background carrier conduction. In contrast, at 400 °C the additional number of carriers generated by UV illumination would have a negligible contribution and thus would not leap through a perceptual change in resistance. Using mobility data for WO_3 thin film sensors¹³⁷, we have estimated that an increase in carrier concentration on the order of $10^{16} / \text{cm}^3$ for stoichiometric WO_3 would be needed to generate a drop in resistance with UV illumination shown in Figure 5.4. This value is significantly higher than the $10^5 / \text{cm}^3$ for stoichiometric WO_3 and insignificant to the

10^{18} - $10^{19}/\text{cm}^3$ carrier concentration in substoichiometric WO_{3-x} produced with heating to $400\text{ }^\circ\text{C}$.

However, it is unlikely that the initial rapid drop in resistance when the UV lamp is turned on in both Figures 5.4 and 5.5 are solely due to generation of electron-hole pairs. The electron-hole recombination process in photoelectric devices is much faster than the gradual return to the base resistance that is observed when the lamp is turned off in Figure 5.4. Ion mobilities are typically 10^4 - 10^8 times slower than electron-hole mobilities and thus a more plausible explanation for the sharp decrease in resistance is that the UV illumination is forming a tungsten bronze through intercalation of H^+ ions. It has been shown that the H^+ ions result from the decomposition of adsorbed water by optically generated electron-hole pairs¹³⁸. At room temperature, the surface is covered with a layer of strongly adsorbed water³³ providing a source of H^+ , and the migration of these H^+ and electrons into the WO_3 would lead to an increase in the conductivity of the material. The subsequent gradual decay when the lamp is turned off is due to the slow migration of the H^+ from the powder.

The difference in the curves in Figures 5.4 and 5.5 is most likely due to oxidation of the powder by the ozone generated by prolonged UV illumination. This was confirmed by repeating the prolonged UV illumination experiment in a flowing N_2 gas. In this case, after the initial drop in resistance, there was a slow small increase to an equilibrium base resistance that was still lower than the starting base resistance. (not shown) The implication of the ozone oxidation to a higher base resistance is that the starting material was already in a partially reduced state which was most likely due to the presence of a small amount of tungsten bronze.

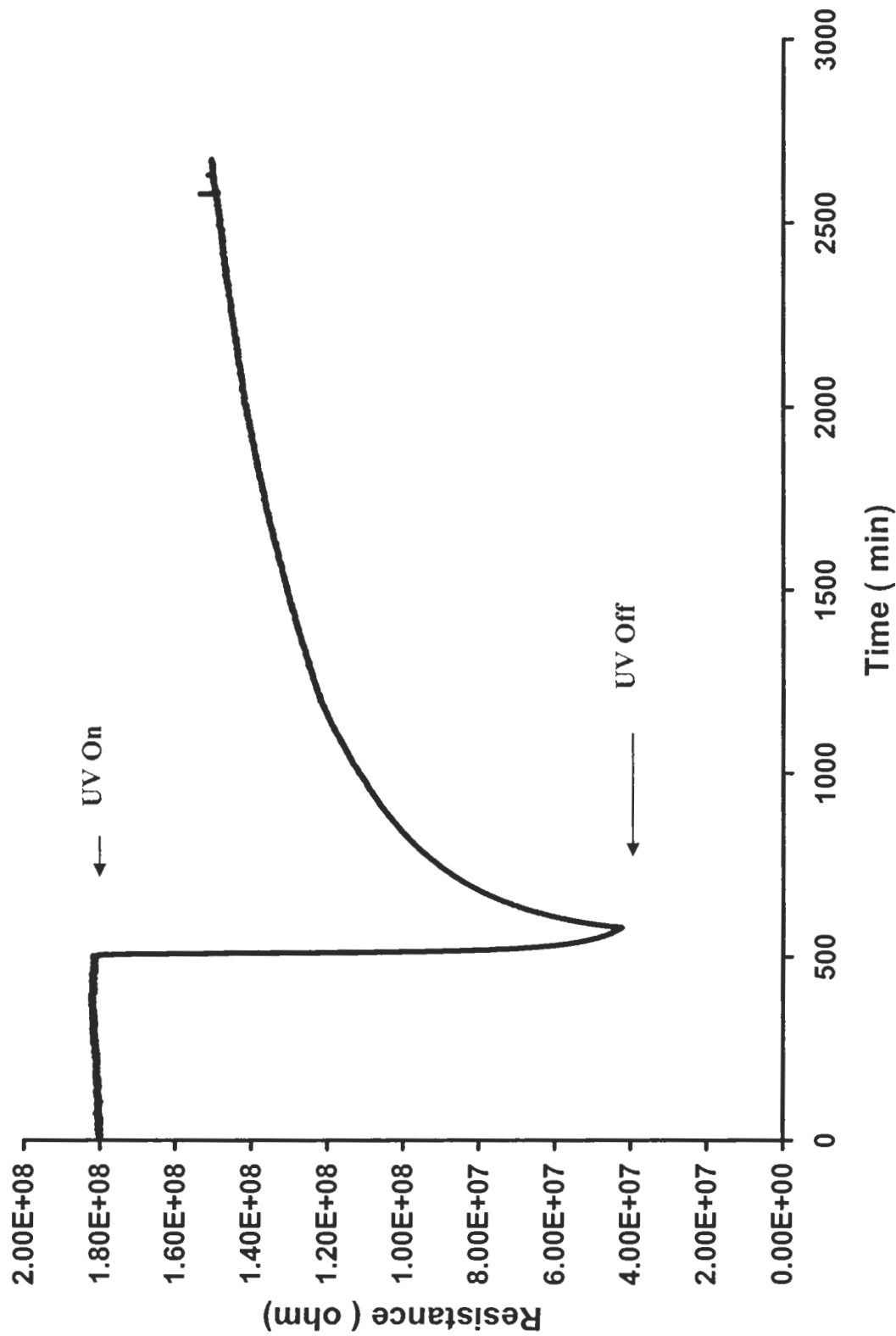


Figure 5.4. Resistance change to UV illumination in a nonporous WO₃ powder sensor at room temperature

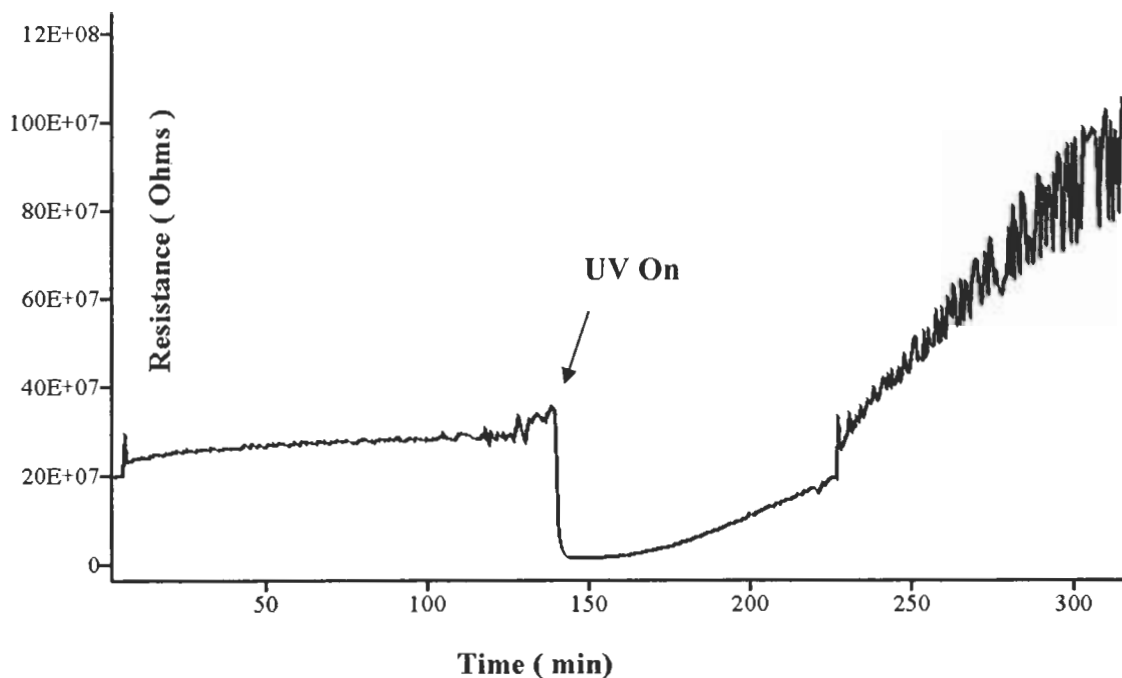


Figure 5.5. Resistance change under continuous UV illumination at room temperature.

The finding that tungsten bronzes are present in the starting powders helps explain a longstanding, yet unexplained feature of both thin film and powder based WO_3 sensors. Both powder and thin film sensors require an initial “bake in” to 400°C as the resistance change during the initial heating cycle is completely different from subsequent heating cycles. A typical example of this behavior is shown in Figure 5.6. The resistance is measured as a function of temperature and the temperature ramp rate was 2°C . During the first ramp in temperature, the resistance change follows the path labeled “A”. In path A, there is an initial rapid drop in resistance at relatively low temperature that plateaus nears 170°C followed by a slight increase to a maximum occurring at about 380°C and then a second decrease to 400°C . At 400°C the temperature is lowered and the resistance follows path ‘B’. After this initial “bake in” to 400°C , subsequent heat-cool

cycles retrace path “B” of the curve. While there are subtle differences in the curve depicted in Figure 5.6 from sensor-to-sensor, the general features described above occur in every WO₃ sensor tested at the LASST facility.

Since the resistive change along path A was of little consequence to the sensor operation (as a precautionary measure all sensors are first heated to 400°C) there was little effort to explain the origin of this behavior. It was generally accepted that Path A was the consequence of impurities or defect sites occurring during thin film preparation that were removed during the first heat cycle. However, the fact that the same curves are obtained in thin film sensors and in our recent powder work would make an impurity argument suspect at best. It is doubtful that the same impurities present in a UHV generated film would appear in a surfactant/solution generated powder. Moreover, the curve in path A appears despite the fact that both powder and thin films are first calcined at 500°C prior to the wire bonding step. Furthermore, we have found that sensors that have passed through one heat-cool cycle will retrace path A provided that these sensors sit on the shelf at room temperature for a period of a week before being retested.

An increase in temperature leads to both an increase in the number of carriers through an increase in “x” in WO_{3-x} and an increase in the number of electrons in the conduction band by thermal excitation. Both of these effects combine to lower the resistance of the WO₃ sensor with increasing operating temperature and can not explain the increase in the resistance that occurs between 250 °C and 380°C in path A. One possible explanation for an increase in resistance with temperature below 250°C and 380°C in path A is that, it is due to surface conductivity arising for a continuous network of water adsorbed on the surface^{139,140} Using infrared spectroscopy the relative amount

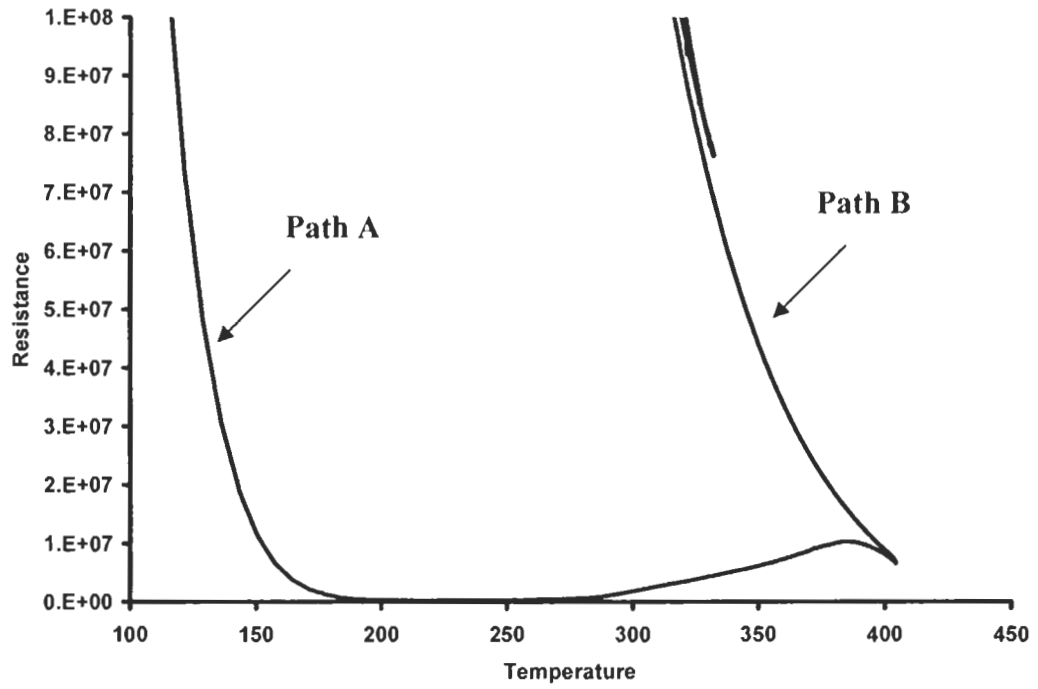


Figure 5.6. Characteristic plot of base resistance vs temperature for a WO_3 sensors.

of adsorbed water on the WO_3 powder surface was measured as a function of evacuation temperature,³³ and this curve is shown in Figure 5.7. From the water desorption curve it was concluded that there were two types of water on the surface; a weakly bound layer that could be removed by evacuation at room temperature and a strongly bound layer that requires heating to 400°C to be completely removed from the surface. The resistance passes through a maximum at 380°C because at temperatures above 380°C , the resistance is no longer dictated by a depletion of the contiguous adsorbed water layer but rather by the temperature dependence of the bulk conductivity. Once all the water is removed, the material follows path B as dictated solely by the lattice oxygen concentration and thermal excitation of carriers.

However, there is several inconsistencies with the water adsorption/desorption curve determined by infrared measurements and the sensor resistance curve shown in Figure 5.6. Once a sensor is heated to 400°C , it then follows path B with repeated temperature cycles from room temperature to 400°C . It does not return along path A. However, when a WO_3 powder that had undergone one cycle (heat to 400°C , cool to room temperature) is then exposed to air, the infrared spectrum shows an immediate readsorption of water to the original level. With a second temperature cycle, the water desorption follows the same curve shown in Figure 5.7. In other words, the water desorption curve shows no hysteresis behavior in that it is identical with repeated temperature cycles from room temperature to 400°C .

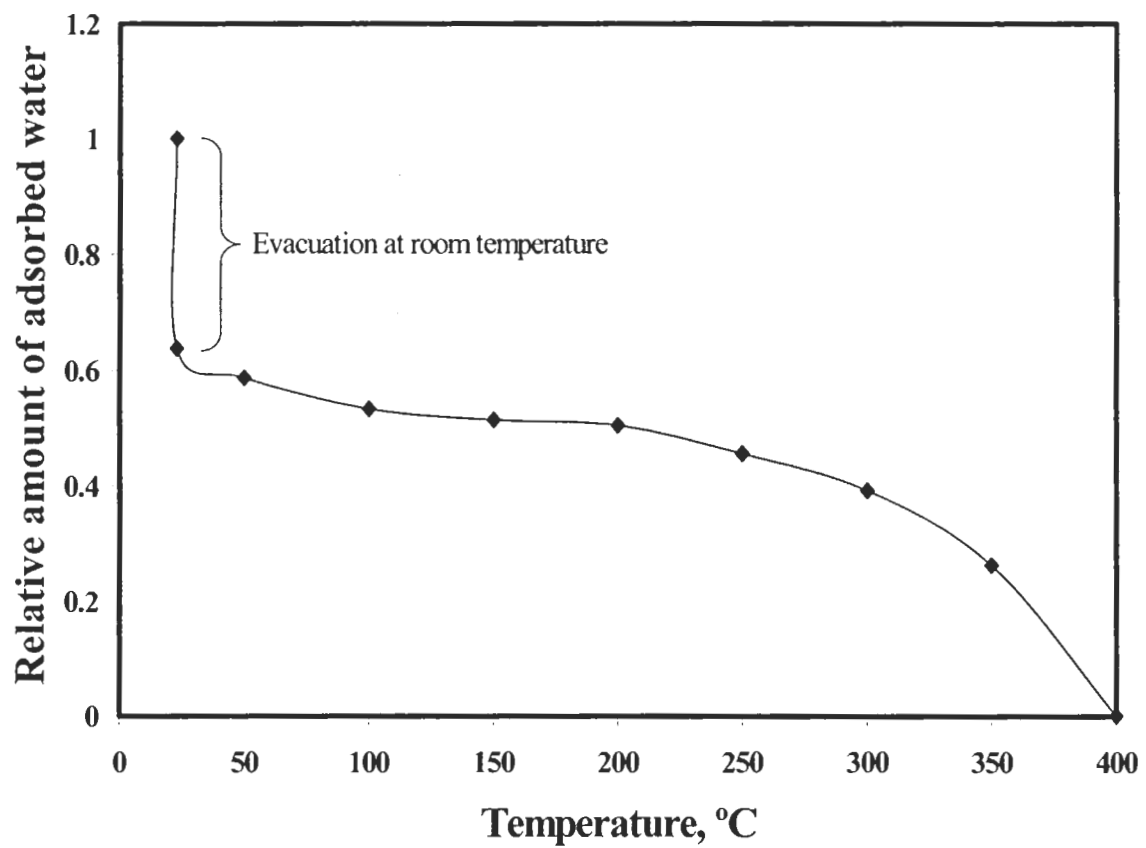


Figure 5.7. Water Desorption curve on WO₃ powder

While water is a contributing factor, we believe that it is the combination of adsorbed water leading to the presence of tungsten bronze in both the thin film sensor that gives rise to the hysteresis in the curve shown in Figure 5.6. Even though both powder and thin film sensors are calcined at 500°C before the wire bonding step, these sensors are only tested several days later. This is the critical time delay needed to form tungsten bronzes. Our UV illumination results suggest that there is a small amount of these bronzes present in the starting material and that they both form and decompose slowly with time. To support this conclusion, we recall, it is found that the shelf time is a critical factor in duplicating a path A response in a sensor. When a powder sensor that has undergone a full complete cycle (heat to 400°C, cool to room temperature) is allowed to sit on the shelf for a week, it will reproduce path A behavior when retested.

5.4. Summary

IR studies have shown that UV illumination at room temperature leads to decomposition of DMMP on WO₃ to form a methyl phosphonate. However, it is unlikely that this will lead to a method for improving detection selectivity in WO₃ based sensor as the decomposition does not involve lattice oxygen. The UV illumination experiments did reveal the presence of tungsten bronzes in the thin films or powder based WO₃ material. While tungsten bronzes can be eliminated by heating the sensors to 400°C, their presence was used to explain the anomalous resistance changes that occur during the first temperature cycle.

Chapter 6

FUTURE WORK

This work clearly shows that we have generated inherently porous materials that lead to selective detection between methanol and DMMP. Additional work in both material design, characterization and in sensor testing are clearly needed. Synthesizing different pore size WO_3 as well as other metal oxide (SnO_2) sensors could open a new route to improve the selectivity in the sensors. The mesoporous structures for WO_3 are fragile but it is known that organic and inorganic additives and binders can stabilize the structures. Obviously, choosing proper additives that will not interfere with the sensor response may or may not be easy. In future synthesis of this material this option could also play a valuable role in applying higher selectivity since structures will be more stable and this can be used to sense larger molecules. Method to directly fabricate porous WO_3 on the sensor platform may lead to the orientation of pores in the films. Additional characterization as N_2 adsorption to determine the morphology and XPS to determine degree of reduction of the materials also need to be investigated. In terms of sensor testing, there are plenty of additional studies that could be conducted. Certainly, samples A1, B1 and B2 should be tested for size selectivity. The robustness of the approach should also be examined by controlled measurements at different target concentration and at different temperatures.

REFERENCES

- (1) Zemel, J. N. *Thin Solid Films* **1988**, 163, 189.
- (2) Ylilammi, M. *Sens. Actuators* **1989**, 18, 167.
- (3) Lalauze, R.; Pijolat, C. *Sens. Actuators* **1984**, 5, 55.
- (4) Gopel, W. *Sensors and Actuators B* **1989**, 16, 167.
- (5) Shaver, P. J. *Appl. Phys. Lett.* **1967**, 11, 255.
- (6) MacIntyre, J. R.; Marshall, T. N. *Instrumentation Technology* **1972**, 8, 29.
- (7) Bernhardt, G.; Silvestre, C.; LeCursi, N.; Moulzolf, S. C.; Frankel, D. J.; Lad, R. J. *Sens. Actuators* **2001**, B77, 368.
- (8) LeGore, L. J.; Snow, K.; Galipeau, J. D.; Vetelino, J. F. *Sensors and Actuators B* **1996**, 35-36, 164.
- (9) Moulzolf, S. C.; LeGore, L. J.; Lad, R. J. *Thin Solid Films* **2001**, 400, 56.
- (10) LeGore, L.J.; Ph.D. Thesis, University of Maine **2000**.
- (11) Kroger, F. A.; Vink, H. J., "Relation between the concentrations of imperfections in crystalline solids," in *Solid State Physics*, F. Seitz and D. Turnbull, Eds. New York: Academic Press, **1956**
- (12) Fruhbeager, B.; Stirling, N.; Grillo, F.G.; Ma, S.; Ruthven, D.; Lad, R.J.; Frederick, B.G. *Sensors Actuator*, **2001**, B76, 226-234.
- (13) Kanan, S. M.; Tripp, C. P. *Langmuir* **2002**, 18, 722.

- (14) Semancik, S.; Cavicchi, R.; Wheeler, M. C.; Tiffany, J. E.; Poirier, G. E.; Walton, R. M.; Suehle, J. S.; Panchapakesan, B.; DeVoe, D. L. *Sensors and Actuators B* **2001**, *77*, 579.
- (15) Menzel, R.; Goschnick, J. *Sensors and Actuators B* **2000**, *43*, 235.
- (16) Kanan, S. M.; Lu, Z.; Tripp, C. P. *J. Phys. Chem. B* **2002**, *106*, 9576.
- (17) Kanan, S. M.; Tripp, C. P. *Langmuir* **2001**, *17*, 2213.
- (18) Fruhberger, B.; Stirling, N.; Grillo, F. G.; Ma, S.; Ruthven, D.; Lad, R. J.; Frederick, B. G. *Sensor and Actuator* **2001**, B76, 226-234.
- (19) Cox, D. F.; Fryberger, T. B.; Semancik, S. *Surf. Sci.* **1989**, *224*, .
- (20) Cox, D. F.; Fryberger, T. B.; Semancik, S. *J. Vac. Sci. Technol. A* **1988**, *6*, 828.
- (21) Semancik, S.; Cox, D. F. *Sensors and Actuators B* **1987**, *12*, 101.
- (22) Fryberger, T. B.; Semancik, S. *Sensors and Actuators B* **1990**, *2*, 305.
- (23) Cox, D. F.; Fryberger, T. B.; Semancik, S. *Phys. Rev. B* **1988**, *38*, 2072.
- (24) Cavicchi, R. E.; Suehle, J. S.; Chaparala, P.; Kreider, K. G.; Gaitan, M.; Semancik, S. *Proc of the 1994 Solid State Sensor and Actuator Workshop* **1994**, Hilton Head, S.C, 53.
- (25) Taylor, T.; Patterson, H. *Appl. Spectrosc.* **1994**, *48*, 674.
- (26) Bjorkman, C. H.; Fukuda, M.; Yamazaki, T.; Miyazaki, S.; Hirose, M. *Jpn. J. Appl. Phys.* **1995**, *34*, 722.
- (27) Tripp, C. P.; Hair, M. L. *Appl. Spectrosc.* **1992**, *46*, 100.
- (28) Morrow, B. A. In "surface groups on oxides", *Spectroscopic Analysis of Heterogeneous Catalysts, Part A: Methods of Surface Analysis*; Fierro, J. L. G., ed.; Elsevier: Amsterdam, 1990.

- (29) Kiselev, A. V.; Lygin, V. I. *Infrared Spectra of Surface Compounds*; John Wiley and Sons: New York, 1975.
- (30) Hair, M. L. *Infrared Spectroscopy in Surface Chemistry*; Marcel Dekker: New York, 1967.
- (31) Kim, C. S.; Lad, R. J.; Tripp, C. P. *Sensors and Actuators B* **2001**, 76, 442.
- (32) Lu, Z.; Kanan, S. M.; Tripp, C. P. *J. Mater. Chem.* **2001**, 12, 2002.
- (33) Kanan, S. M.; Lu, Z.; Cox, J. K.; Bernhardt, G.; Tripp, C. P. *Langmuir* **2002**, 18, 1707.
- (34) Lee, K. *Thin Solid Films* **1997**, 302, 84.
- (35) Bechinger, C.; Muffler, H.; Schafle, C.; Sundberg, O.; Leiderer, P. *Thin Solid Films* **2000**, 366, 135.
- (36) Brinker, C. J.; Scherer, G. W. *Academic Press, New York* **1990**, .
- (37) Bradley, D. C.; Mehrotra, R. C.; Gaur, D. P. *Academic Press, London* **1978**, .
- (38) Hubert-Pfalzgraf, L. G. *New Journal of Chemistry* **1987**, 11, 663.
- (39) Cantalini, C.; Wlodarski, W.; Li, Y.; Passacantando, M.; Santucci, S.; Comini, E.; Faglia, G.; Sberveglieri, G. *Sensors and Actuators B* **2000**, 64, 182.
- (40) Cantalini, C.; Atashbar, M. Z.; Li, Y.; Ghantasala, M. K.; Santucci, S.; Wlodarski, W.; Passacantando, M. *J. Vac. Sci. Technol.* **1999**, A17, 1873.
- (41) Chemseddine, A.; Morineau, R.; Livage, J. *Sol. St. Ionics* **1983**, 9 & 10, 357.
- (42) Gotic, M.; Ivanda, M.; Popovic, S.; Music, S. *Materials Science and Engineering B* **2000**, 77, 193.
- (43) Sun, M.; Xu, N.; Cao, Y. W.; Yao, J. N.; Wang, E. G. *Journal of Materials Science Letters* **2000**, 19, 1407.

- (44) Deepa, M.; Sharma, n; Varshney, s; Varma, S.; Agnihotry, S. A. *J. Mater. Sci.* **2000**, 35, 5313.
- (45) Livage, J.; Henry, M.; Sanchez, C. *Prog. Solid St. Chem* **1988**, 18, 259.
- (46) Nishide, T.; Mizukami, F. *Thin Solid Films* **1995**, 259, 212.
- (47) Wang, L.; Shi, J.; Gao, J.; Tomura, S.; Yan, D. *J. Non-Cryst. Solids* **2000**, 278, 178.
- (48) Oye, G.; Sjoblom, J.; Stocker, M. *Adv. Colloid Interface Sci.* **2001**, 89-90, 439.
- (49) Zhao, D.; Goldforb, D. *J. Chem. Soc., Chem. Commun.* **1995**, 1995, 875.
- (50) Stucky, G. D.; Huo, Q.; Firouzi, A.; Chmelka, B. F.; Schacht, S.; Voigt-Martin, I. G.; Schuth, F. *Directed Synthesis of Organic/Inorganic Composite Structures, Studies in Surface Science and Catalysis*; Elsevier Science B.V.: Amsterdam, 1997.
- (51) Fodor, K. F.; Bitter, J. H., de Jong, K.P. *Micropor. Mesopor. Mater.* **2002**, 56, 101.
- (52) Renzo, F. D.; Cambon, H.; Dutartre, R. *Microporous Materials* **1997**, 10, 283.
- (53) Clacens, J.-M.; Pouilloux, Y.; Barrault, J. *Appl. Catal. A* **2002**, 227, 181.
- (54) Nagamine, S.; Kurumanda, K.; Tanigaki, M.; Endo, A. *Micro. Meso. Mater.* **2001**, 49, 57.
- (55) Melezhyk, O. V.; Prudius, S. V.; Brei, V. V. *Micro. Meso. Mater.* **2001**, 49, 39.
- (56) Dai, L.; Mau, A. W. H. *J. Phys. Chem. B* **2000**, 104, 1891.
- (57) Papirer, E. *Adsorption on Silica Surfaces*; Marcel Dekker, Inc.: New York, 1998.
- (58) Chen, C. Y.; Burkett, S. L.; Li, H.-X.; Davis, M. E. *Microporous Materials* **1993**, 2, 27.
- (59) Huo, Q.; Margolese, D. I.; Ciesla, U.; Demuth, D. G.; Feng, P.; Gier, T. E.; Sieger, P.; Firouzi, A.; Chmelka, B. F.; Schuth, F.; Stucky, G. D. *Chem. Mater.* **1994**, 6, 1176.

- (60) Beck, J. S.; Vartuli, J. C.; Roth, W. J.; Leonowicz, M. E.; Kresge, C. T.; Schmitt, K. D.; Chu, C. T.-W.; Olson, D. H.; Sheppard, E. W.; McCullen, S. B.; Higgins, J. B.; Schlenker, J. L. *J. Am. Chem. Soc.* **1992**, 114, 10834.
- (61) Ulaganppan, N.; Battaram, N.; Raju, V. N.; Rao, C. N. R. *J. Chem. Soc., Chem. Commun.* **1996**, 1996, 2243.
- (62) <http://www.ch.ic.ac.uk/liquidcrystal/micelles.jpg>.
- (63) Koyana, K. A.; Tatsumi, T. *Chem. Commun.* **1996**, 1996, 145.
- (64) Huo, Q.; Leon, R.; Petroff, P. M.; Stucky, G. D. *Science*, **1995** 268, 1324.
- (65) Namba, T.; Nishiyama, Y.; Yasui, I. *J. Mater. Res.* **1991**, 6, 1324.
- (66) Nishide, T.; Mizukami, F. *Thin Solid Films* **1995**, 259, 212.
- (67) Daniel, M. F.; Desbat, B.; Lassegues, J. C.; Gerand, B.; Figlarz, M. *J. Solid State Chem.* **1987**, 67, 235.
- (68) Lee, S.-H.; Cheong, H. M.; Ahang, J.-G.; Mascarenhas, A.; Benson, D. K.; Deb, S. K. *Appl. Phys. Lett.* **1999**, 74, 242.
- (69) Forsythe, E. W.; Choong, V.-E.; Le, T. Q.; Gao, Y. *J. Vac. Sci. Technol. A* **1999**, 17, 3429.
- (70) Salje, E. *Acta Cryst.* **1975**, A31, 360.
- (71) Nonaka, K.; Takase, A.; Miyakawa, K. *Journal of Materials Science Letters* **1993**, 12, 274.
- (72) Tripp, C. P.; Hair, M. L. *Langmuir* **1991**, 7, 923.
- (73) Brunauer, S.; Emmett, P. H.; Teller, E. *J. Am. Chem. Soc.* **1938**, 60, 309.
- (74) Machin, W. D.; Parsons, B. I.; Montgomery, D. S. *Mines Branch Technical Bulletin* **1961**, TB26, 1.

- (75) Emmett, P. H. *Measurement of the Surface Area of Solid Catalysts*, in "Catalysis"; Reinhold Publishing Corporation: New York, 1954.
- (76) McCash, E. M. *Surface Chemistry*; Oxford University Press: New York, 2001.
- (77) Machin, W. D.; Parsons, B. I.; Montgomery, D. S. Mine Branch Technical Survey, TB26, 1961
- (78) Sing, K. S. W.; Everett, D. H.; Haul, R. A. W.; Moscou, L.; Pierotti, R. A.; Rouquerol, J.; Siemineiewska, T. *Pure Appl Chem* **1985**, 57, 603.
- (79) Yortsos, Y. C. *Methods in The Physics of Porous Media*; Academic Press: London, 1999.
- (80) Barrett, E. P.; Joyner, L. G.; Halenda, P. P. *J. Am. Chem. Soc.* **1954**, 73, 373.
- (81) Saito, A.; Foley, H. C. *AIChE* **1991**, 37, 429.
- (82) Horvath, P. E.; Kawazoe, K. *J. Chem. Eng. Jpn.* **1983**, 16, 470.
- (83) *Acta Cryst.* **1969**, B25, 925
- (84) Ilar, R.K, *The Chemistry of Silica*, John Wiley and Sons, New York, **1979**
- (85) Ben McCool, *personal communication*.
- (86) Biz, S.; Occelli, M. L. *Catal. Rev.-Sci. Eng.* **1998**, 40, 329.
- (87) Schüth, F. *Chem. Mater.* **2001**, 13, 3184.
- (88) Takahara, Y.; Kondo, J. N.; Takata, T.; Lu, D.; Domen, K. *Chem. Mater.* **2001**, 13, 1194.
- (89) Wang, Y.; Ma, C.; Sun, X.; Li, H. *Micro. Meso. Mater.* **2001**, 49, 171.
- (90) Thieme, M.; Schüth, F. *Micro. Meso. Mater.* **1999**, 27, 193.
- (91) Hirashima, H.; Imai, H.; Balek, V. *J. Non-Cryst. Solids* **2001**, 385, 96.
- (92) Antonelli, D. M.; Ying, J. Y. *Angew. Chem. (Int. Ed.) Engl.* **1996**, 35, 426.

- (93) Gao, Y.; Du, J.; Gu, T. *J. Chem. Soc., Faraday Trans. I* **1987**, 83, 2671.
- (94) Ciesla, U.; Demuth, D.; Leon, R.; Petroff, P.; Stucky, G.; Unger, K.; Schüth, F. *J. Chem. Soc., Chem. Commun.* **1994**, 1387.
- (95) Stein, A.; Fendorf, M.; Jarvie, T. P.; Mueller, K. T.; Benesi, A. J.; Mallouk, T. E. *Chem. Mater.* **1995**, 7, 304.
- (96) Cheng, W.; Baudrin, E.; Dunn, B.; Zink, J. I. *J. Mater. Chem.* **2001**, 11, 92.
- (97) Kumar, D.; Schumascher, K.; Hohenesche, CdF.; Grun, M.; Unger, K. K. *Colloids Surf. A: Physicochem. Eng. Aspects* **2001**, 187-188, 109.
- (98) Santato, C.; Odziemkowski, M.; Ulmann, M.; Augustynski, J. *J. Am. Chem. Soc.* **2001**, 123, 10639.
- (99) Agrawal, A.; Habibi, H. *Thin Solid Films* **1989**, 169, 257.
- (100) Choma, J.; Burakiewicz-Mortka, W.; Jaroniec, M. *Colloids Surf. A: Physicochem. Eng. Aspects* **2002**, 203(1-3), 97.
- (101) Landau, M. V.; Dafa, E.; Kaliya, M. L.; Herskowitz, M. *Micro. Meso. Mater.* **2001**, 49, 65.
- (102) Wirnsberger, G.; Yang, P.; Scott, B. J.; Chmelka, B. F.; Stucky, G. D. *Spect. Acta A* **2001**, 57, 2049.
- (103) Li, G.-J.; Kawi, S. *Talanta* **1998**, 45, 759.
- (104) Wang, S.; Wu, D.; Sun, Y.; Zhong, B. *Mater. Res. Bull.* **2001**, 36, 1717.
- (105) Balazsi, C.S. *Material Structure*, **1999**, 6(2), 135.
- (106) Kresge, C. T.; Leonowicz, M. E.; Roth, W. J.; Vartuli, J. C.; Beck, J. S. *Nature* **1992**, 359, 710.

- (107) Schumacher, K.; Ravikovitch, P. I.; DuChesne, A.; Neimark, A. V.; Unger, K. K. *Langmuir* **2000**, *16*, 4648-4654.
- (108) Stein, A.; Fendorf, M.; Jaevie, T. P.; Mueller, K. T.; Benesi, A. J.; Mallouk, T. E. *Chem. Mater.* **1995**, *7*, 304-313
- (109) Booth, J.; Ekstrom, T.; Iguchi, E.; Tillry, R. J. D. *J. Solid State Chem.* **1982**, *41*, 293-307
- (110) Sofian Kanan, *unpublished data*
- (111) Kumar, D.; Schumacher, K.; Hohenesche, C. F.; Grun, M.; Unger, K. K. *Colloids Surf. A: Physicochem. Eng. Aspects* **2001**, 187-188, 109.
- (112) Cao, L.; Segal, S. R.; Suib, S. L.; Tang, X.; Satyapal, S. *J. Catal.* **2000**, *194*, 61.
- (113) Templeton, M. K.; Weinberg, W. H. *J. Am. Chem. Soc.* **1985**, *107*, 774.
- (114) Blajeni-Aurian, B.; Boucher, M. M. *Langmuir* **1989**, *5*, 170.
- (115) Mitchell, M. B.; Sheinker, V. N.; Mintz, E. A. *J. Phys. Chem.* **1997**, *101*, 11192.
- (116) Rusu, C. N.; Yates Jr, J. T. *J. Phys. Chem. B* **2000**, *104*, 12292.
- (117) Obee, T. N.; Satyapal, S. *J. Photochem. Photobiol., A* **1998**, *118*, 45.
- (118) Bertilsson, L.; Potje-Kamloth, K.; Liess, H.-D. *Langmuir* **1999**, *15*, 1128.
- (119) Zhanpeisov, N. U.; Zhidomirov, G. M.; Yudanov, I. V.; Klabunde, K. J. *J. Phys. Chem.* **1994**, *98*, 10032.
- (120) Li, Y.-X.; Klabunde, K., *J. Langmuir* **1991**, *7*, 1388.
- (121) Li, Y.-X.; Schlup, J. R.; Klabunde, K. J. *Langmuir* **1991**, *7*, 1394.
- (122) Hedge, R. I.; White, J. M. *Appl. Surf. Sci.* **1987**, *28*, 1.
- (123) Henderson, M. A.; Jin, T.; White, J. M. *J. Phys. Chem.* **1986**, *90*, 4607.
- (124) Tesfai, T. M.; Sheinker, V. N.; Mitchell, M. B. *J. Phys. Chem. B* **1998**, *102*, 7299.

- (125) Taranenکو, N.; Alarie, J.-P.; Stokes, D. L.; Vo-Dinh, T. *J. Raman Spectrosc.* **1996**, 27, 379.
- (126) Frederick, B. *private communication*
- (127) Moulzolf, S. C.; LeGore, L. J.; Lad, R.J. *Thin Solid Films* **2001**, 400, 56-63.
- (128) Bernhardt, G.; Silvestre, C.; LeCursi, N.; Moulzolf, S.C.; Frankel, D.J.; Lad, R.J. *Sens. Actuators* **2001**, B77, 368-374.
- (129) Pilling, R. S.; Bernhardt, G.; Kim, C. S.; Duncan, J.; Crothers, C. B. H.; Kleinschmidt, D.; Frankel, D. J.; Lad, R. J.; Frederick, B. G. *Sens. Actuators* **2003**, in press.
- (130) Rossi, P. F.; Busca, G. *Colloids and Surfaces*, **1985**, 16: 95-102.
- (131) Zhuang, J.; Rusu, C. N.; Yates, Jr J. T. *J. Phys. Chem. B* **1999**, 103, 6957.
- (132) Sun, M.; Xu, N. *J. Mater. Res.* **2000**, 15, 927.
- (133) Hurditch, R.; *Electron Lett.* **1975**, 11, 142.
- (134) Che, M.; Tench, A. J. *Adv. in Catal.* **1982**, 31, 77-133
- (135) Shvets, V. A.; Sapozhnikov, V. B.; Chuvylkin, N. D.; Kazansky, V. B., *J. Catalysis*, **1978**, 52, 459-61.
- (136) Berak, J. M.; Sienko, M. J. *J. Solid State Chem.* **1970**, 2, 109-133.
- (137) Moulzolf, S. C.; Frankel, D. J.; Lad, R. J. *Rev. Sci. Instrum.*, **2002**, 73(6), in press
- (138) Bechinger, C.; Wirth, E.; Leiderer, P., *Appl. Phys. Lett.* **1996**, 68 (20) 2834.
- (139) Veregin, R.P.N.; Powell, D.; Tripp, C.P.; McDougall, N. V.; Mahon, M. *Imag. Sci. Technol.*, **1997**, 41(2), 192-196.
- (140) Vergin, R.P.N.; Tripp, C.P.; McDougall, M.N.V.; Osmond, D. J. *Imag. Sci. Technol.* **1995**, 39, 429.

BIOGRAPHY OF THE AUTHOR

Anil Waghe was born in Mumbai (Bombay), India. He had his high school education in Parle Tilak Vidyalaya schools and Parle College. He earned a B.Sc.(first class) degree in chemistry from the University of Bombay in 1986. He graduated with his M.Sc degree in Organic Chemistry with polymer synthesis specialization from the Indian Institute of Technology, Bombay in 1988. He was employed as Junior Information Scientist at Sandarbha Scinfotech Pvt. Ltd., Technical Office at Grauer and Weils Ltd. and finally Research and Development Chemist at Chemspec Chemical before coming to United States.

He entered the graduate program at the University of Maine, Orono, Maine in September 1996 and he served as a graduate research assistant for the Department of Chemistry and LASST and he was a teaching assistant for the Department of Chemistry. He is a candidate for the Doctor of Philosophy degree in Chemistry from The University of Maine in August, 2003.